Localization Microscopy Based Super-resolution Imaging and Analysis of Dynamics

Zur Erlangung des akademischen Grades eines

DOKTOR-INGENIEURS

an der Fakultät für

Elektrotechnik und Informationstechnik
des Karlsruher Instituts für Technologie (KIT)

genehmigte

DISSERTATION

von
Lu Zhou
geb. in Jilin, China

Tag der mündlichen Prüfung:	14. März 2018
Hauptreferent:	Prof. Dr. Uli Lemmer
Korreferent:	Prof. Dr. Gerd Ulrich Nienhaus

Contents

1. Introduction

Since the discovery that the cell is the fundamental unit of life by using a light microscope, far-field optical microscopy techniques have become essential for studies in biology [1]. Traditional light microscopy suffers from the low contrast of biological samples, whereas fluorescence microscopy provides a new method to detect molecules labeled with fluorescent probes, such as fluorescent proteins and fluorescent dyes, offering high biochemical specificity and sensitivity [2]. With these advantages, fluorescence microscopy has become the most widely used microscopic technique in cellular biology over the centuries. However, the resolution of optical systems is limited by the diffraction of light, to roughly half of the wavelength (about 200 – 300 nm) (Figure 1.1). This means that the sub-cellular structures, e.g., mitochondrial cristae and nuclear pores, that are smaller than the diffraction limit cannot be discerned.

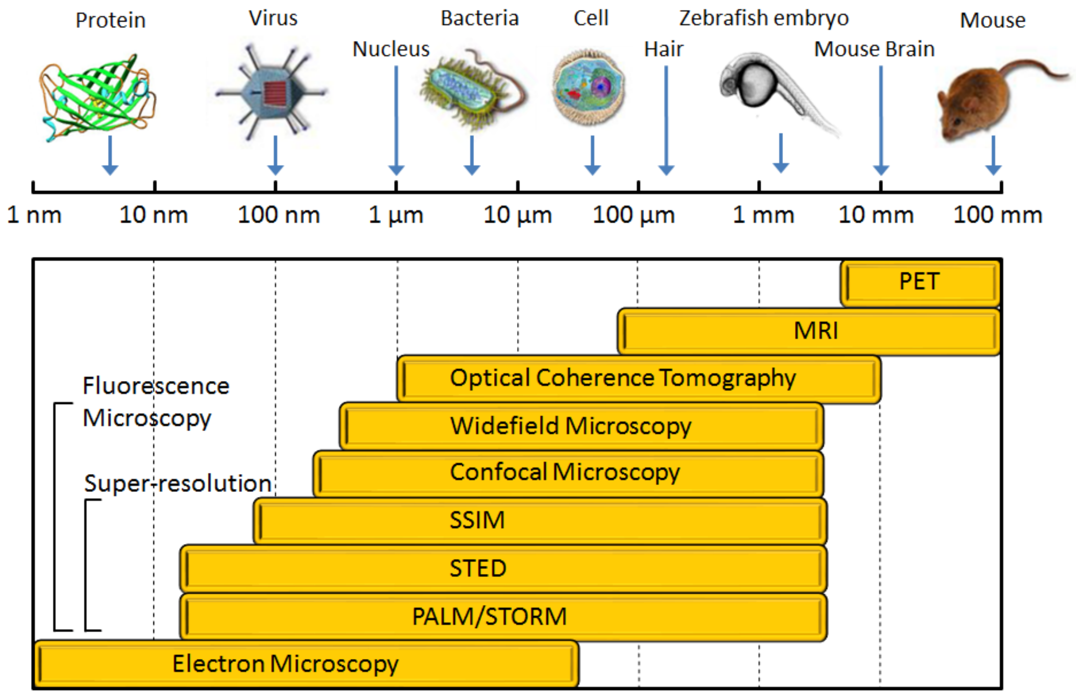

Figure 1.1: Overview of various biological imaging techniques and their spatial resolutions. Image adopted from reference [3]. Pictures taken from [3–5].

In recent decades, multiple super-resolution far-field fluorescence microscopy techniques have been developed aiming at overcoming the diffraction limit, such as stimulated emission depletion microscopy (STED) [6], structured illumination microscopy (SSIM) [7], photoactivated localization microscopy (PALM) [8], and stochastic optical reconstruction microscopy (STORM) [9] (Figure 1.1). Among these methods, PALM and STORM are two prominent localization-based super-resolution microscopic techniques which utilize photoactivatable proteins and photoswitchable fluorescent dyes, respectively, to temporally separate the spatially close molecules so that the positions of molecules can be precisely detected. In particular, for the PALM technique, photoactivatable fluorescent proteins can be genetically fused to the target protein of interest, which offers a powerful and convenient way for live-cell imaging. Moreover, trajectories of molecules can be achieved by tracking the positions of individual molecules, which also allows measuring of molecular dynamics, such as diffusion properties of proteins, in living cells with the PALM technique [10].

In this work, we have focused on the development and the application of PALM microscopy. The PALM technique was successfully employed to investigate two biological processes: (1) the membrane repair process in mammalian cells and zebrafish; (2) the vesicle dynamics in fungal cells. The two biological topics will be introduced in the following sections.

1.1 Repair process of the cell membrane

Human cells routinely suffer small plasma membrane lesions induced, for example, by mechanical stress. Muscle cells have developed efficient membrane repair mechanisms, which involve the interaction between many different proteins, such as dysferlin (Dysf) [11] and MG53 [12].

Dysf is a transmembrane protein with seven C2 domains. Humans with mutations in the *DYSF* gene can acquire limb-girdle muscular dystrophy type 2B (LGMD2B), Miyoshi myopathy or distal myopathy with anterior tibialis onset [13, 14]. Dysf associates with many other players to fulfill the function of membrane repair. It was reported that Dysf binds to phosphatidylserine (PS), a membrane phospholipid, in a Ca^{2+}-dependent manner through its C2-domains [15]. Besides PS, Dysf also interacts with other functional proteins in the membrane repair process. Annexins interact with Dysf and form multimeric complexes in a Ca^{2+}-dependent manner at the site of the lesion [16–19]. Muscle-specific protein caveolin-3 (Cav3) also associates with Dysf and regulates membrane localization and endocytosis of Dysf [20, 21]. Moreover, MG53, a tripartite motif protein (TRIM72), was also recently reported to interact with Dysf and fast accumulate at the cell membrane lesion [12, 22]. This work is mainly focused on the roles of Dysf and MG53 in the membrane repair process. A schematic model for the membrane repair process based on these two proteins is shown in Figure 1.2.

Dysf is proposed as a key functional protein for muscle membrane repair, which rapidly recruits to membrane wounds after the cell membrane damage [11]. Further studies showed that a Mini-Dysf (Figure 1.2, green) with two C2 domains was generated by calpain (Figure 1.2, pink) in a Ca^{2+} dependent manner after membrane damage [23, 24]. Moreover, the Mini-Dysf quickly translocates to the damage site and accumulates, whereas the full-length Dysf does not [23, 24] (Figure 1.2). In zebrafish, further deletion of the C2 domains generated an isoform that was still able to accumulate at the site of lesion and rescue patch formation in Dysf mutants and morphants [24, 25]. It was also reported that MG53 performs an essential role in facilitating the transport of Dysf to the damage site on the membrane, which strengthens the underlying interaction between Dysf and MG53 [22] (Figure 1.2).

MG53 was shown to be a component of the membrane repair machinery and a molecular complex formed by Dysf, Cav3 and MG53 was believed to be essential for the repair process [12, 22]. MG53 distributes both in the cytosol and on the plasma membrane and rapidly recruits to the membrane damage site in a manner of oxidation-dependent oligomerization [12] (Figure 1.2). Similar to Dysf, MG53 also interacts with PS and mediates vesicle accumulation at damaged membrane [12]. In contrast to Dysf, however, accumulation of MG53 during the membrane repair process is not Ca^{2+} but Zn^{2+}-dependent [12, 26]. MG53 deletion results in muscle pathology with defective repair of the damaged membrane [12, 22]. In addition to the function of membrane repair, MG53 also regulates membrane budding and exocytosis [27]. The two domains of MG53, TRIM and SPRY, contribute differentially to the localization of MG53. The SPRY domain was proven to perform a significant role in targeting of MG53 to the membrane, which may potentially influence the membrane repair function of MG53 [27].

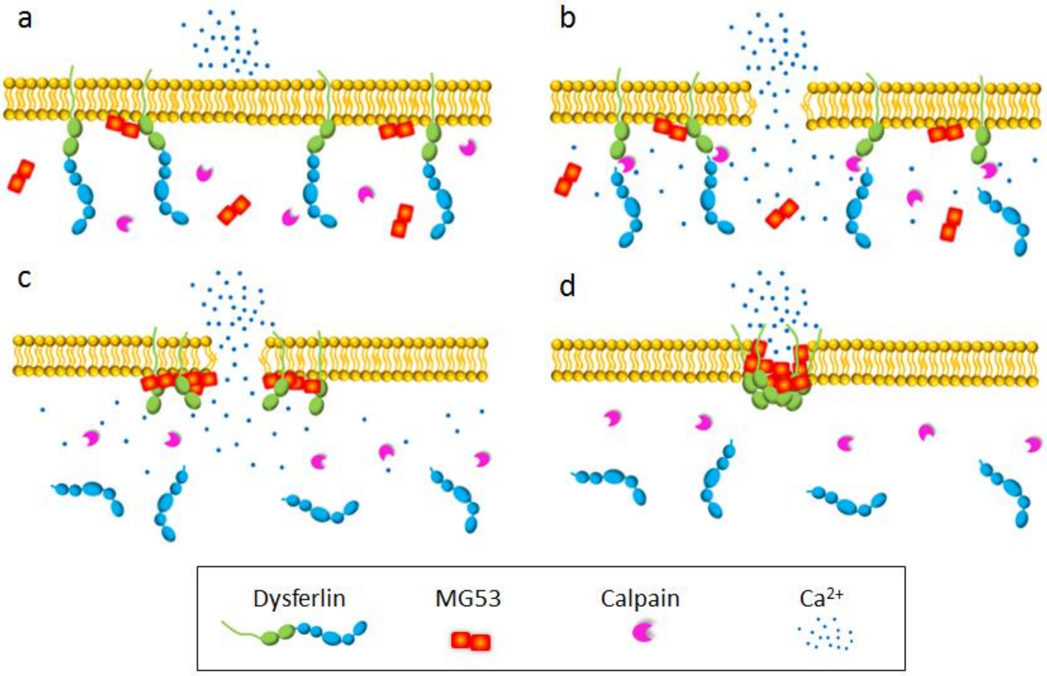

Figure 1.2: A schematic model for membrane repair. (a) Before membrane damage, the cytosolic calcium concentration is much lower than the extracellular environment. (b) Membrane damage causes an influx of calcium, which activates calpain to cleave the Dysf. (c) Mini-Dysf (green) and MG53 form an interdigitated lattice surrounding the injury site and (d) finally reseal the membrane injury and stop the calcium influx.

In this work, the function of Dysf and MG53 in the membrane repair process was studied both in zebrafish and mammalian cells. Zebrafish is an excellent model for studying membrane repair due to its short generation cycle, transparency during embryogenesis and availability of its genome sequence. Moreover, different mammalian cell lines were also used which have higher relevance to the human system. Different microscopic techniques were employed in this work to investigate the membrane repair process. In particular, by employing localization microscopy, the interaction between Dysf and PS, and their transport to the membrane lesion were directly observed and proven. The details will be discussed in Section 4.

1.2 Vesicle transport in fungal cells

The kingdom of fungi shows enormous diversity and can be classified as division, class, order, genus, and species. In this work, two different kinds of fungi, *Aspergilus nidulans* (*A. nidulans*) and *Ustilago maydis* (*U. maydis*), were employed to investigate the cytoplasmic transport of proteins and vesicles. As shown in Table 1.1, *A. nidulans* and *U. maydis* belong to the same subkingdom of dikarya, but different divisions [28, 29]. As a common property, both of the two fungi show polar growth: establishment and maintenance of the cells are based on a defined axis of polarity. Polar growth is an essential mechanism for a broad range of cell species, such as epithelial cells with apical-basal polarity, migrating cells and differentiating muscle cells and neurons [30, 31]. Likewise, prerequisite for filamentous growth of the hyphae is also polar growth. The highly polarized tubular cells and their growth along the hyphal tip provide a convenient model system to study polar growth. Moreover, pathogenicity and high secretion capability of fungi are also closely related to polarized hyphal growth.

	Aspergillus nidulans	Ustilago maydis
Kingdom	Fungi	Fungi
Subkingdom	Dikarya	Dikarya
Division	Ascomycota	Basidiomycota
Class	Eurotiomycetes	Ustilaginaomycetes
Order	Eurotiales	Ustilaginales
Genus	*Aspergillus*	*Ustilago*
Species	*Aspergillus nidulans*	*Ustilago maydis*

Table 1.1: Taxonomy of *A. nidulans* and *U. maydis*.

Polar growth of fungal hyphae is sustained by the continuous delivery of vesicles loaded with biomolecules to the hyphal tips [32, 33]. As shown in Figure 1.3, the long-distance transport of vesicles towards the cell apices is facilitated by arrays of microtubules and microtubule-dependent motor proteins [34]. In both *A. nidulans* and *U. maydis*, microtubules extend all the way to the hyphal tip, whereas actin cables are mainly localized close to the hyphal tip [32, 33]. In general, vesicles containing components for cell growth are transported first along microtubules from posterior area to the hyphal tip region, further transferred to actin cables and finally delivered to the apical site of the hypha [35–39]. Before fusion with the apical membrane, a structure called Spitzenkörper is formed by the accumulated vesicles at the hyphal apex [37]. The Spitzenkörper acts as a vesicle supply center, where various cargos for the apical region are sorted [38].

Typically, two kinds of vesicles are transported in fungal cells, secretory vesicles (SVs) and early endosomes (EEs) (Figure 1.3). SVs are formed and released from the trans-Golgi network [36, 40]. It has been observed that the gene deletion of kinesin-1 or myosin-5 decreases the amount of SVs at the hyphal tips and leads to severe growth retardation [36, 41, 42]. Kinesin-1 and myosin-5 are motor proteins, which interact with microtubules in the cytoplasm and actin cables at the hyphal tip, respectively [41, 43]. Therefore, it is believed that SVs are transported along microtubules by kinesin-1 and further along actin cables by myosin-5 to the apical membrane for exocytosis (Figure 1.3). However, as yet, there is still no direct observation of SV transport, probably due to the small size and fast motion of SVs. In contrast, EEs are much easier to track, and it has been reported that EEs transport bi-directionally along microtubules by the motor protein kinesin-3 and dynein [44–48].

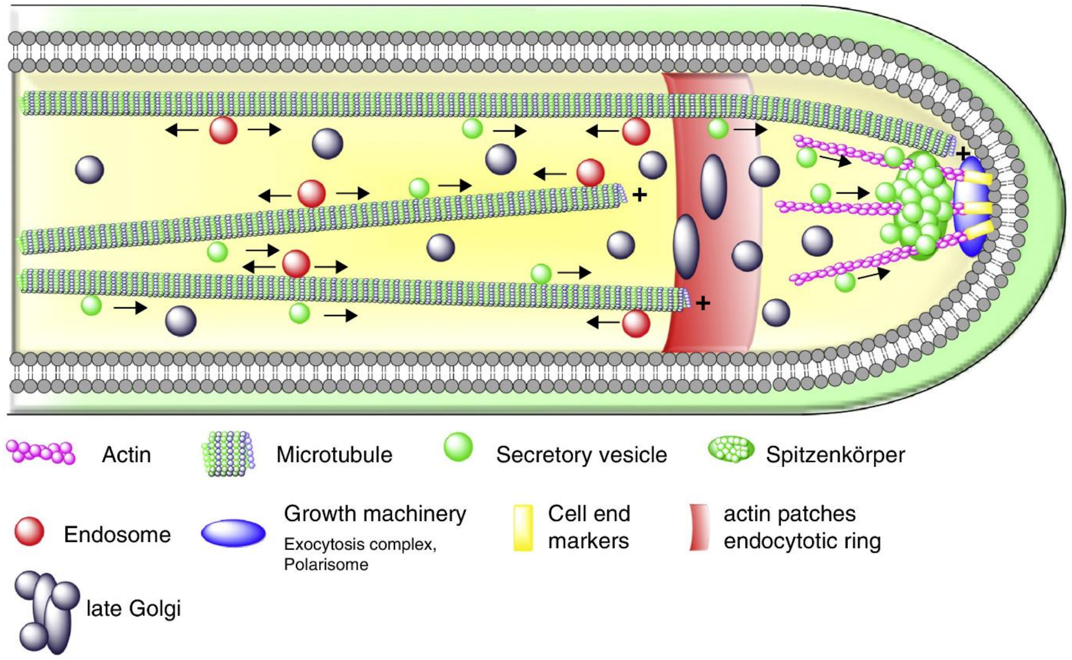

Figure 1.3: Scheme of vesicle transport in filamentous fungi. Image adopted from reference [36].

Many cargo proteins are involved in the processes of vesicle transport for cell growth. In *A. nidulans*, the construction materials for the cell wall, e.g., ChsB, a chitin synthase, need to be packaged and transported to the hyphal tip to support filamentous polar growth. Also, some components of spliceosomes such as the Num1 protein have also been shown to interact with motor proteins [48], indicating a potential involvement of the Num1 protein in the cytoplasmic transport system of *U. maydis*. The following sections will briefly introduce the ChsB and Num1 proteins and their roles in vesicles transport in *A. nidulans* and *U. maydis*, respectively.

1.2.1 The ChsB protein in *Aspergillus nidulans*

Filamentous fungi are covered by a cell wall consisting mainly of chitin and glucan. Chitin is a β-1,4-linked homopolymer of N-acetylglucosamine which is essential for building the cell wall on the hyphal apex for polar growth. Therefore, different kinds of chitin synthase, the enzyme for synthesis of chitin, are needed especially at the cell tip for hyphal morphogenesis [49]. As shown in Table 1.2, both *A. nidulans* and *U. maydis* have eight different chitin synthases, which can be classified into seven classes according to their structural properties [50]. In general, class III chitin synthases are fundamental for hyphal morphology and cell wall integrity of fungal cells [49]. For *A. nidulans*, six genes of chitin synthases have been isolated including two genes of class III. Among these, ChsB is known to play a crucial role in the maintenance of cell wall integrity for the polar growth of *A. nidulans* [51].

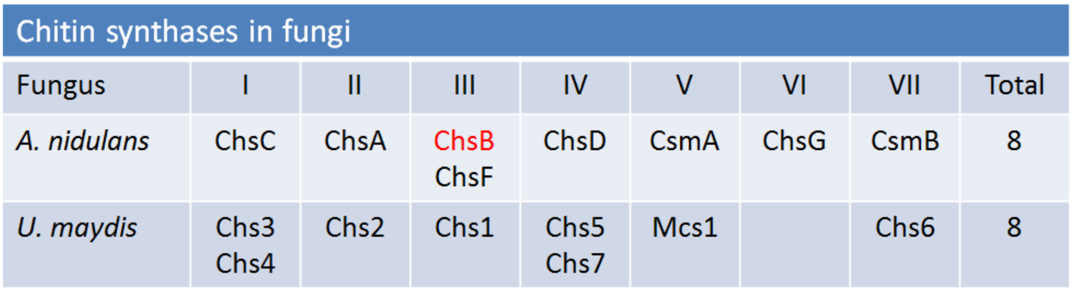

Chitin synthases in fungi

Fungus	I	II	III	IV	V	VI	VII	Total
A. nidulans	ChsC	ChsA	ChsB ChsF	ChsD	CsmA	ChsG	CsmB	8
U. maydis	Chs3 Chs4	Chs2	Chs1	Chs5 Chs7	Mcs1		Chs6	8

Table 1.2: Members of seven classes of chitin synthases in *A. nidulans* and *U. maydis* [52]**.** This work is focused on chitin synthase ChsB from *A. nidulans* (in red).

Chitin synthases can be transported via vesicles to the hyphal tips. However, the transport mechanism of these cell wall-related enzymes, such as ChsB, has remained elusive. It was reported that chitin synthases are transported on SVs to the plasma membrane on the hyphal tip for the synthesis of chitin [53]. Subsequently, chitin synthases localized on the plasma membrane can be internalized by endocytosis and transported on EEs for degradation in vacuoles, or recycled back to the membrane [53]. It has been shown in our previous work that kinesin-1 is required for transport of ChsB to the subapical region of *A. nidulans* fungal cells [54]. However, further investigation of the transport mechanism is limited by lacking direct visualization.

In this work, we have established localization microscopy-based high-speed pulse-chase imaging, as a robust biophysical approach to study the transport of ChsB-enriched vesicles in *A. nidulans* fungal cells. Furthermore, by using localization-based super-resolution imaging, we quantitatively analyzed the dynamics of the Spitzenkörper and the associated stepwise hyphal growth. The details will be discussed in Section 5.1.

1.2.2 The Num1 protein in *Ustilago maydis*

U. maydis belongs to the division of basidiomycete, and this phytopathogenic fungus can cause smut disease on corn (Zea mays). *U. maydis* displays a dimorphic life cycle with two stages: (1) a yeast-like, haploid sporidia stage, which divides by budding; (2) a dikaryotic filamentous fungi stage, which grows as a filament (Figure 1.4). The second phase starts with the conjugation tube formation from two sporidia [55]. The dikaryotic filament forms the appressorium and penetrates into the host plant to launch the biotrophic phase for further propagation [56].

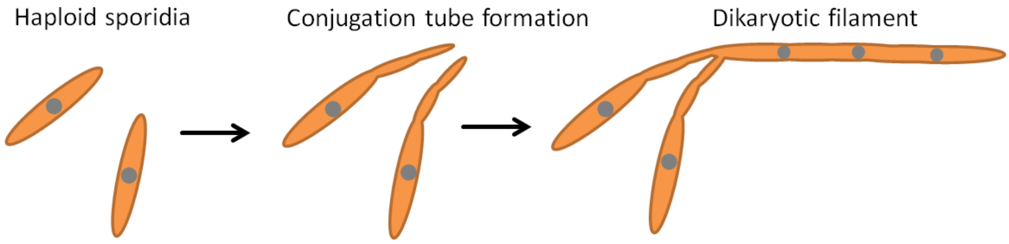

Figure 1.4: Developmental stages in the *U.maydis*. Haploid sporidia form conjugation tube and finally develop into the dikaryotic filament.

The development of *U. maydis* requires highly efficient cargo transport systems. Motor proteins, such as kinesin-1 and kinesin-3 transport vesicles in *U. maydis* along an array of antiparallel microtubules [57, 58]. The cargos include secretory vesicles, endosomes, peroxisomes, nuclei, but also mRNA, which passively travels on vesicles [58]. During pre-mRNA splicing, spliceosomes are needed for intron removal. The Num1 protein is homologous to SPF27, a core component of the evolutionarily conserved Prp19/CDC5 complex (NTC), which is an integral component of active spliceosomes [59]. In addition to regulating spliceosome formation and the splicing process, Num1 has also proven to perform a significant role in hyphal morphogenesis [48]. Moreover, Num1-containing complexes are also involved in the cellular response to DNA damage and cell cycle checkpoint control [60–67].

In previous work, Num1 was shown to physically interact with motor protein kinesin-1 and to be involved in the vesicle-mediated transport processes [48]. Further observations in Num1 deletion strains, such as altered polar growth, vacuolar morphology, dynein localization, as well as loss of the motility of early endosomes, strengthen the evidence of interaction between Num1 and kinesin-1[48]. Therefore, Num1 is an essential protein involved in splicing machinery and cytoplasmic trafficking.

According to our model, the Num1 protein is involved in the following three processes: (1) pre-mRNA splicing; (2) export of mRNA-particles through the nuclear pore; (3) microtubule-based mRNA-transport. To study the transport process, visualization of the cytoplasmic Num1 protein is of great importance. Num1 was shown to predominantly localize in the nucleus according to its function of pre-mRNA splicing [48]. With the Num1:GFP fusion protein, the existence of Num1 in the cytosol of *U. maydis* was also proven [48]. However, due to the weak signals and high background fluorescence from conventional optical microscopy, it was not possible to detect the precise cytoplasmic localization of Num1 proteins and the transport processes.

In this work, we have employed a photoactivatable fluorescent protein, EosFP [68, 69] and photoactivated localization microscopy (PALM) [8, 9, 70] to visualize the Num1 protein and study its transport mechanism in *U. maydis*. Our results provide clear evidence that, in addition to its function of pre-mRNA splicing in the nucleus, Num1 plays an additional role in the cytosol connected to the kinesin-1 motor protein. The details will be discussed in Section 5.2.

1.3 Outline of this work

This work focuses on sophisticated biological applications of localization microscopy. In Chapter 2, the fundamentals, the implementation, and the application of localization microscopy are explained. Details of sample preparation, PALM imaging, and data analysis are discussed in Chapter 3. Based on the improvement of the methods, we employed our localization-based microscopic technique to investigate two biological topics. Chapter 4 describes the membrane repair process in mammalian cells and zebrafish. In Chapter 5, the vesicle dynamics in fungal cells is presented. Finally, the whole work is summarized in Chapter 6.

2. Localization-based super-resolution microscopy

2.1 Resolution limit

In the 17th century, the Dutch inventor Antoni van Leeuwenhoek was the first to use a single-lens microscope to observe cells. Since then, a large number of developments of optical far-field microscopy techniques have led to significant improvements of the image quality. In 1873, the German physicist Abbe realized that the resolution of far-field optical microscopes is limited by the diffraction of light [71]. The Abbe limit can be described by the formula

$$d = 0.5 \cdot \lambda / NA. \tag{2.1}$$

The λ is the wavelength of light, and the numerical aperture (NA) of an objective lens is defined as

$$NA = n \cdot \sin\theta, \tag{2.2}$$

where n is the refractive index of the imaging medium and θ is the half angle over which the objective can collect light from the sample. Therefore, even with an infinite aperture of the objective lens (θ = 90°), the resolution remains finite. The Abbe criterion states that a microscope cannot resolve two objects with a distance smaller than the Abbe limit *d* (Equation 2.1). In 1903, a similar theory was presented by Lord Rayleigh, which is also called Rayleigh criterion [72].

Images are composed of an array of diffraction-limited spots with different intensity, which overlap to produce the final image. Each point object imaged after a perfect lens with a circular aperture at the focal plane forms the so-called Airy disk or Airy pattern due to the diffraction of light. As shown in Figure 2.1, an Airy pattern consists of a central spot (the 0th order) surrounded by series of diffraction rings (higher orders). Therefore, the image resolution is normally determined by the ability to distinguish the maxima of the 0th order from close Airy patterns by means of intensity contrast.

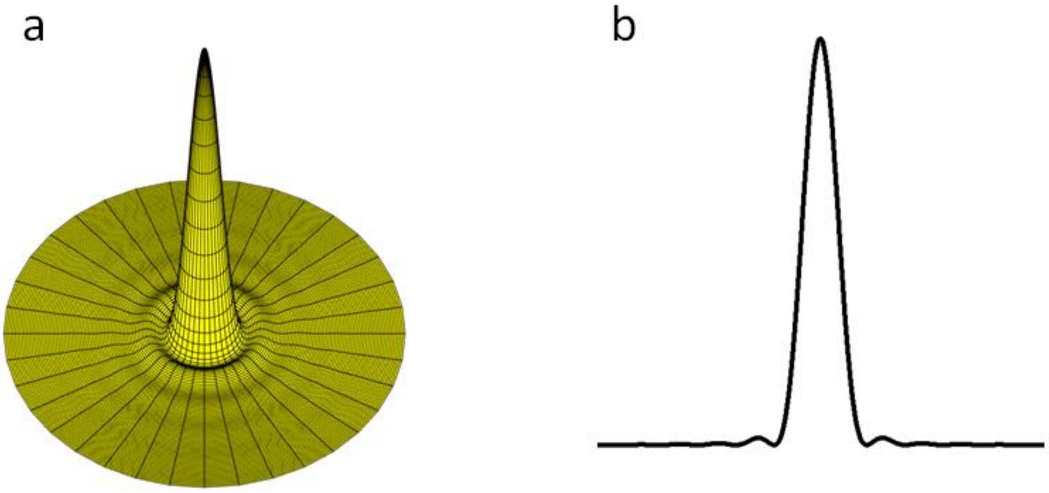

Figure 2.1: 3D and 2D profiles of the Airy pattern.

The most popular one is the Rayleigh criterion, which states that the two objects can be distinguished if the first minimum of the Airy pattern overlaps with the central maximum (0^{th} order) of another Airy profile. Based on the Rayleigh criterion, the minimum distance between the two objects (r) can be defined as

$$r = 0.61 \cdot \lambda / NA. \tag{2.3}$$

With this distance, the overlapped profile of two Airy patterns shows a sharp dip between two peaks (Figure 2.2, left). As mentioned above, the Rayleigh criterion (Equation 2.3) is very similar to Abbe's law (Abbe's criterion) (Equation 2.1), which is only different in the coefficient. The resolution limit defined by Abbe's criterion is also plotted in Figure 2.2 (middle), and the small dip is still distinct between two maxima. Besides these two criterions, another convention, Sparrow criterion, is often used to define the minimum distance for resolving two distinct objects. Different with Rayleigh and Abbe criterion, the coefficient of the Sparrow criterion is 0.47, and with this parameter, the sum of the two Airy patterns produced a flat intensity profile as shown in Figure 2.2 (right). In the case of imaging a sample labeled with the green fluorescent protein (GFP, maximum emission at 510 nm) using an objective with the NA of 1.4, the resolution limit based on Rayleigh, Abbe, and Sparrow criterions are 222 nm, 182 nm, and 171 nm, respectively.

This diffraction limit of optical microscopy was considered as an unbreakable law for over a century. Since 1994, however, several new exciting strategies have been developed, which can 'break' the rule under certain circumstances, such as stimulated emission depletion microscopy (STED) [6], saturated structured illumination microscopy (SSIM) [7] and localization-based super-resolution microscopy, such as photoactivated localization microscopy (PALM) [8] and stochastic optical reconstruction microscopy (STORM) [9]. This work will focus on localization-based super-resolution techniques.

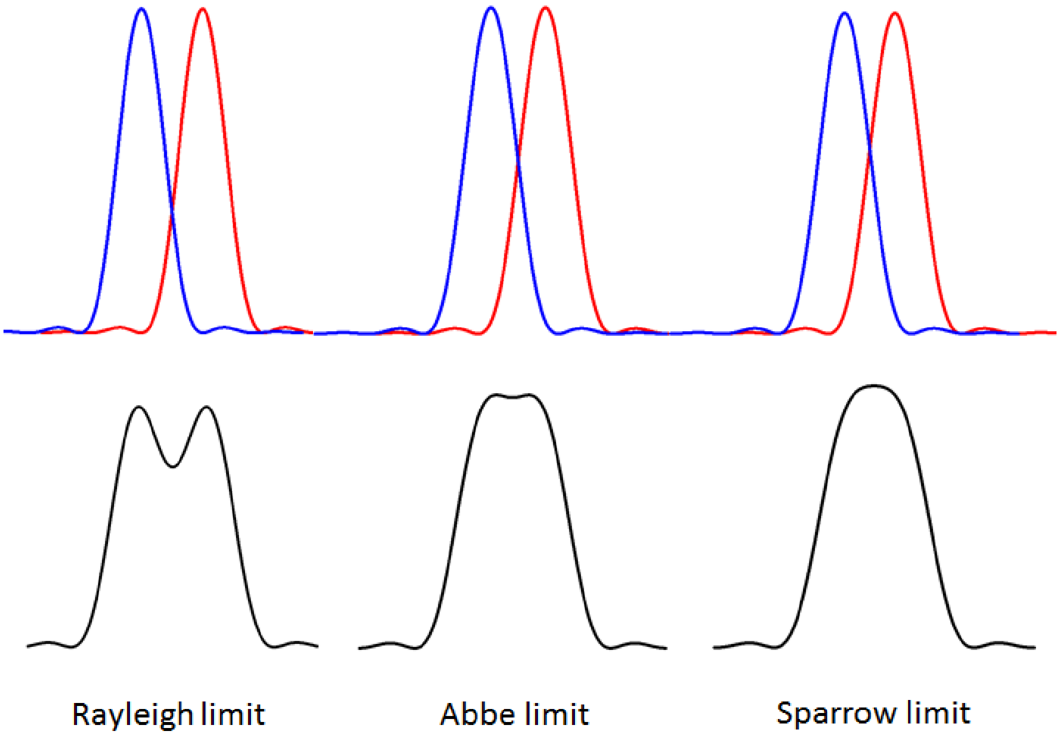

Figure 2.2: Three criteria of the resolution limit. Two Airy profiles are plotted based on the Rayleigh, Abbe and Sparrow criteria, respectively (upper panel). The respective summed profiles are shown in the lower panel.

2.2 Localization-based super-resolution imaging

2.2.1 Principle of localization microscopy

For far-field optical microscopy, each single point object will be blurred into a spot because of diffraction. The intensity distribution of the spot is called the point spread function (PSF), which in an ideal condition without any aberration is an Airy pattern as discussed in the last section. Fluorescent microscopes are incoherent imaging systems, which means every single fluorescent probe from the specimen is independently imaged, and their simultaneously fluorescent emission will not affect each other. Therefore, the resulting image is the sum of the PSFs of the individual probes in the sample (Figure 2.3a). Apparently, fluorescent probes with mutual distance smaller than the width of PSF will show an overlapping image and cannot be resolved (Figure 2.3a).

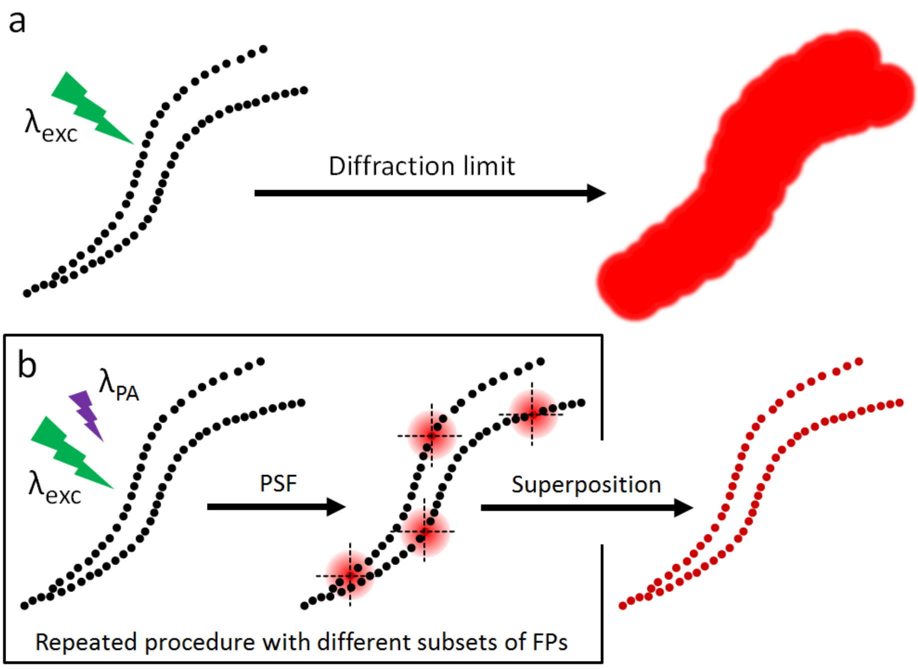

Figure 2.3: Comparison of imaging with a conventional microscopy and PALM. (a) Diffraction limits the image resolution. (b) The principle of the PALM technique for super-resolution imaging as described in the text. Image adopted from reference [73].

This situation changed dramatically when people realized that the overlapping PSFs of the fluorophores could be separated in the time domain by stochastically switching the fluorophores between a non-emitting (dark) state and an emitting (fluorescent) state [8, 9, 70]. The concept is controlled activation, which leads to only a small subset of the fluorophores being photoactivated to the fluorescent state while the majority stays in the dark state. The activated individual fluorophores occur stochastically and sparsely distributed and, therefore, avoid the spatial overlap problem (Figure 2.3b). The position of each fluorophore can be precisely determined by calculating the centroid of the PSF. After the imaged fluorophores are bleached or switched to the dark state, a new subset of fluorophores is activated to their fluorescent state for subsequent imaging. This procedure is repeated until all the fluorophores are captured and localized. As a final step, all calculated positions are combined and plotted to reconstruct a super-resolution image (Figure 2.3b). PALM and STORM are two prevalent localization-based microscopic techniques, which are based on imaging of photoactivatble fluorescent proteins or photoswitchable dyes, respectively.

2.2.2 Image resolution of localization microscopy

The optical resolution of localization microscopy is not limited by diffraction but determined by the localization precision of the individual fluorophores. Theoretically, the variance of the localization uncertainty was well established in [74] as

$$(\Delta x)^2 = \frac{s^2}{N} + \frac{a^2}{12N} + \frac{8\pi s^4 b^2}{a^2 N^2}, \tag{2.4}$$

where *s* is the standard deviation of the PSF of the microscope, *N* is the number of photons collected, *a* is the size of the pixel in the image, and *b* is the background noise. With a perfect detector, the localization uncertainty is only related to the first term of the equation, determined by the PSF and photon number. However, a camera detector is subdivided into individual pixels, which will lead to pixelation noise which raises the uncertainty. Finally, the third term represents the uncertainty due to background noise [74]. Of note, the pixel size of the image influences both the pixelation noise (the second term) as well as the background noise (the third term). With smaller pixel size, the pixelation noise decreases, whereas the background noise increases. The transition between the two terms occurs at

$$\frac{a^2}{12N} = \frac{8\pi s^4 b^2}{a^2 N^2}. \tag{2.5}$$

Accordingly, the best ratio of the pixel size to the standard deviation of the PSF occurs if

$$\frac{a}{s} = \sqrt[4]{\frac{96\pi b^2}{N}}. \tag{2.6}$$

Therefore, for most cases, the pixel size should be about equal to the standard deviation of the PSF [74]. Considering that fluorescent proteins typically have a lower photon number yield than fluorescent dyes, the pixel size in PALM imaging is generally set to 100 – 130 nm [29, 30], which is a bit larger than in STORM imaging (70 – 100 nm [35]).

Experimentally, the localization precision can be determined by calculating the standard deviation (SD) of the localization distribution measured repetitively from the same single fluorophore. In some literature reports, the localization precision is also defined by the full width at half maximum (FWHM) of the distribution of measured localizations, which corresponds to the smallest displacement between two fluorophores that can be resolved. For the Gaussian distribution,

$$FWHM = 2\sqrt{2\ln 2}\,SD \approx 2.35\,SD. \tag{2.7}$$

Of note, one should avoid potential confusion when comparing localization precisions from different measurements.

Another frequent conceptual confusion is between localization precision and localization accuracy. Localization accuracy has an entirely different meaning than the localization precision discussed above. If the microscope and the algorithm are unbiased to estimate the locations of the individual fluorophore, the mean of the detected locations ($\overline{x}_p$, $\overline{y}_p$) approaches the real position of the fluorophore (x_p, y_p) with an increasing number of detected locations. When the system is biased, the average location predicts the wrong position (Figure 2.4).

Apparently, the biased system is inaccurate with a nonzero localization accuracy Δ_{xy}, which is defined as the distance between the true and the predicted incorrect positions (Figure 2.4) [76]. In principle, the localization accuracy is not sensitive to background noise. However, other factors such as spatial distribution of photons and the properties of detectors and samples can lead to a biased system and significantly affect the localization accuracy [76].

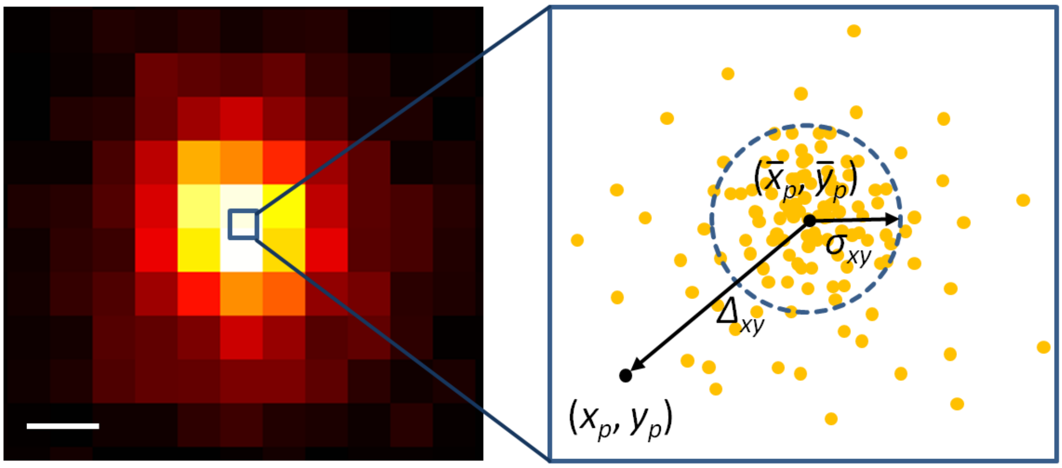

Figure 2.4 Illustration of localization precision and accuracy. Positions of the same emitter from different images are plotted as yellow spots. In this biased system, the averaged location $(\bar{x}_p, \bar{y}_p)$ with the localization precision σ_{xy}, however, predicts only a wrong position. The distance between the real position (x_p, y_p) and the measured position $(\bar{x}_p, \bar{y}_p)$ is defined as the localization accuracy Δ_{xy} of the system. Image adopted from reference [76].

For continuous structures, the labeling density of fluorophores also significantly influences the image quality. The effects of labeling density can be quantified by using the Nyquist-Shannon criterion, which states that a spatial structure smaller than twice the average label-to-label distance cannot be resolved [77, 78]. The Nyquist resolution is given by $2/N^{1/D}$, where N is the number density of labels and D is the dimension of the structure. If the localization precision is significantly smaller than the average localization spacing, the Nyquist resolution dominates the overall image resolution. For a 2D PALM image with a localization precision of ~30 nm, a labeling density of ~5000/μm^2 is required to achieve the matching Nyquist resolution. When the localization precision and Nyquist resolution are comparable, a heuristic argument has been proposed that the overall resolution approximately equals the root sum square of the localization precision and the mean localization spacing [79],

$$\text{Overall Resolution} = \sqrt{\text{localization precision}^2 + \text{Nyquist resolution}^2}. \qquad (2.8)$$

2.2.3 Limitations of localization microscopy

The central principle of localization microscopy is to disperse the image information in time by taking many images, so that the molecules are sparsely distributed within an individual image frame. The acquired PSFs need to be accurately fitted to calculate the centroid with subdiffraction precision. However, even with the simplest Gaussian fit, the calculation of the raw data still takes several hours to achieve a super-resolution image. Therefore, unlike in conventional fluorescent microscopy, the real-time visualization in localization microscopy is still challenging. Several previous works reported real-time super-resolution observation [80, 81]. However, simpler fitting algorithms such as the modified center of mass algorithm [80] and the fluoroBancroft algorithm [81] were employed in these works to reduce the processing time. Apparently, there is a trade-off between the calculation precision and the processing speed. To achieve real-time super-resolution visualization, both the fitting algorithm as well as the computer hardware need further development.

Another trade-off is between spatial and temporal resolution. As discussed in the last section, a higher spatial resolution requires more detected molecules to fulfill the Nyquist criterion, therefore a longer acquisition time. Recently, video-rate localization microscopy has been reported by employing an advanced scientific complementary metal-oxide semiconductor (sCMOS) camera with its reduced data acquisition time [82]. However, this technique is still quite limited by the dynamic process of the structure, the labeling density of the sample and, in particular, the properties of fluorescent probes, such as brightness and blinking.

Indeed, the fluorescent probe is also a limitation for localization microscopy. Fluorescent probes with optimum optical properties will significantly improve the imaging quality. In recent years, both fluorescent proteins and organic dyes suitable for localization microscopy have been developed rapidly. These fluorescent probes will be discussed in the following section.

2.3 Fluorescent probes for localization microscopy

The proper selection of fluorescent probes for different applications is essential for localization-based super-resolution imaging. As discussed above, localization microscopy depends on the fluorescent probes which can switch between dark and emitting states. Photoactivatable fluorescent proteins (FPs) and organic dyes are two major groups of fluorescent probes that are widely used. Both have distinct advantages and disadvantages for various imaging applications. In this section, the general overview of FPs and organic dyes for super-resolution localization microscopy are discussed.

2.3.1 Fluorescent proteins

In 1962, the green fluorescent protein from the jellyfish *Aequorea victoria* (avGFP) was first isolated by Osamu Shimomura [83]. Cloning of the avGFP gene by Prasher in 1992 and the recombinant expression of avGFP in *Escherichia coli* and *Caenorhabditis elegans* by Martin Chalfie in 1994 provided a fundamental method of functional expression of avGFP [84, 85]. Since then, labeling of cells and organisms with fluorescent proteins became a widely used tool, and in 2008 the Nobel Prize in Chemistry was awarded to Shimomura, Chalfie and Tsien ‘for the discovery of the green fluorescent protein’ [83, 86]. However, these FPs are not suitable for localization microscopy. In recent years, so-called photoactivatable FPs (PA-FPs) have been developed and widely applied in localization microscopy due to their special photoactivation properties [87–89].

In general, PA-FPs can be classified as photoconvertible (irreversible photoactivation) and photoswitchable (reversible photoactivation) FPs [86]. In photoconvertible FPs, a permanent photochemical modification happens and converts the FPs from a nonfluorescent (dark) state to a fluorescent (bright) state or from one emission wavelength to another irreversibly. Therefore, photoconvertible FPs include dark to bright photoconvertible FPs, e.g., PA-GFP, PA-mCherry [90, 91], and also photoshiftable FPs that can shift their emission colors, e.g., EosFP [68]. Photoswitchable FPs can switch between a dark-off state and a bright-on state reversibly controlled by the light. Photoswitchable PFs can be further classified into two groups, positive photoswitchers (e.g., Padron [92]) and negative photoswitchers (e.g., Dronpa [93], mIrisFP [94]), with the irradiation at the excitation wavelength populating the fluorescent or non-fluorescent state, respectively.

Compared with irreversible PA-FPs, reversible ones are not ideal markers for localization microscopy. To achieve a high localization precision, a high emitted photon number from each single emitter is necessary. Therefore, the excitation light should be considerable intense. For positive photoswitchers, the high-power excitation light, however, also leads to excessive photoactivation. Thus, the density of the activated photoswitchers becomes too high for the detection of individual emitters. Whereas, negative photoswitchers with high-power excitation are quickly switched off even before emitting the full photon budget [86]. Moreover, photoswitchable FPs suffer from lower contrast ratio between bright and dark states than photoconvertible FPs [86]. Therefore, photoconvertible FPs are better probes for super-resolution PALM imaging.

In this work, the photoconvertible FP, mEosFP*thermo*, was used for PALM imaging in various biological applications due to its prominent optical properties, e.g., high photon number and contrast ratio [95]. mEosFP*thermo* was engineered from EosFP, a GFP-liked tetrameric protein isolated from the reef coral *Lobophyllia hemprichii* [68]. Because oligomerization is often detrimental in applications requiring functional fusion constructs, dimeric (EosFP V123T; EosFP T158H) and a monomeric variant (EosFP V123T, T158H) have been generated by protein engineering [68]. The monomeric variant (EosFP V123T, T158H), with the additional mutation, A69V, displays high thermotolerance and good expression at 37 °C and is well suitable for cell imaging [94, 95]. As a photoconvertible fluorescent protein, the absorption and emission of mEosFP*thermo* can be converted from green to the red by the illumination with violet light [69] (Figure 2.5). The signals collected in the red channel shows as separated events and the sparse distribution of molecules ensures precise detection and localization in a single molecule level.

The prominent advantage of FPs is that they can be easily fused with target proteins, providing a convenient method for live cell imaging. However, compared with organic dyes, FPs have inferior photophysical properties, especially low photon budget. Thus, the localization precision is worse than with dyes.

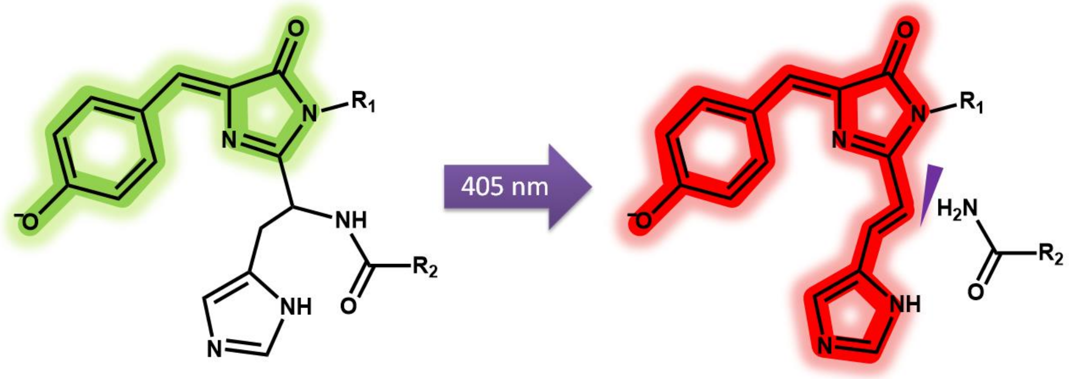

Figure 2.5: Photoconversion of the EosFP chromophore from green to red. Fluorescence emission converts from green (516 nm) to red (581 nm) after exposure to a violet light (405 nm), which leads to irreversible cleavage of the peptide backbone between C_α and N_α of the histidine [69]. Image adopted from reference [96].

2.3.2 Organic dyes

Organic photoswitchable dyes are also widely used in localization-based super-resolution imaging due to their excellent brightness (photon number per switching cycle), which can significantly improve the localization precision. Moreover, other properties of the dyes, such as on-off duty ratio, the number of switching cycles and sensitivity to light activation are also of great importance to the quality of the super-resolution images [97]. These switching properties of various dyes have been well studied in [97], and several photoswitchable dyes with different emission bands with excellent performance have been identified, e.g., Alexa Fluor 488, Cy3B and Alexa Fluor 647. Of note, to achieve the best performance of the dyes, chemical additives such as thiols and oxygen scavengers are used in the imaging buffer. The imaging buffers also need to be carefully selected for different dyes and imaging conditions, e.g., β-mercaptoethanol is much more toxic to live cells than glutathione or ascorbic acid, which have proven to be more appropriate compatible reducing agents for live-cell imaging [98]. Recently, a new technique, DNA-PAINT (point accumulation for imaging in nanoscale topography [99]) has been fast developed [100]. By employing the transient binding of short fluorescent dye-labeled oligonucleotides, super-resolution images can be achieved without any redox buffer to enhance the switching property of dyes.

Organic dyes have better photophysical properties than fluorescent proteins. However, the main drawback is the labeling problem in live cells. Typically, STORM imaging has been done on fixed cells using antibodies to label the protein of interest. For live-cell imaging, a particular tag, such as SNAP or Halo, can be fused to the protein of interest for further binding to the dye molecules [101, 102]. However, typical dyes with outstanding photophysical properties, e.g., Alexa Fluor 647 and Cy5, are not membrane permeable. Therefore, additional efforts, such as electroporation [101] or employing streptolysin O [103], a bacterial toxin which forms temporary pores in cell membrane, are necessary for delivering dyes into the cells, which, however, not only increase the experimental complexity but also lead to a decrease in cell viability.

2.4 Implementation of a localization microscope

2.4.1 Instrumentation

Localization microscopy needs specific hardware components, such as the microscope frame with a high-resolution mechanical stage, lasers, high-NA objectives, detectors and a data acquisition computer.

For localization microscopy, suitable lasers for excitation and activation are necessary. Especially for excitation, a high-power laser is required to ensure a high flux of emitted photons for fast imaging and precise calculation of localizations. In general, free-space lasers are directly coupled (without any optical fiber) into the microscope to achieve maximum power. Typically, for PALM imaging of PA-FPs, lasers with a power of 50 – 200 mW are sufficient for excitation and detection. For STORM imaging of organic dyes, stronger laser sources (100 – 500 mW) are needed to acquire the whole photon budget from dyes within the typical camera exposure time of 10 – 200 ms. Of course, the required laser power also depends on the illumination area and the camera acquisition speed.

A high-NA objective is needed to collect as many photons as possible. Some biological applications focus on proteins at the bottom membrane of adherent cells or cytoskeleton structures (actin or microtubules) close to the cells' bottom surface. Thus, for these applications, instead of epi-illumination, the total internal reflection fluorescence (TIRF) technique is employed. As shown in Figure 2.6a, under epi-illumination, the excitation beam is focused on the back focal plane of the objective and parallel light after the objective can illuminate the whole thick sample. However, in TIRF mode, the incident angle of the beam exceeds the critical angle, resulting in total internal reflection at the coverslip (Figure 2.6b). Only the evanescent wave can penetrate approximately 100 nm into the sample and excite the fluorophores in a region very close to the coverslip. Hence, there is no background fluorescence from the upper layer of the sample.

For TIRF imaging in localization microscopy, the NA of the objective should be greater than the refractive index of the sample medium, e.g., water ($n \approx 1.33$). In practice, objectives designed for TIRF imaging with an NA of 1.46 or more are available. The choice of a suitable coverslip thickness is also important. Typically, most high-NA objectives are designed to work with coverslips with a thickness of ~170 µm. Finally, as discussed in section 2.2.2, the pixel size in the raw images should be ~100 nm to reach the optimum imaging condition for high localization precision. Therefore, the magnification of the objective and a suitable tube lens should be carefully selected to match the pixel size of the detector.

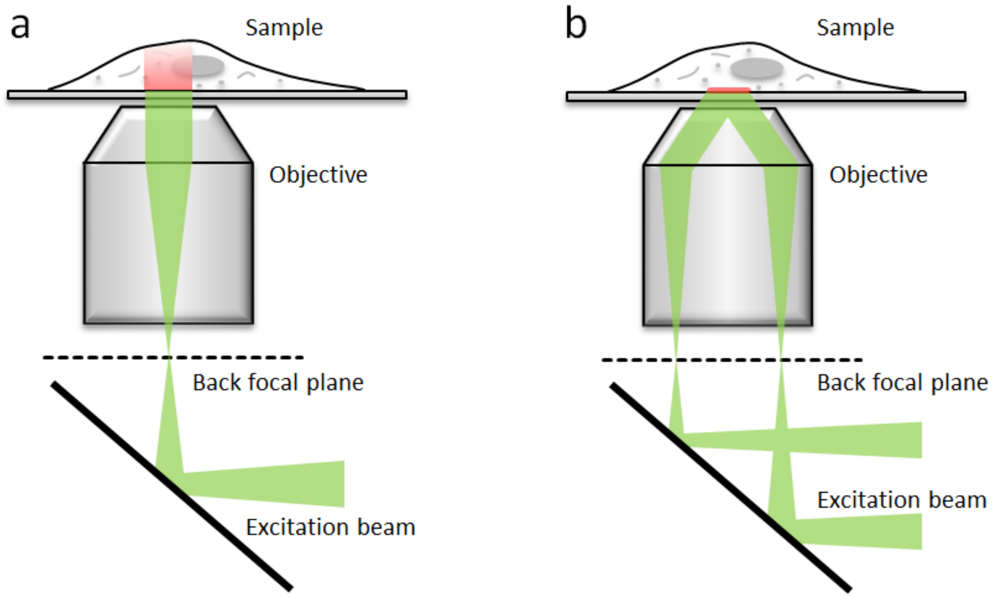

Figure 2.6: Configuration of epi-illumination and TIRF imaging modes. (a) Epi-illumination mode. (b) TIRF mode.

Back-illuminated electron-multiplying charge-coupled devices (EMCCDs) are mostly used for localization microscopy due to their low readout noise and capability of detecting low numbers of photons. Especially, if the number of photons per pixel is less than 100, and the frame rate is less than 100 Hz, the level of noise introduced by the camera remains negligible [77]. Recently, newly developed scientific complementary metal-oxide semiconductor (sCMOS) cameras have been used in localization microscopy, featuring faster data acquisition speed, larger field of view and higher effective quantum efficiency [82]. However, the pixel-dependent noise of the sCMOS camera is non-negligible, which can lead to severe localization artifacts. Therefore, the raw images taken by sCMOS camera need to be carefully calibrated based on the intrinsic properties of each pixel, such as offset, gain, and variance. The sCMOS camera-specific calibration processes and algorithms have been discussed in reference [82].

2.4.2 Software

Localization algorithms play a major role in localization microscopy. In general, the algorithm contains three parts: (1) detection of molecules; (2) localization of molecules; (3) image reconstruction. The core of the algorithm is the second part, the localization of the molecules, which has developed quickly in the past decade [104–108]. Typically, localization algorithms can be separated into two groups, non-fitting methods (e.g., center-of-mass algorithm [80], fluoroBancroft algorithm [104], radial symmetry [106]) and fitting methods (e.g., least squares criteria [74], maximum likelihood criteria [109]). There is always a trade-off between calculation speed and localization precision. Typically, fitting methods with their better localization precision are preferred.

Besides step (2), step (1), detection of molecules, can also dramatically influence the efficiency and reliability of the localization calculation. The main problem is the temporal and spatial heterogeneity of background, which arises from the inherent nature of the sample, photobleaching of the fluorescent markers or technical issues, such as the inhomogeneous illumination of the sample and fluctuations of the laser intensity [110]. These problems have been well solved with the published algorithm, a-livePALM, which has been developed previously in our group by Dr. Yiming Li [110]. The algorithm evaluates the background information in a larger region surrounding the local detection area for searching molecules. As shown in Figure 2.7, after loading the raw images, background estimation and Gaussian noise filtering are run in parallel in the central processing unit (CPU) and the graphics processing unit (GPU). The calculation region is defined considering the detected background information. Local maxima are then searched in the designated calculation region, followed by the localization calculation based on the maximum likelihood estimator (MLE) algorithm [109].

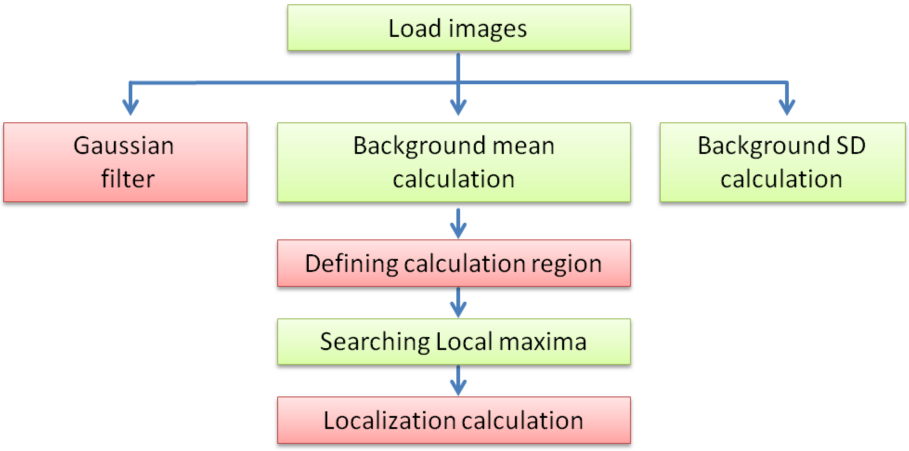

Figure 2.7: Flowchart of the a-livePALM algorithm. Green- and red-color boxes represent the procedures run in the CPU and GPU, respectively. Image adopted from reference [110].

Recently, a comprehensive evaluation of various localization software packages was published [111]. The algorithms were evaluated with respect to various features, such as detection rate, localization precision, quality of the reconstructed image, image resolution, software usability and computational resources. The a-livePALM software attained a high cumulative grade with its excellent performance. Therefore, the a-livePALM algorithm was used in this work for most of the data analysis.

2.5 Beyond imaging – analysis of dynamics

2.5.1 Analysis of dynamics based on localization detection

Dynamic information of membrane proteins in live cells can provide profound insights into many cellular events. Tracking of membrane proteins can be achieved by conjugating the protein of interest with gold beads [112] or normal fluorescent proteins [113]. However, with these methods, only a tiny fraction of membrane proteins can be labeled and measured because the separation of the particles needs to be greater than the diffraction limit. With localization microscopy, sub-diffraction localizations of proteins can be acquired in live cells by labeling the protein of interests with PA-FPs. By employing algorithms for trajectory analysis, such as sptPALM (single-particle tracking PALM), high-density trajectory maps of labeled membrane proteins can be obtained [114]. The strategy of sptPALM is shown in Figure 2.8.

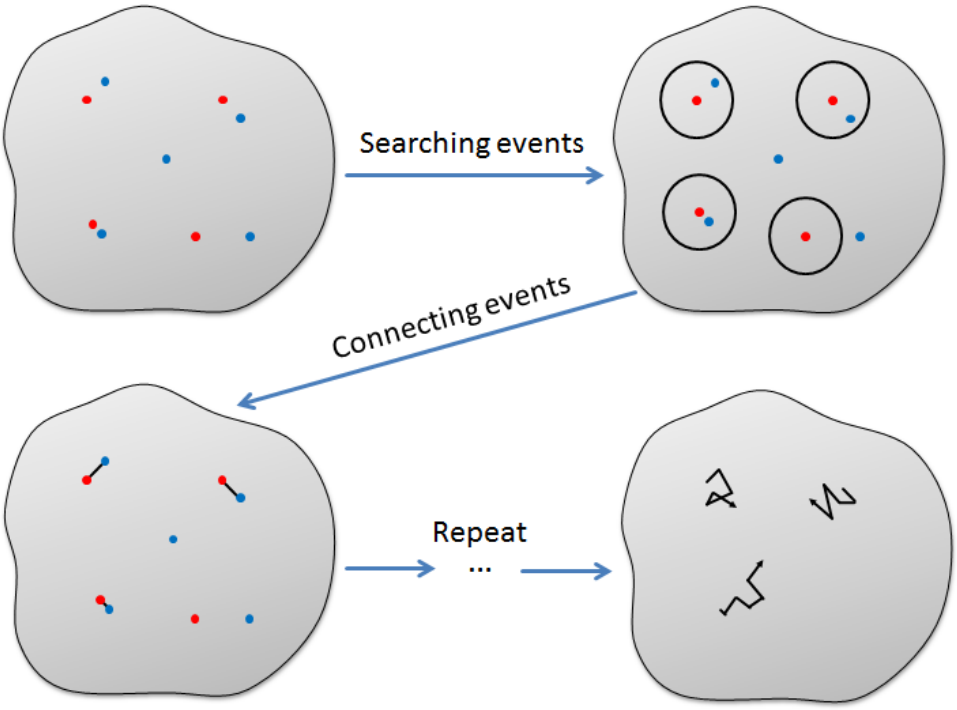

Figure 2.8: Schematic of sptPALM analysis. Localizations of fluorescence events from consecutive frames (the first frame: red dots; the second frame: blue dots) are connected according to their proximity. These processes are repeated to obtain trajectories of single particles. Image adopted from reference [114].

PA-FPs are fused with the protein of interests and expressed in the cultured cell. Raw images of the fluorescence events are taken in the TIRF mode. After photoactivation of the FPs, single molecules can be localized with sub-diffraction precision. As shown in Figure 2.8, fluorescence events from consecutive frames, e.g., the first frame (red spots) and the second frame (blue spots), can be linked according to their proximity. Therefore, the maximum distance between the two linked events needs to be carefully set based on the diffusional motions of the membrane protein. By repeating the activation, imaging and bleach processes, multiple ensembles of molecules can be measured to obtain high-density single-molecule trajectories, up to ~ 50 per µm^2 [114].

With the huge amount of trajectories, the motion behavior can be statistically analyzed. The most common approach is to study the dynamic properties of the proteins of interest by analyzing the mean square displacement (MSD) as a function of time. In general, the membrane motion can be classified into three types: diffusive, directed and confined. By performing MSD analysis, the motion types and their relative parameters, e.g., size of confinement domain (confined), diffusion coefficient (diffusive) and transport velocity (directed) can be readily determined. Normal and anomalous diffusion in 2D can be described by

$$MSD = \Gamma t^{\alpha}, \tag{2.9}$$

where

$$MSD = \langle (x_t - x_0)^2 \rangle + \langle (y_t - y_0)^2 \rangle. \tag{2.10}$$

Γ is the transport coefficient, t is the time interval and α determines the motion type: anomalous subdiffusion (α < 1), anomalous super diffusion (α > 1) and normal diffusion (Brownian diffusion) (α = 1) [115, 116]. (x_t , y_t) are the two-dimensional Cartesian coordinates of the molecule at the t^{th} position of its trajectory. For anomalous diffusion, the diffusion coefficient is time-dependent with

$$D\,(t) = \frac{1}{4}\Gamma t^{\alpha-1}\,. \tag{2.11}$$

For normal diffusion, the MSD is proportional to the time interval with

$$MSD = \Gamma t, \tag{2.12}$$

and the diffusion coefficient is a constant with

$$D = \frac{1}{4}\Gamma. \tag{2.13}$$

Therefore, for the diffusive behavior of membrane proteins, the diffusion coefficient can be statistically calculated through MSD analysis base on a large number of molecule trajectories acquired by sptPALM.

Recently, the single-molecule diffusional-mobility-shift assay (smDIMSA), was published, which provides a simple method to study ligand-receptor interactions based on sptPALM [117]. The central idea is that the diffusional mobility of the membrane receptor is sensitive to the size of the water-soluble binders. Therefore, by detecting the diffusional mobility shift of membrane receptors in the presence and absence of ligands, the ligand-receptor interactions in the intact membrane of living cells can be quantitatively studied without ligand labeling [117].

2.5.2 Analysis of dynamics based on a pulse-chase experiment

The photoactivation property of PA-FPs can also be employed for a pulse-chase experiment, which is a potent tool to study the dynamics of labeled proteins or intracellular vesicles. In general, PA-FPs are first activated by a pulse of light, followed by tracking of the activated molecules until photobleaching.

Tracking of normal FPs needs continuous imaging to follow the targets, which leads to considerable bleaching of the FPs and phototoxicity of the cells. Differently, PA-FPs can be photoactivated in arbitrarily selected region, and the surrounding area stays dark (Figure 2.9). Therefore, the diffusion of activated molecules can be readily monitored without continuous long-time excitation and visualization. With this technique, the photobleaching and phototoxicity problems are relieved, and moreover, the spatio-temporal limits of the observation of biological dynamics are dramatically extended [87]. As shown in Figure 2.9, several dynamic processes can be studied with this technique: (1) the movement of cytoplasmic or membrane proteins, e.g., movement rate and direction, diffusion coefficient, the mobile and immobile fractions (Figure 2.9a); (2) transport of vesicles, e.g., secretory vesicles and endosomes (Figure 2.9b); (3) dynamics of organelles, e.g., fission and fusion of the mitochondria (Figure 2.9c).

Within the large variety of PA-FPs, green-to-red photoconvertible fluorescent proteins, such as EosFP, are particularly superior for the pulse-chase experiment because of their high optical contrast between green and red emitting states [95]. Further, fluorescent proteins which combine photoconversion and photoswitching, such as mIrisFP [94], even offer the possibility of using a pulse-chase experiment in conjunction with super-resolution imaging for single particle tracking in the protein dynamic processes [98].

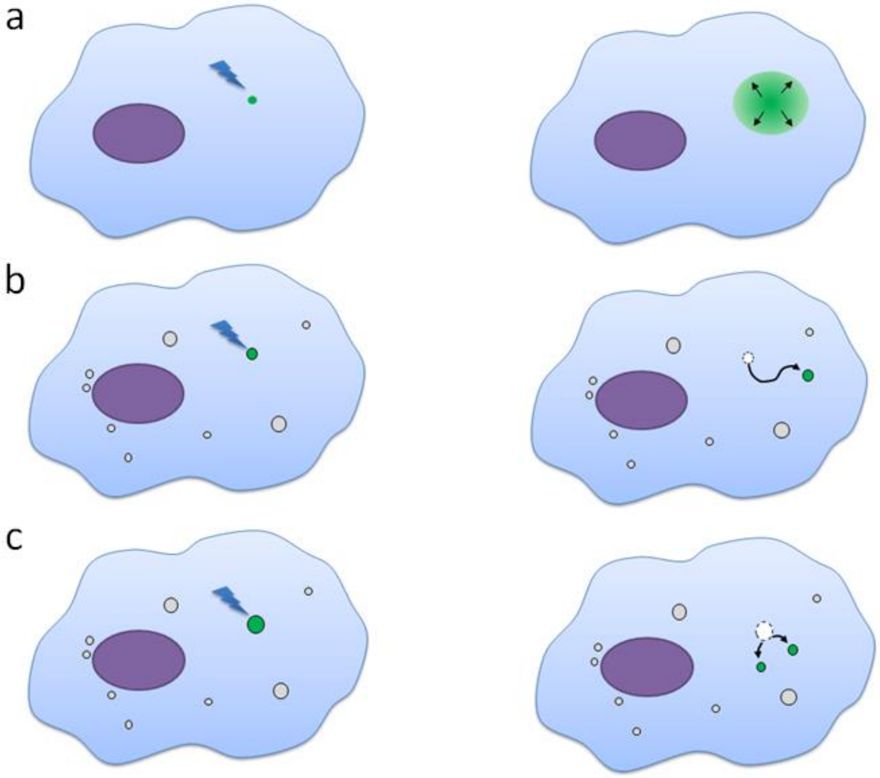

Figure 2.9: Three examples of pulse-chase experiments using PA-FPs. Pulse-chase experiment of protein diffusion (a), vesicle transport (b) and fusion and fission of organelles. Image adopted from reference [87].

3. Methods

3.1 Sample preparation

3.1.1 HeLa cell

HeLa and C2C12 cells were used to investigate membrane damage and repair processes. In general, cells were cultured in Dulbecco’s Modified Eagle’s Medium (DMEM) supplemented with 10% fetal bovine serum (FBS) and antibiotics, including 100 ng/mL streptomycin and 60 µg/mL penicillin (Thermo Fisher Scientific, Carlsbad, CA, USA) at 37 °C and 5% CO_2. Before transfection, cells were seeded into an 8-well Lab-Tek II chambered coverglass (Thermo Fisher Scientific) and incubated for 24 h. Cells were transfected with Lipofectamine 3000 (Thermo Fischer Scientific) according to the manufacturer's protocol. After transfection, cells were incubated for 24 h and washed twice with DMEM containing 10% FBS before imaging. Imaging of cells was always done at 37 °C and with 5% $CO_{2.}$

As to the plasmids, MG53:turboGFP plasmid was originally from OriGene (OriGene, Rockville, MD, USA). Our technician Julia Kuhlmann cloned the turboGFP:MG53, which the turboGFP is N-terminally fused to MG53 by PCR. An linker with the amino acid sequence of GSAGSSAAGSGEF [118] was used to space the turboGFP and MG53. Julia Kuhlmann modified different mutants by site-directed mutagenesis using PCR. mRFP-Rab5 and mRFP-Rab7 were gifts from Ari Helenius (Addgene plasmid # 14436). mRFP-ubiquitin was a gift from Nico Dantuma (Addgene plasmid # 11935).

3.1.2 Live zebrafish

Live zebrafish samples were used in this work to study membrane damage and repair processes. The AB_2O_2 zebrafish wildtype (WT) line from the European Zebrafish Resource Centre (EZRC, Karlsruhe) was used in this work to study membrane damage and repair processes. Zebrafish husbandry and experimental procedures were performed in accordance with German animal protection regulations (Regierungspräsidium Karlsruhe, Germany, AZ35-9185.81/G-137/10). My collaboration partner Dr. Volker Middel injected plasmids to the yolks of 1-2 cell embryos. *Dysf* gene knock-down was also performed by him with 0.8 mM morpholino against Dysf mRNA as described in [25]. The live zebrafish sample was prepared as shown in Figure 3.1. The 3- to 5-days old embryos were first anesthetized with 0.02% ethyl-m-aminobenzoate methanesulphonate (MESAB) and put onto a 1-well Lab-Tek II chambered coverglass (Thermo Fischer Scientific). To immobilize the zebrafish sample, 0.5% low melting agarose was warmed to 60°C and used. After the first agarose layer had cooled down, the zebrafish sample was further fixed with another layer of agarose. The sample was finally covered with a cover glass and was used immediately for imaging.

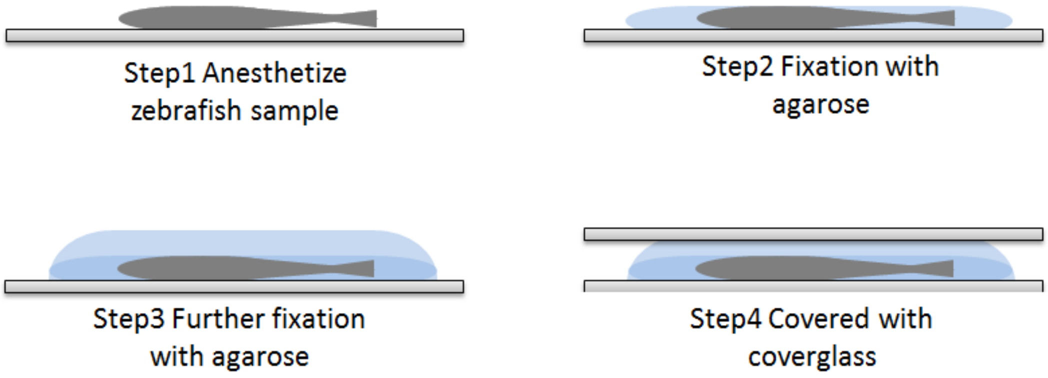

Figure 3.1: Live zebrafish sample preparation as described in the text.

Muscle expression of sensors in zebrafish was driven by the unc45b promotor as described in [119]. Lipid sensors LactC2:GFP, LactC2:RFP were from [120] and pcDNA3-Clover were previously used in [121]. Plasmid of CAAX was originally from [122] and modified by Dr. Volker Middel to CAAX:mEosFP*thermo* as described in [123]. The Dysf plasmids zfWRRFK-TM-C and hWRRFR-TM-C were from this work and all the other mutants of Dysf used in this work were designed and achieved by Dr. Volker Middel by site-directed mutagenesis using PCR [123].

3.1.3 Fungal cells

3.1.3.1 *Aspergilus nidulans*

A. nidulans cells were used in this work for investigating the mechanism of vesicle transport in fungal cells. *A. nidulans* strain TN02A3 was used in this work [124]. Strains with gene deletion of motor protein kinesin-1, kinesin-3 or myosin-5 have been reported in [42, 45, 125], respectively. My collaboration partner Dr. Norio Takeshita transformed the mEosFP*thermo*:ChsB plasmids into different strains, and screened transformants microscopically for fluorescence, which was further confirmed by PCR for correct integration of the constructs [126].

A. nidulans cells were cultured by collaboration partner Dr. Norio Takeshita and Minoas Evangelinos in supplemented minimal medium with 2% of glycerol as the carbon source, and 70 mM sodium nitrate and 0.9 µM ammonium molybdate as the nitrogen source. The expression of mEosFP*thermo*:ChsB under the inducible alcA promoter instead of native ChsB did not show any abnormal phenotype [126]. Before imaging, cells were seeded into 8-well Lab-Tek II chambered coverglass (Thermo Fischer Scientific) and incubated at 28 °C overnight. For the experiments with microtubule or actin destabilizing drugs, benomyl, methyl 1-(butylcarbamoyl)-2-benzimidazole carbamate (Sigma-Aldrich, St. Louis, USA) or cytochalasin A (Sigma-Aldrich) was used at a final concentration of 2 µg/ml in the medium.

3.1.3.2 *Ustilago maydis*

U. maydis cells were used in this work to study the transport mechanism of Num1 protein. *U. maydis* strain AB31 [127] was used. AB31 harbors a set of compatible *bE1* and *bW2* genes under control of the arabinose-responsive Pcrg1 promoter [127]. In glucose containing media, AB31 grows yeast-like, but upon arabinose-induced expression of bE1/bW2, the strain switches to polarized growth and forms long filaments [42, 45].

U. maydis cells were cultered by collabration partner Dr. Theresa Obhof in complete medium (CM) [128] containing 1% glucose (CM-G) or 1% arabinose (CM-A), respectively, at 28 °C. Solid media contained 2% agar. For microscopic analyses, cells were taken from liquid cultures in a CM-G medium. For the investigation of hyphae, cells were transferred from CM-G to CM-A and induced for 6 h, as described [127]. 200 µl cells were mixed with 200 µl 4% low melting agarose (45°C) in 8 well chambers (µ-Slide 8 well, ibidi GmbH, Munich, Germany) and immediately analyzed. *Escherichia coli* strain TOP10 (Thermo Fischer Scientific) was used for cloning purposes. Growth conditions and media for cultivation have been described previously [129].

In this work, the Num1 protein was fused both with mEos2 and tdEosFP for super-resolution imaging by Dr. Theresa Obhof. The mEos2 open reading frame was di-codon optimized for expression in *U. maydis* [130] and fused to the 3´end of the *num1* gene. The construct was integrated into the Num1 locus of strain AB31 [127] by homologous recombination so that the Num1:mEos2 fusion gene was expressed under the native promoter of Num1 in its natural context. A tandem dimeric EosFP (tdEosFP) fusion protein optimized for use in *U. maydis* was also constructed. The T158R mutant of EosFP splits the tetramer into dimeric EosFP [131]. In analogy to mEos2, the tdEosFP open reading frame was fused in frame to the 3´end of the *num1* gene and introduced into the Num1 locus of AB31.

3.2 PALM setup

Our PALM setup is based on an inverted microscope (Axiovert200, Zeiss, Jena, Germany) as shown in Figure 3.2. A high numerical aperture oil immersion objective (Plan-Apochromat, 63x, N.A. 1.46, Zeiss) and a water immersion objective (C-Apochromat, 63x, N.A. 1.2, Zeiss) are applied for different applications. Four lasers with wavelengths 405 nm (Stradus 405-250, Vortran Laser Technology, Sacramento, CA, USA), 473 nm (LuxX 473-100, Omicron-Laserage Laserprodukte, Rodgau-Dudenhofen, Germany), 561 nm (Gem 561, Laser Quantum, Konstanz, Germany) and 639 nm (MRL-FN-639-500, Ultralasers, Ontario, Canada) are combined via dichroic mirrors (AHF, Tübingen, Germany) and passed through an acousto-optical tunable filter (AOTFnC-400.650, A-A, Opto-Electronic, Orsay Cedex, France) to achieve precise control of the laser intensities for illumination. In this work, a beam expander (GBE05-A-5x Achromatic Galilean Beam Expander, AR Coated 400-650 nm, Thorlabs, Dachau/München, Germany) was aligned into the light path to expand the laser beam after the AOTF for imaging large cell structures, e.g., zebrafish myofiber. The expanded laser beam can be focused by the scan lens onto the back focal plane of the objective for wide field illumination. By tilting the mirror in front of the scan lens, the beam can be displaced from the optical axis to change the excitation to total internal reflection (TIRF) mode. For fluorescence recovery after photobleaching (FRAP) experiments, a fraction of the light is split by a polarizing beam splitter cube (PBS). The FRAP lens in the light path and the scan lens form a telescope which generates a parallel incident beam into the objective resulting in the excitation of a spot confined to a diameter of ~1 µm. Two shutters independently control the two excitation light paths. The fluorescence emission is collected by the same objective and passed through a quad band dichroic mirror (z 405/473/561/640, AHF, Tübingen, Germany). The fluorescence is detected either by the EMCCD camera (Ixon Ultra X-7759, Andor, Belfast, UK) or the sCMOS camera (ORCA-Flash4.0, Hamamatsu, Herrsching am Ammersee, Germany) with pixel sizes of 109 nm and 112 nm, respectively. Commercial beam splitting devices (OptoSplit II unit, Cairn Research, Kent, UK) are arranged in front of each camera for two channel imaging. The shutters and the AOTF are controlled by custom written software in LabVIEW (National Instruments, Austin, TX, USA) through a data acquisition card (NI USB-6229 BNC, National Instruments, Austin, TX, USA).

The FRAP light path allows us to perform membrane damage and pulse-chase experiments. For both applications in this work, a portion of the 405 nm laser was split into the FRAP light path and focused on the sample to achieve membrane damage or local photoconversion for the pulse-chase experiment. The details will be discussed in Section 3.3 and Section 3.7.

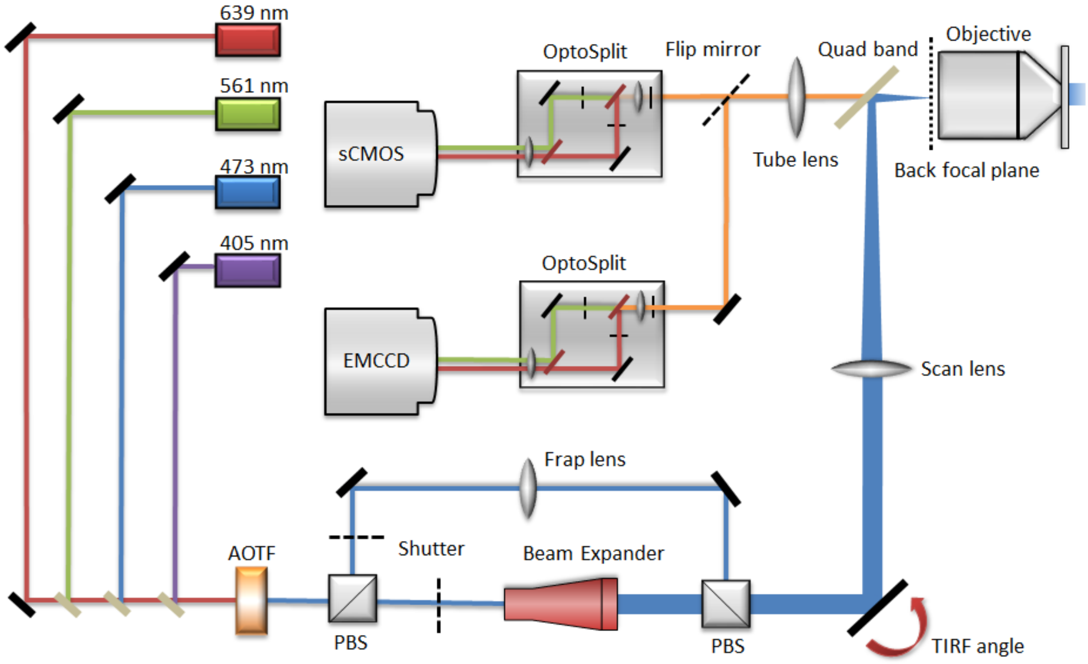

Figure 3.2: Schematic of PALM setup as described in the text.

3.3 Laser-induced membrane damage

To study the process of cell membrane repair, precisely controlled damage of the cell membrane plays a key role. In general, membrane damage can be induced by applying mechanical damage with beads or a needle, by electroporation or by laser irradiation. Among these methods, laser damage is the most convenient way, especially in combination with fluorescence microscopy. Lasers can induce cell membrane damage because of three reasons, including optical breakdown, photothermal damage and photochemical damage, depending on laser powers and exposure times [132]. Femtosecond pulsed Ti:Sapphire lasers have been proven to efficiently cause membrane damage due to two photon absorption by the plasma membrane and the optical breakdown effect [133]. This method is also applied in this work to damage the muscle cells of zebrafish with a Leica TCS SP2 confocal microscope (Leica, Wetzlar, Germany). The detailed procedure was discussed in previous work [25]. However, a controlled method of membrane damage by continuous-wave lasers is beneficial because of their wider availability. In this work, different continuous wave lasers were tested, including 405 nm, 488 nm, 532 nm, 561 nm and 647 nm, both on a commercial spinning disk confocal microscope (Andor Revolution® XD, BFi OPTiLas, München, Germany) and the PALM setup. Among the tested wavelengths, 405 nm laser reproducibly induced localized membrane damage on both thin adherent cells (HeLa cells) and thick tissues (live zebrafish).

To achieve controlled membrane damage on the spinning disk confocal microscope, we employed the FRAPPA unit. The FRAPPA (FRAP+PA) unit is designed for FRAP (Fluorescence Recovery after Photobleaching) experiments and photoactivation (PA) of fluorescent proteins for the study of protein dynamics. To damage the membrane, a region of 6 × 6 pixels was irradiated with a 405 nm laser beam at 200 µW on the sample, with a pixel dwell time of 800 µs. Irradiation was repeated 200-600 times to damage the membrane within 6-18 s locally. The membrane damage method was tested both on cultured HeLa cells and live zebrafish on the spinning disk confocal microscope. HeLa cells and zebrafish muscle cells were labeled with LactadherinC2:RFP (LactC2:RFP) and dysferlin:mOrange (Dysf:mOrange) through transfection and injection of embryos respectively. As shown in Figure 3.3, cultured HeLa cells (Figure 3.3a) and muscle cells of live zebrafish (Figure 3.3b) were damaged upon irradiation with a 405 nm laser. The regions of the damaged membrane showed noticeable morphological changes (Figure 3.3, arrows). These results demonstrate a successful method to study the mechanisms of membrane damage and repair both in cultured cells and thick tissues of live zebrafish.

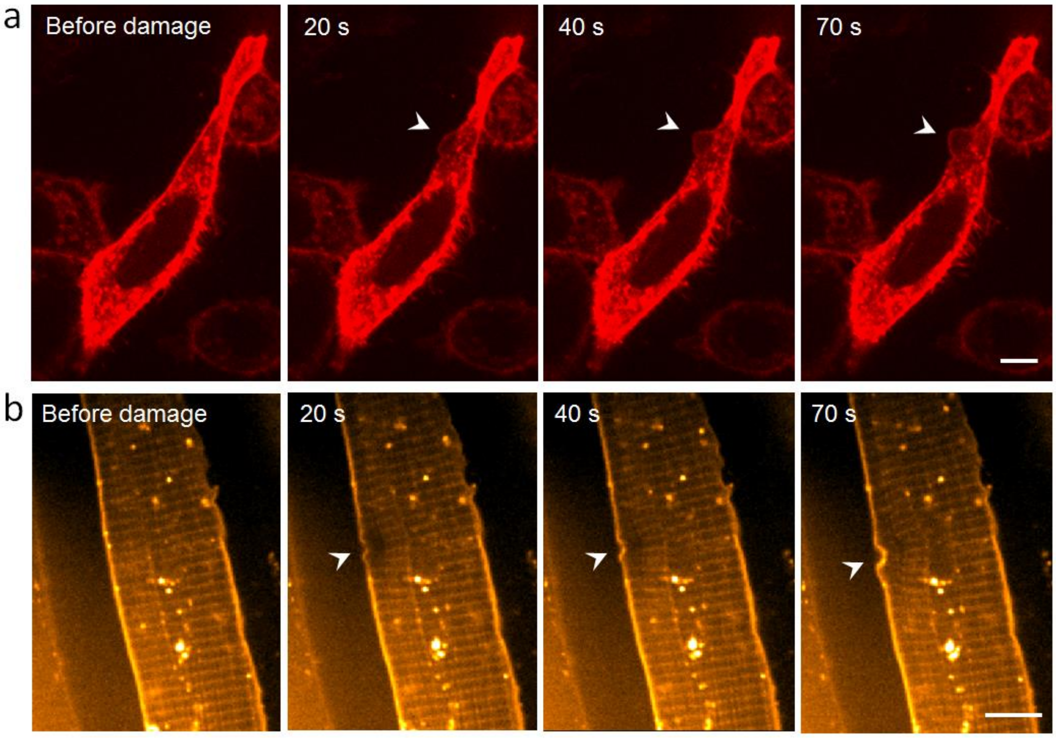

Figure 3.3: Membrane damage was induced by irradiation with a 405 nm laser on the spinning disk confocal microscope. Membrane damage (arrows) was achieved both in the HeLa cell (a) and in the muscle cell of a live zebrafish (b). Scale bar, 10 µm.

The membrane damage method with irradiation by a 405 nm laser was also tested with live zebrafish samples on the PALM setup. The membrane injury was achieved by splitting a portion of the 405 nm laser to the FRAP light path and focusing the laser beam to the sample (5 mW) for 2-4 s. As shown in Figure 3.4, widefield images showed clear membrane damage of the zebrafish muscle cell on the PALM setup.

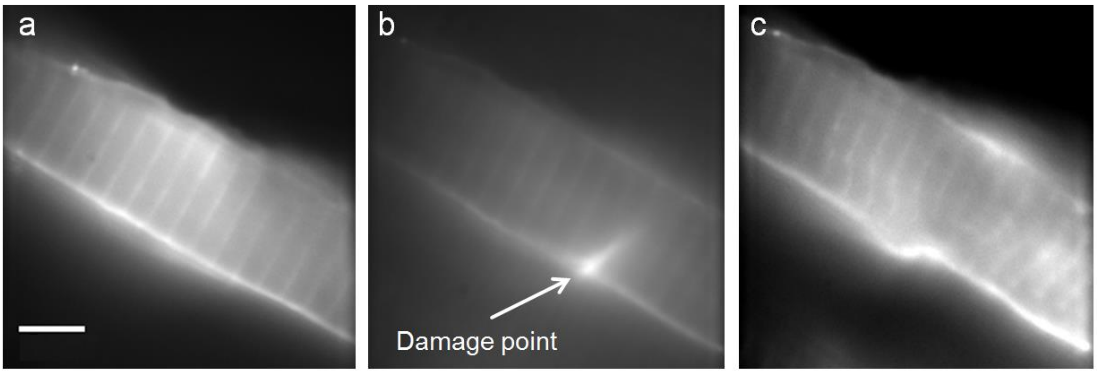

Figure 3.4: Membrane damage was induced in live zebrafish by irradiation with a 405 nm laser on the PALM setup. The muscle cell was imaged before (a), during (b) and 10 s after membrane damage (c), respectively. Scale bar, 5 µm.

Besides detecting membrane damage via cell membrane morphological changes, it can also be assessed by chemical methods, e.g., calcium indicators or indicators of reactive oxygen species (ROS).

Typically, the calcium concentration in tumorigenic cells lines is ~180 nM [134], which is much lower than that in the cell culture medium DMEM (1.8 mM). After membrane damage, the membrane is permeable to ions such as Ca^{2+}. Thus, the cytosolic calcium concentration increases dramatically after membrane damage. By using the calcium indicator fluo-4 AM (Thermo Fisher Scientific), the cell cytosolic calcium concentration can be assessed by the intensity of green fluorescence (Figure 3.5).

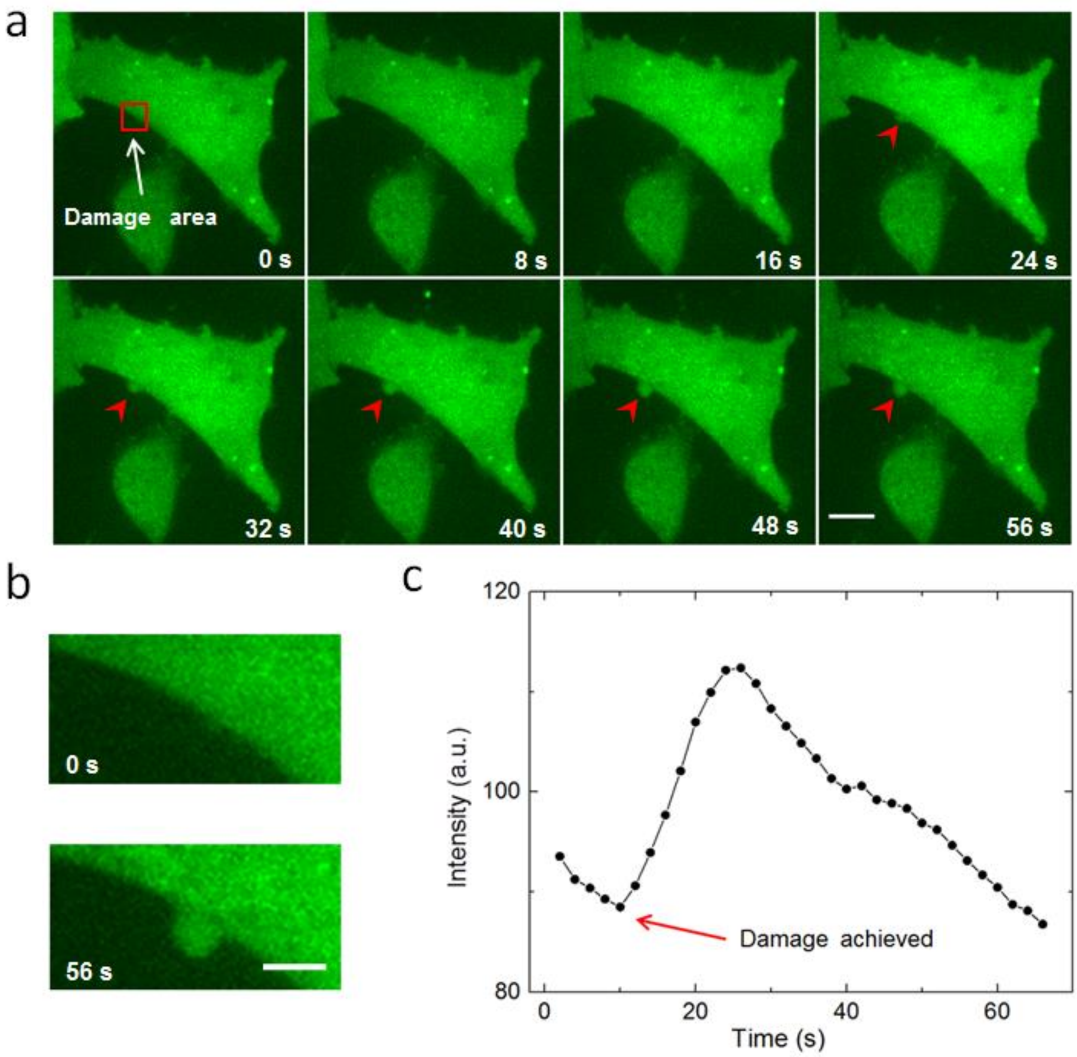

Figure 3.5: Cytosolic calcium concentration increase indicates membrane damage. (a) A HeLa cell was continuously irradiated with a 405 nm laser in a local area (red square) and imaged on the spinning disk confocal microscope. (b) Local membrane region before and after damage. (c) Emission intensity of the calcium indicator. Scale bars, (a) 10 µm, (b) 5 µm.

HeLa cells were first incubated with fluo-4 AM according to the manufacturer's protocol and then imaged on the spinning disk confocal microscope (Figure 3.5). 405-nm laser irridiation was briefly applied (6 × 6 pixels, 500 µs pixel dwell time, 50 repeat times, ~1 s) to a selected area of the membrane (Figure 3.5a, red square) prior to each image of the calcium indicator. As shown in Figure 3.5a and c, 10 s after imaging (5 frames), the fluorescence intensity suddenly increased, and a membrane "bleb" appeared at the damaged area (Figure 3.5b). The intensity increase indicates an increase of the cytosolic calcium concentration, proving membrane damage by 405 nm laser irradiation.

The ROS indicator CellROX Deep Red Reagent (Thermo Fisher Scientific) was also applied to detect the membrane damage. As shown in Figure 3.6, 405 nm laser light was applied to damage the local membrane area (Figure 3.6a, white square) between the 5th and 6th frames.

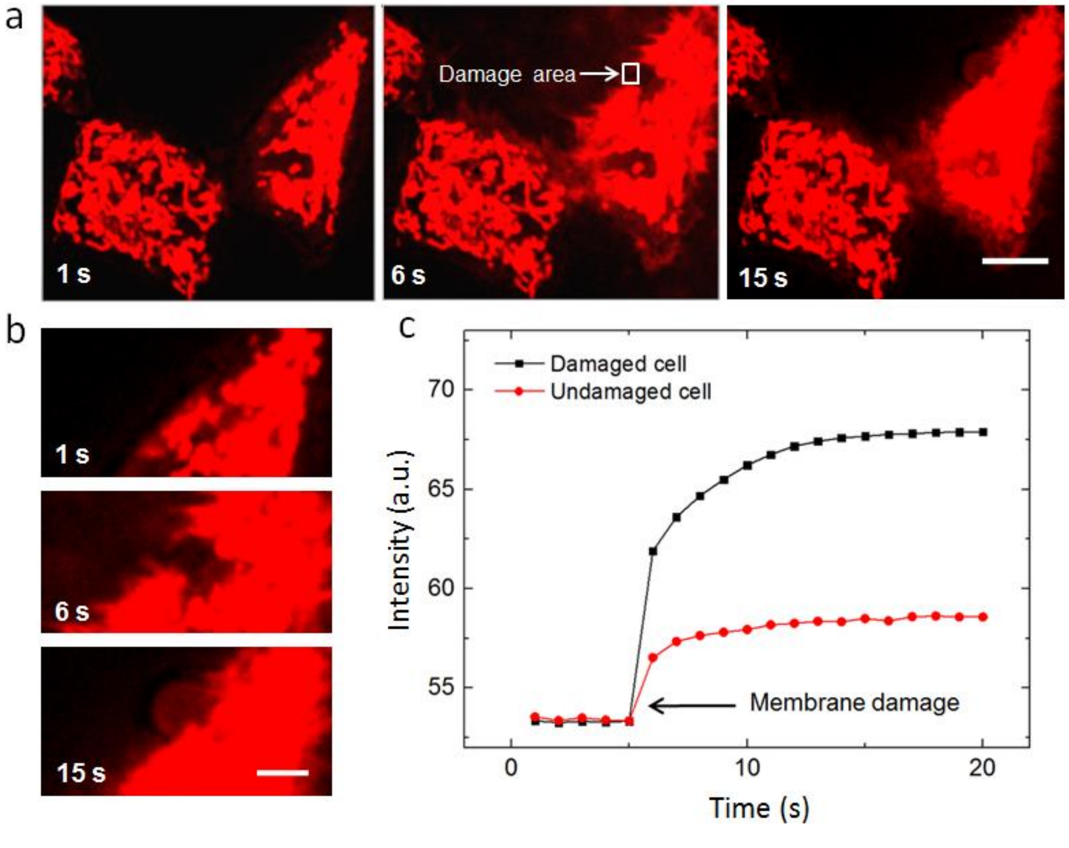

Figure 3.6: ROS concentration increase indicates membrane damage. (a) HeLa cells were labeled with a ROS indicator and imaged on a spinning disk confocal microscope before and after 405 nm laser-induced local membrane damage (white square). (b) Local membrane region before and after membrane damage. (c) Emission intensity of a damaged cell (black curve from the right cell in (a)) and an undamaged cell (red curve from the left cell in (a)). Scale bars, (a) 10 µm, (b) 5 µm.

After membrane damage, the fluorescence intensity of the ROS indicator inside the damaged cell (right cell) showed a steep increase. Intensity profiles of the damaged and undamaged cells in the image are also plotted (Figure 3.6c). 405 nm laser irradiation leads to an increase of ROS concentration in the damaged cell. Therefore, with the ROS indicator, the cell membrane damage induced by the 405 nm laser was confirmed, which also supports the presumed mechanism of laser-induced membrane damage, photochemical damage from ROS, as discussed in Section 1.1.

3.4 PALM imaging of live zebrafish muscle cell

To investigate membrane damage and repair, the PALM technique was employed to visualize muscle cells of live zebrafish. To acquire high-quality PALM images or movies, some factors should be considered, including sample preparation (discussed in Section 3.1.2), sample drift correction, image resolution evaluation, and the process of making super-resolution movies. The latter three factors will be discussed in this section.

3.4.1 Cross-correlation based drift correction

The primary challenge for live zebrafish imaging is the sample drift because of the unstable immobilization and the motion of live zebrafish. Of note, the drift problem is often not noticeable with diffraction-limited resolution. For imaging of zebrafish muscle cell, with 30 ms frame time, a super-resolution image typically takes 1 – 3 min (2000 – 6000 frames). Consequently, the influence of the sample drift needs to be considered. Figure 3.7 shows a super-resolution PALM image of a zebrafish muscle cell without any drift correction. The zebrafish embryo was injected with CAAX:mEosFP*thermo*, a lipid-anchored protein tethered to the cell membrane.

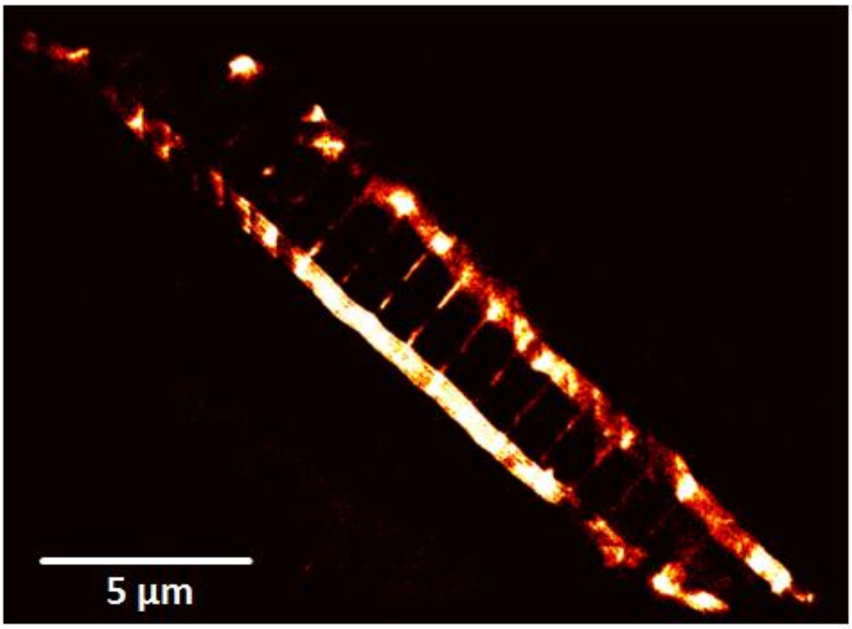

Figure 3.7: Super-resolution PALM image of a zebrafish muscle cell labeled with CAAX:mEosFP*thermo* without any drift correction.

For conventional PALM and STORM imaging of cultured cells or nanostructured surfaces, fiducial markers such as gold nanoparticles or fluorescent beads can be applied to correct the drift of the sample. However, for thick tissues or live zebrafish, the fiducial marker method is not feasible because of the difficulty of marker delivery. To correct the drift during zebrafish imaging, cross-correlation based drift correction can be used. As shown in Figure 3.8a, the matrix *f*(*x*, *y*) is the PALM image of zebrafish muscle cell reconstructed from 100 frames. Then we artificially shifted the structure of muscle cell by 5 pixels (125 nm) and 9 pixels (225 nm) in the horizontal and vertical direction respectively and obtained the matrix *g*(*x*, *y*) (Figure 3.8b). To better illustrate the shift, the two images were also plotted together as shown in Figure 3.8c. The cross-correlation between *f*(*x*, *y*) and *g*(*x*, *y*) can be calculated with the formula

$$f(x,y) \star g(x,y) = \sum_{i=0}^{W-1} \sum_{j=0}^{H-1} f(i,j) g(x+i, y+j), \tag{3.1}$$

where *W* and *H* are the width and height of the two matrices. The calculation will return a matrix with the dimension of (2*W*-1) by (2*H*-1).

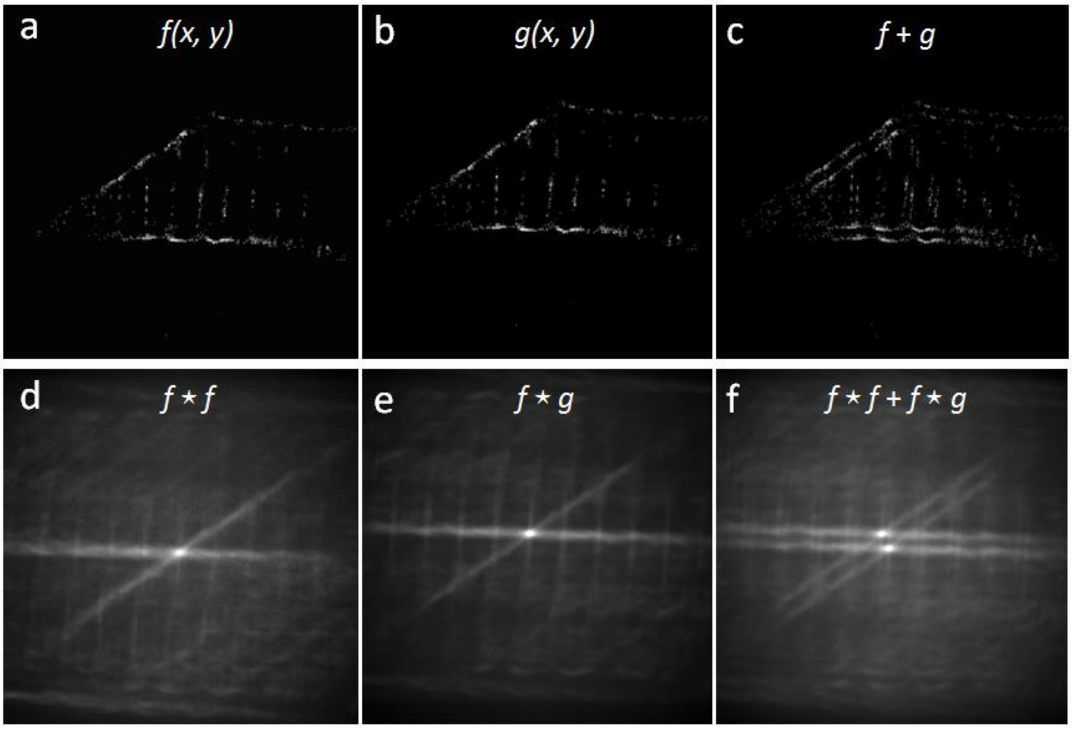

Figure 3.8: Cross-correlation calculation shows the shift between images. (a) PALM image of zebrafish muscle cell *f*(*x*, *y*). (b) Artificially shifted image *g*(*x*, *y*). (c) Overlap of original and shifted images. (d, e) Cross-correlation calculation of *f*(*x*, *y*) with itself (d) and the shifted image *g*(*x*, *y*) (e). (f) The overlap of (d) and (e) shows the shift of the maximum point.

In particular, if the two matrices are identical, the resulting matrix shows a maximum point in the center at the coordinate (*W*, *H*), e.g., $f(x, y) \star f(x, y)$ as shown in Figure 3.8d. Differently, the cross-correlation between the original matrix $f(x, y)$ and the shifted matrix $g(x, y)$ returned a matrix with a shifted maximum point (Figure 3.8e). Figure 3.8f gives a clear illustration by overlapping the Figure 3.8d and e. The shift of the maximum point from the center of the matrix is exactly the artificial shift, which we set for the matrix $g(x, y)$ based on $f(x, y)$ (5 and 9 pixels in each direction). Therefore, by detecting the shift of the maximum point in the cross-correlation matrix from the center point, the shift between two images can be calculated and compensated.

Zebrafish muscle cell is an ideal biological sample to perform cross-correlation based drift correction due to its regular membrane and T-tubule structures. Cross-correlation calculation based on such a structure can effectively and precisely detect the sample drift during the imaging process. In this work, I have combined the image registration algorithm from [135] to our a-livePALM software to achieve fast drift correction for PALM imaging of zebrafish muscle cell. The image registration algorithm is based on a fast Fourier transform to compute the cross-correlation between images with fast computation speed and small memory requirement [135]. The method was tested with data from live zebrafish (Figure 3.9).

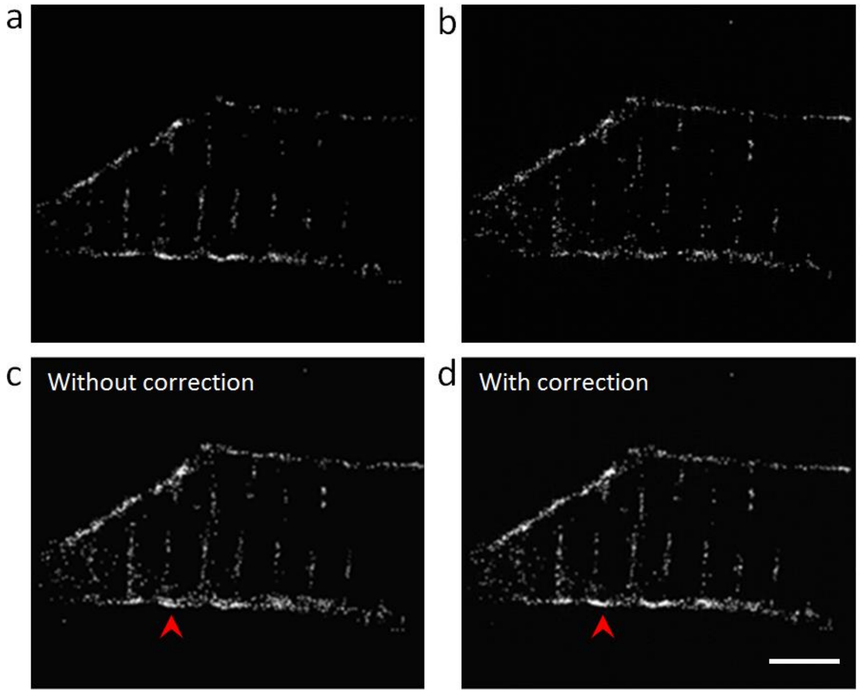

Figure 3.9: Cross-correlation based drift compensation of muscle cell in live zebrafish. PALM images were reconstructed with frames 1 – 100 (a) and frames 2000 – 2100 (b) from a total of 3000 frames. (c, d) Combined images without (c) and with (d) drift correction. Red arrows mark the difference of the membrane structure. Scale bar, 2 µm.

PALM images were reconstructed from two sub-stacks, frames 1 – 100 (Figure 3.9a) and frames 2000 – 2100 (Figure 3.9b) from the raw image stacks. With 30 ms camera exposure time, the time interval between these two sub-stacks was 1 min. From cross-correlation based drift calculation, the drift between these two images turned out to be 125 nm and 50 nm in *x* (horizontal) and *y* (vertical) directions, respectively. These two images were further combined without (Figure 3.9c) and with (Figure 3.9d) drift compensation. The difference of the membrane structure (Figure 3.9c and d, arrows) showed the effect of drift compensation on the combined images.

To compensate the drift of the whole image stack (typically 5000 frames), we used the following strategy (Figure 3.10). The first sub-stack (frames 1 – 100) was selected to reconstruct an image as a reference image. The following sub-stack (frames 101 – 200) was then reconstructed and compared with the reference image. The drift was corrected, and the combined image was used as the new reference image for sequential correction. The procedure was repeated until all images were corrected.

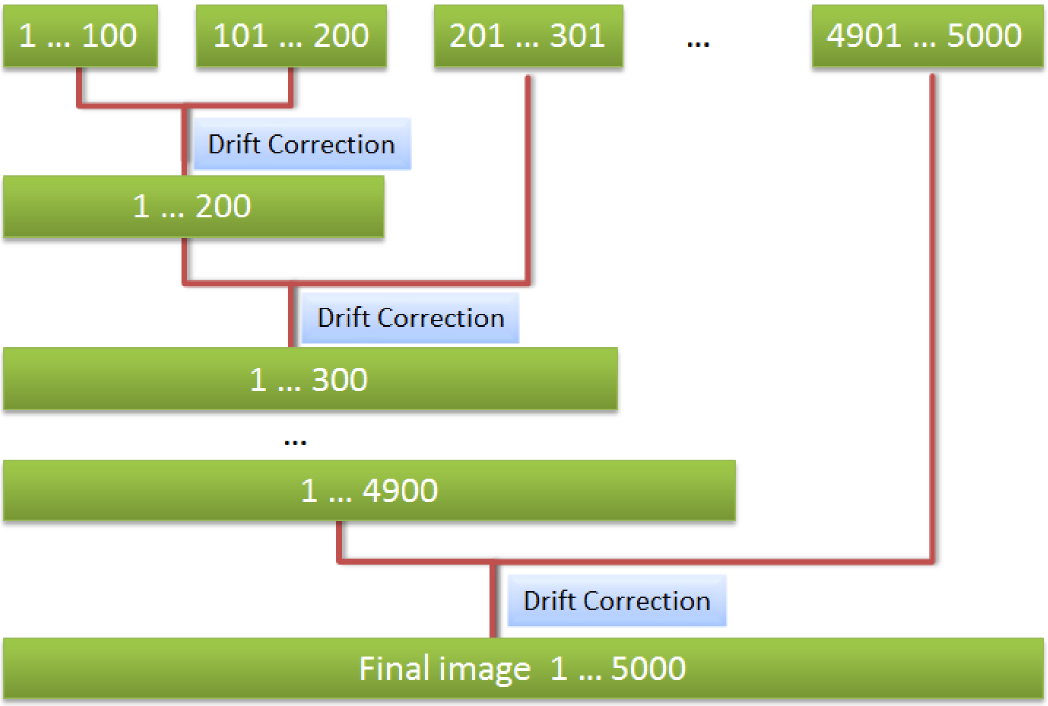

Figure 3.10: Drift correction strategy of the PALM data as described in the text.

With the cross-correlation based drift correction method, PALM images of drifting live zebrafish samples can be efficiently corrected. Figure 3.11 shows the PALM images of the muscle cell in live zebrafish reconstructed from the same raw data without and with drift correction. Raw images were acquired with 30 ms camera exposure time on the PALM setup. PALM images in Figure 3.11 were reconstructed from 5000 frames, and the number of frames per sub-stack was set to be 100. We used the strategy shown in Figure 3.10 to compensate the drift. The improvement after drift correction is obvious, both the membrane and T-tubule structure are better resolved.

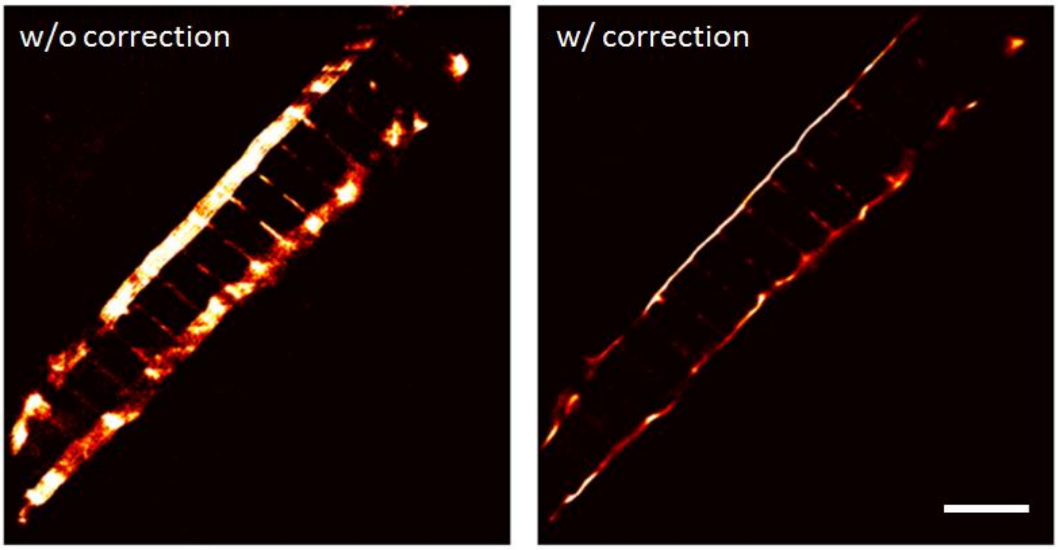

Figure 3.11: PALM images of the muscle cell in live zebrafish without (a) and with (b) cross-correlation based drift correction. PALM images were reconstructed from the same raw data. Scale bar, 2 µm.

In some cases, drift artifacts were not readily detectable by only looking at the PALM images. By comparing the full width half maximum (FWHM) of membrane cross sections, the improvement by the drift correction can be better assessed. As shown in Figure 3.12, the FWHM of membrane intensity profiles along different lines with a linewidth of 8 pixels (200 nm), line 1 and line 2, were calculated from the PALM images of zebrafish muscle cell without and with drift correction. The FWHM was improved from 152.3 nm to 67.6 nm for line 1 and from 150.5 nm to 74.0 nm for line 2, respectively, by applying drift correction.

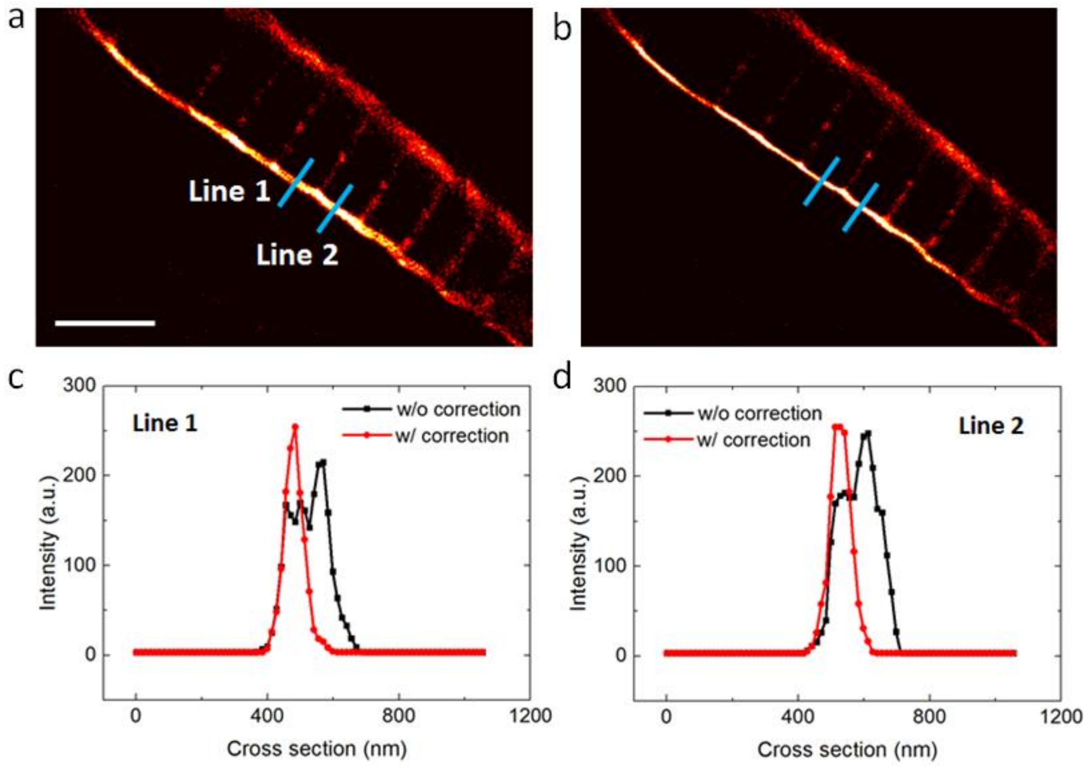

Figure 3.12: PALM images of a live zebrafish muscle cell without (a) and with (b) cross-correlation based drift correction. Both images were reconstructed from the same raw data. (c, d) Intensity profiles along line 1 (c) and line 2 (d) from PALM images of zebrafish muscle cell without (black) and with (red) drift correction. Scale bar, 2 µm.

3.4.2 Resolution evaluation by using Fourier Ring Correlation

The resolution of PALM images needs to be precisely evaluated to determine the optimum parameters for cross-correlation based drift correction. In this work, we employed Fourier Ring Correlation (FRC) and the FRC resolution (R_{FRC}) to evaluate the quality of PALM images [136].

In detail, the raw image stack was first split into two image stacks based on odd and even frame numbers and then reconstructed into two super-resolution images (Figure 3.13a, upper left and upper right). By analyzing the correlation between their Fourier transforms (FT) over the perimeter of circles with different radii in Fourier space (Figure 3.13a, lower left and upper right), an FRC curve was achieved indicating the decay of the correlation towards higher spatial frequency (Figure 3.13b). The image resolution R_{FRC} is the inverse of the spatial frequency at which the FRC curve drops to $1/7 \approx 0.143$, which has been proven as an appropriate threshold value for evaluation of the image resolution (Figure 3.13b) [136]. As shown in Figure 3.13b, the curve reaches the threshold at the spatial frequency of 0.007 nm^{-1}, which is equivalent to a resolution of 142.9 nm.

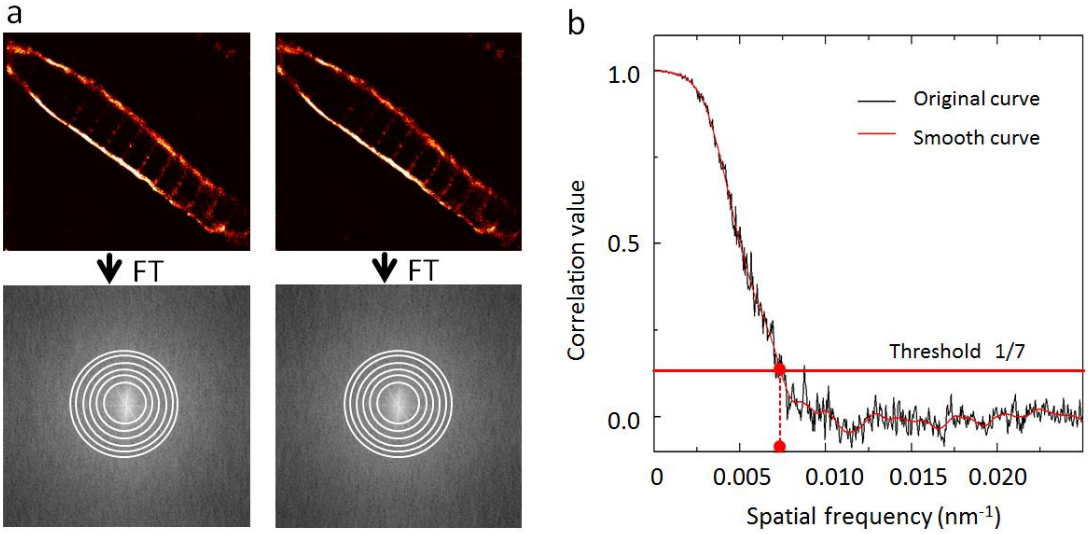

Figure 3.13: Principle of defining image resolution using FRC. (a) Raw images were split into two stacks and reconstructed into PALM images. Both images were transformed to Fourier space and the correlation between circles with different radii was calculated. (b) The correlation curve calculated from (a) with the threshold set to 1/7 for determining image resolution.

With this method, we can precisely evaluate the quality of PALM images without and with drift correction. As shown in Figure 3.14, PALM images of a zebrafish muscle cell were reconstructed from 5000 frames without and with drift corrections. The drift correction was performed with 100 frames as sub-stack. The

R_{FRC} value for the original PALM image was 215.8 nm (Figure 3.14a), which was markedly improved to 135.7 nm after proper drift correction (Figure 3.14b). It is important to note that the R_{FRC} value of the FRC method highly depends on the threshold setting for the correlation curve (1/7 in [136] and this work). In detail, different threshold settings may lead to different relevant spatial frequencies and resolutions for the same correlation curve. However, by fixing the threshold, the FRC method is still a precise and efficient method to compare image qualities before and after some specific image processing technique, such as drift correction used in this work.

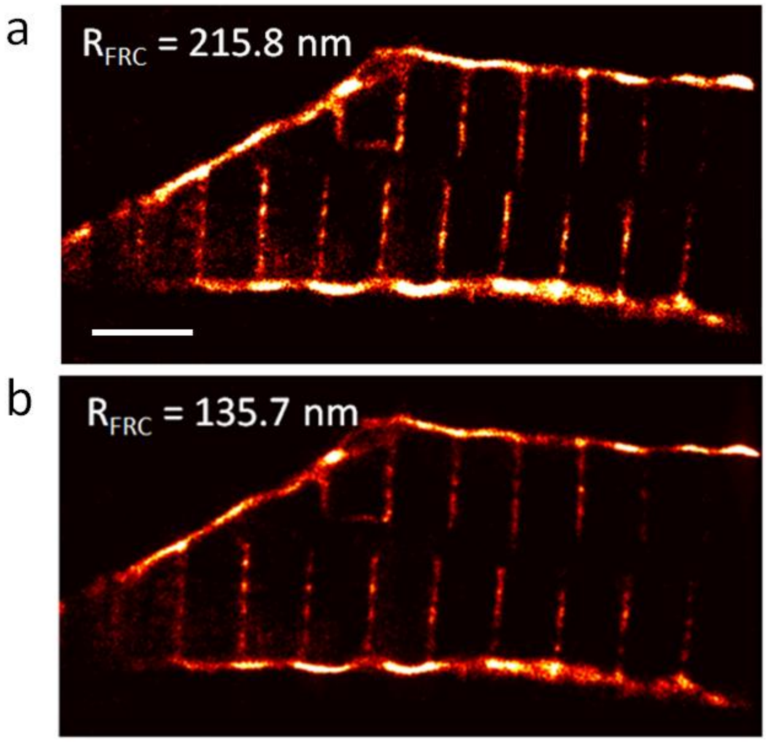

Figure 3.14: PALM images of zebrafish muscle cell without (a) and with (b) drift correction. The FRC resolutions were 215.8 nm and 135.7 nm respectively. Scale bar, 2 µm.

In the drift correction process, the frame number of the sub-stack is a variable which may lead to different PALM image quality. Particularly for samples with different protein expression levels, drift conditions, and imaging conditions, the optimum frame number of sub-stacks must be carefully set to achieve the best image quality. As shown in Figure 3.15, with the same 5000 raw images, the frame number of sub-stacks for drift correction was varied from 0 to 800, respectively. The R_{FRC} values of the final reconstructed images with different sub-stack values were calculated and plotted (Figure 3.15b). The results show that the optimum frame number of the sub-stacks, specifically for this cell, should be set from 100 to 200, resulting in the best drift-corrected PALM image with the lowest R_{FRC} value. Therefore, FRC is an efficient method to evaluate and set the frame number of sub-stacks for precise drift correction.

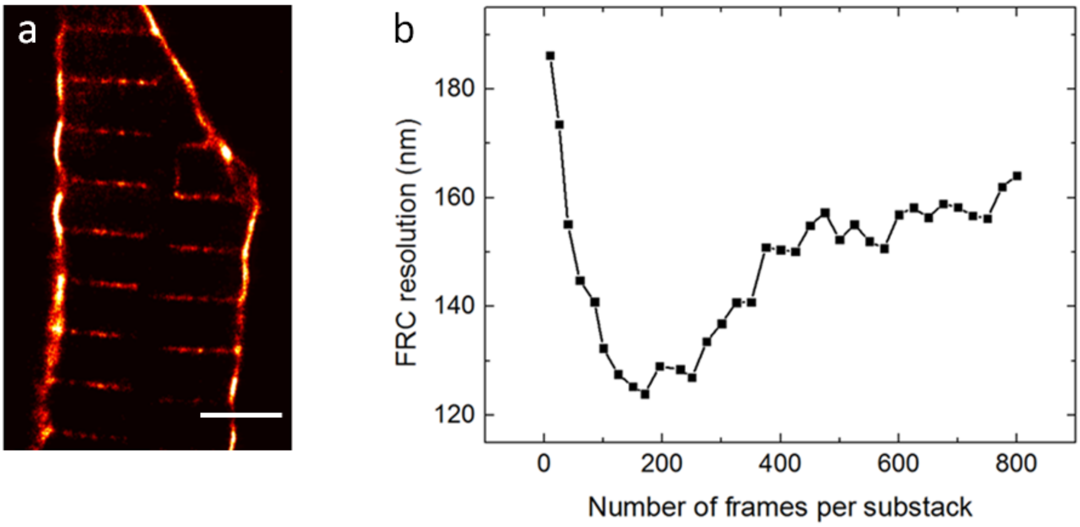

Figure 3.15: Influence of sub-stacks to the quality of PALM images. (a) PALM image of a zebrafish muscle cell with drift correction. The frame number of sub-stacks was set to 100. (b) FRC resolutions of PALM images with different frame numbers of sub-stacks for drift correction. Scale bar, 2 µm.

Moreover, FRC is also a suitable method to evaluate redundant frames for PALM sampling. As shown in Figure 3.16, the R_{FRC} values were calculated for PALM images reconstructed and drift corrected (100 frames per sub-stack) from a different total number of frames. The result in Figure 3.16b shows that roughly 2000 frames were already sufficient to reconstruct the zebrafish muscle cell structure (Figure 3.16a). With more raw frames, the resolution of the reconstructed image will not improve further. This indicates that the raw images after sufficient collection of fluorescence events are redundant for reconstruction of the super-resolution PALM image.

By combining FRC and cross-correlation based drift correction methods for PALM imaging of zebrafish muscle cells, the quality of PALM images can be precisely evaluated to achieve the optimum parameters for drift correction. Therefore, the sample drift problem can be significantly reduced. This technique can be generally applied to imaging of live cells, in particular for imaging structures such as microtubules and actin cytoskeletons.

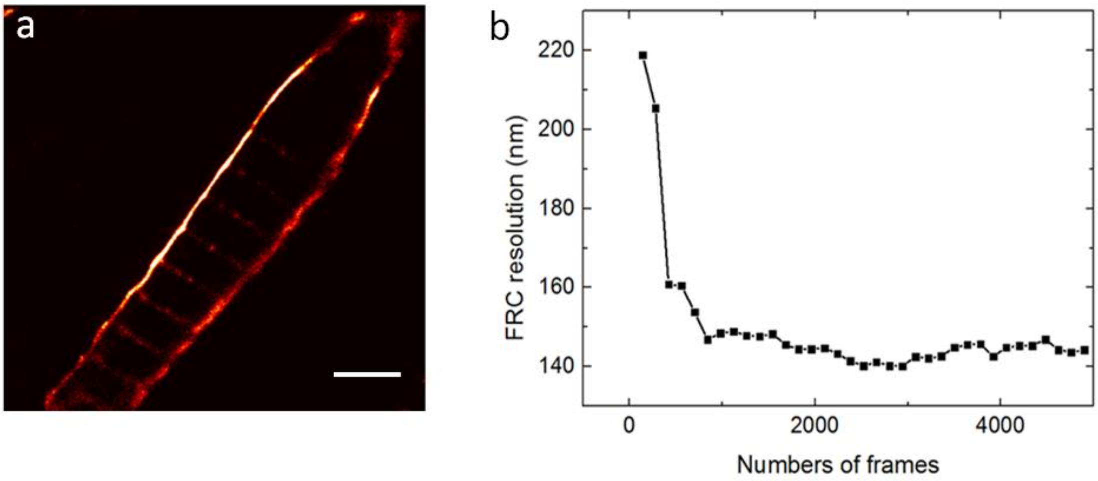

Figure 3.16: Redundant frames evaluated by FRC for PALM images. (a) PALM image of zebrafish muscle cell reconstructed from 2000 frames. (b) FRC resolutions of PALM images reconstructed from different numbers of frames. Raw images were all collected on the zebrafish muscle cell shown in (a). Scale bar, 2 µm.

3.4.3 Super-resolution movie of damaged muscle cell

Zebrafish muscle cells have efficient self-repair ability after membrane damage. To visualize the membrane repair process, raw images need to be converted into PALM movies for visualizing of the morphological change of the damaged membrane. To generate movies, image sequences were collected in the following way. A 405 nm laser was focused on the zebrafish muscle cell for 2 – 4 s to achieve membrane damage as described in Section 3.3. After membrane damage, intense 561 nm laser irradiation (800 – 1200 W/cm^2) was applied to bleach the activated mEosFP*thermo* fluorophores in the red channel for about 1 min. This time is also necessary for the damaged fiber to stabilize again for the following imaging process. Generally, 5000 frames were acquired with 30 ms camera exposure time for further analyses. To obtain PALM movies, we employed the "moving-window binning" analysis [137]. Typically, 300 – 500 frames (9 – 15 s) from the beginning of the raw image stack were set to be the "window" for reconstructing the first PALM image. The "window" was subsequently shifted by 30-50 frames (0.9 – 1.5 s) to reconstruct the next PALM image until the "window" was shifted to the end of the whole image stack. Parameters, such as the "window" size and the shifted frames, have to be set carefully based on the sample conditions and the quality of the raw images. A larger "window" size may improve the PALM image quality but reduce the time resolution. Therefore, the spatial and temporal resolutions need to be balanced according to different observation requirements. Figure 3.17 shows a zebrafish muscle cell labeled with CAAX:mEosFP*thermo* and imaged after membrane damage. 5000 frames were collected and processed with a “window” size of 330 frames (~10 s) and 33 shifted frames (~1 s) to make the PALM movie. The morphological change at the damaged membrane region is clearly visible.

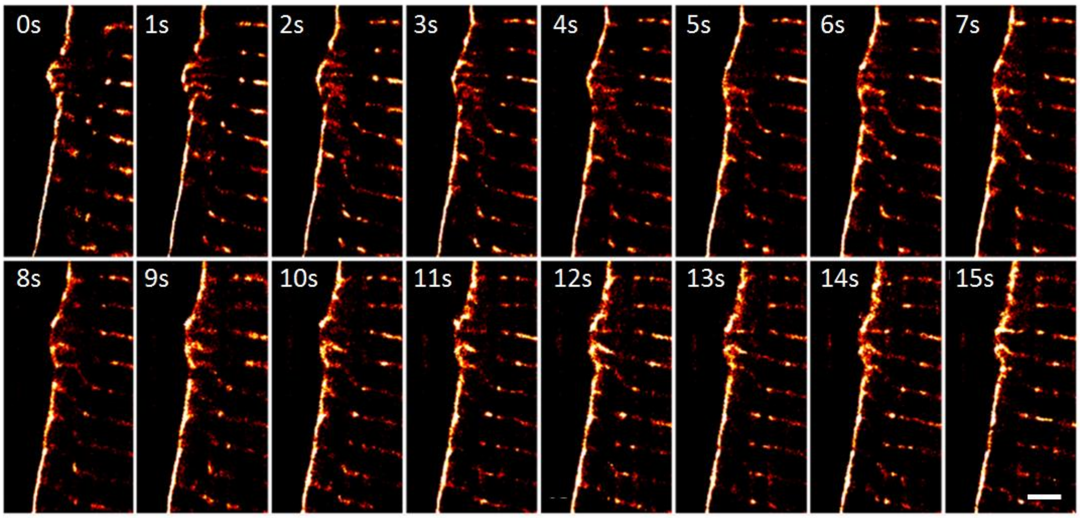

Figure 3.17: PALM image sequence of damaged muscle cell from live zebrafish. Scale bar, 2 μm.

3.5 Directional analysis of single molecule trajectories

In addition to super-resolution imaging, the PALM technique has also been widely used for studies of molecular dynamics, e.g., sptPALM and smDIMSA, as discussed in Section 2.5.1. These studies mainly focus on diffusion coefficient calculation from the abundant trajectories. For research of muscle cell repair process, however, the directional motion of functional proteins is particularly important for investigating the mechanism of protein accumulation. For example, Dysf accumulates fast at the membrane damage site, but the mechanisms of transport, such as the source of the accumulated Dysf, are still elusive. Therefore, we have implemented a trajectory analysis method focused on directional motion of proteins aiming to observe the protein recruitment process at the single molecule level.

All the trajectories after membrane damage were collected as discussed in Section 2.5.1. Dysf is a trans-membrane protein, which distributes predominantly on the cell membrane. Thus, analysis of a preferred direction of the collected trajectories was focused on the membrane region next to the damaged site (Figure 3.18a). For the quantitative calculation, we defined a value R_{proj} based on the collected trajectories in the adjacent membrane region. In detail, for each trajectory, its projection onto a line connecting the midpoint of the trajectory with the lesion site was calculated (Figure 3.18b). The resulting displacement (Figure 3.18b, red line) was divided by the number of steps in the trajectory, yielding positive (S_{pos}) or negative (S_{neg}) speeds, which represent the motion of the single trajectory towards or away from the lesion, respectively. The R_{proj} parameter was defined as the ratio of the summed magnitudes of all positive and negative speeds from one measurement with the formula

$$R_{proj.} = \frac{\sum S_{pos}}{\sum S_{neg}} \,. \tag{3.2}$$

Therefore, for random trajectories, the R_{proj} value should be close to one. R_{proj} values significantly greater or smaller than one indicate a net movement of the measured molecules toward or away from the lesion respectively. With this analysis, directional motion of membrane proteins can be clearly revealed, especially in the membrane repair process. The application of this method in zebrafish will be further discussed in Section 4.3.

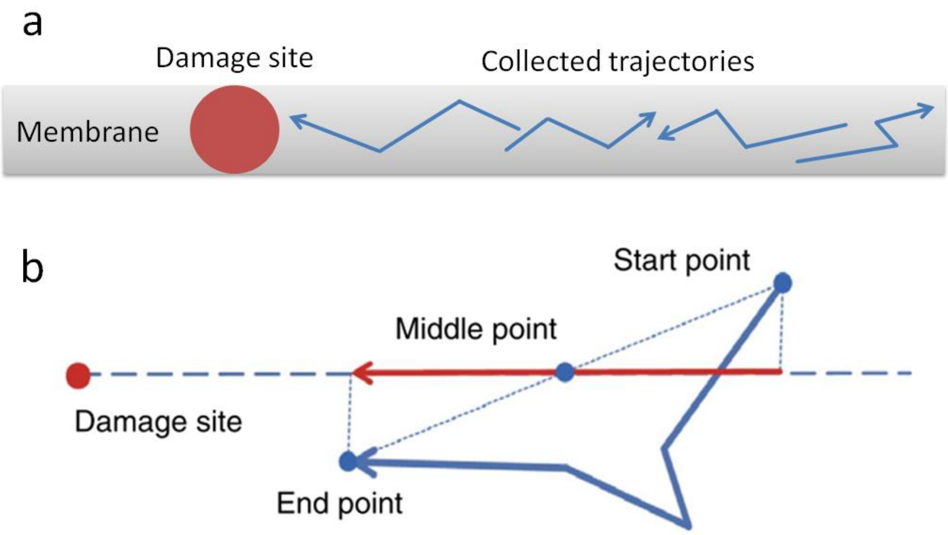

Figure 3.18: Directional analysis of membrane protein movements during membrane repair. (a) Trajectories in the area next to the damaged membrane were collected. (b) Projection analysis of each single trajectory for further calculation of the R_{proj} value.

3.6 Localization-based cluster analysis

Localization of individual molecules in PALM imaging also allows us to identify and analyze the protein clusters. The matrix in Figure 3.19a represents the spatial distribution of collected fluorescence events. Each element in the matrix refers to a single pixel in the PALM image, and the numbers represent how many fluorescence events were recorded in each pixel. All the numbers were set to 1 for simplicity (Figure 3.19a, left).

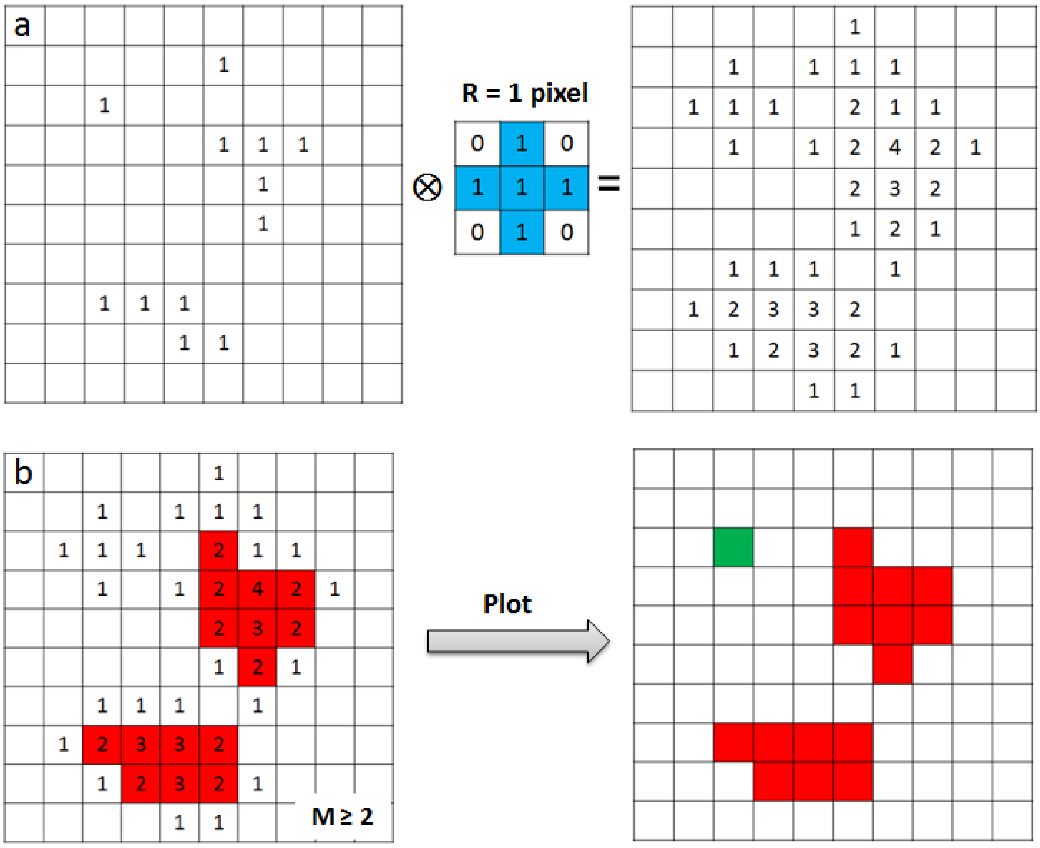

Figure 3.19: Localization-based cluster analysis as described in the text. (a) Convolution of localization matrix with mask matrix. (b) Selection and rendering of clusters.

Two parameters need to be carefully set to define clusters, the radius of the searching range, *R*, and the minimum molecule number, *M*. In detail, if the molecule number in the defined circular area with radius *R* is equal or larger than *M*, the center pixel in the region is defined to be part of the cluster. The cluster searching process is a convolution calculation with a proper mask which was generated based on the defined parameter *R*. As shown in Figure 3.20, an approximately circular region with the radius of *R* in the matrix was selected and the elements in the region were set to 1.

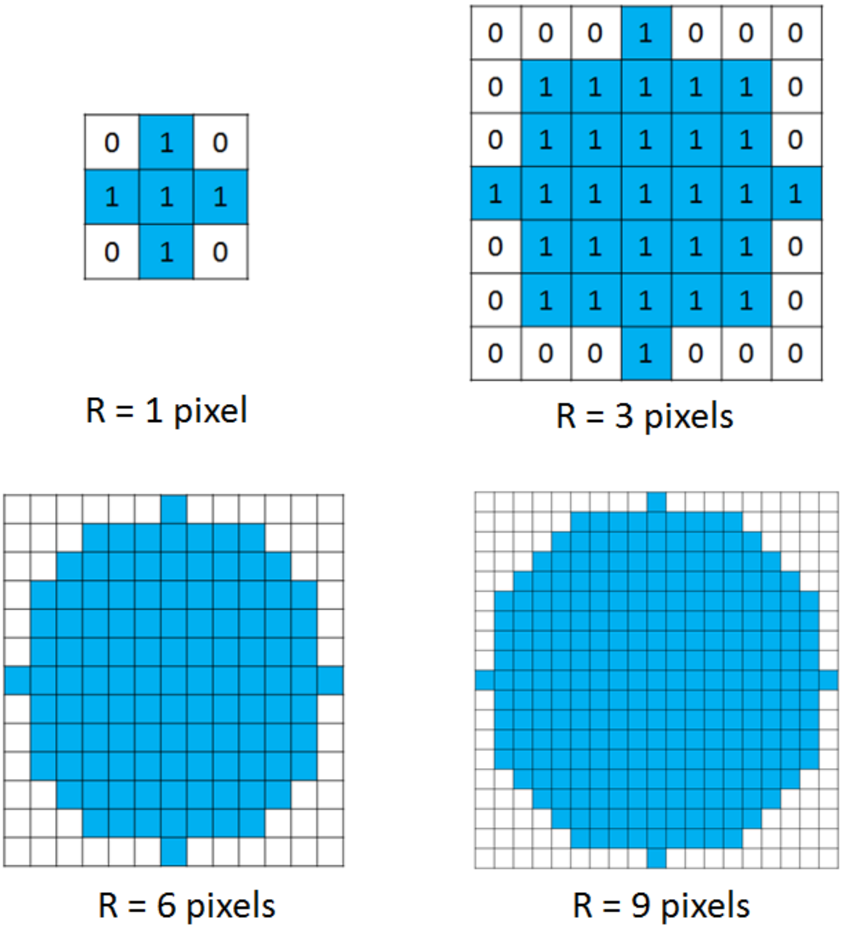

0	1	0
1	1	1
0	1	0

R = 1 pixel

0	0	0	1	0	0	0
0	1	1	1	1	1	0
0	1	1	1	1	1	0
1	1	1	1	1	1	1
0	1	1	1	1	1	0
0	1	1	1	1	1	0
0	0	0	1	0	0	0

R = 3 pixels

R = 6 pixels

R = 9 pixels

Figure 3.20: Setting of the convolution mask with different radii. The elements in blue and white color regions were set to 1 and 0, respectively.

To better illustrate the convolution process, an example was given with the convolution mask (*R*=1) and an original matrix (Figure 3.19a). The convolution result was shown in Figure 3.19a (right). Based on the convolution result, we set the minimum molecule number (*M*=2 in Figure 3.19b), so that the pixels belonging to clusters can be specifically selected and rendered with red color. The fluorescence events not related to clusters are presented with green color (Figure 3.19b). By setting proper parameters for different applications and imaging conditions, the cluster area can be clearly defined and visualized for further analyses.

After defining the cluster area, individual clusters need to be separated for statistical analyses of cluster properties, such as cluster size and molecule number per single cluster. In principle, there are two criteria to define individual clusters based on the relations between neighboring pixels. (1) Neighbors sharing a common corner belong to the same cluster. (2) Neighbors must share a common side to be recognized as being from the same cluster. In this work, to determine individual clusters, we employed the second criterion using the Hoshen-Kopelman algorithm included in Matlab software [138]. As shown in Figure 3.21, for example, the defined cluster area (red area) was split into two clusters (blue and yellow clusters) with the Hoshen-Kopelman algorithm.

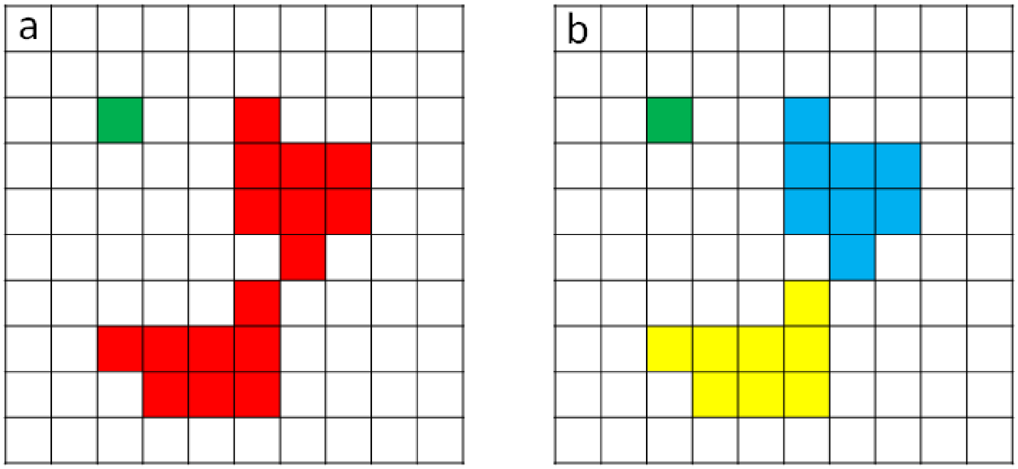

Figure 3.21: Definition of individual clusters. (a) Cluster area (red) and unrelated events (green). (b) Based on the ‘common side’ rule described in the text, cluster area was separated into two clusters, blue and yellow clusters.

Localization-based cluster analysis can be combined with the moving-window binning technique. Therefore, the dynamics of clusters, such as clusters fusion and fission processes, can also be clearly detected. The application of this method in *A. nidulans* will be discussed in detail in Section 5.1.

3.7 Pulse-chase imaging of vesicle transport and kymograph analysis

To investigate the mechanism of vesicle transport in *A. nidulans*, we employed the pulse-chase experiment and kymograph analysis. Unlike diffusive and directional motion, discussed in Section 2.5.1 and Section 3.5, the motion of vesicles in the cell cytosol is active transport based on motor proteins (see Section 1.2). Therefore, by quantitatively analyzing the vesicles' active transport, one may find constant speeds, which reflect the motion of vesicles propelled by different motor proteins.

As discussed in Section 2.5.2, by using photoconvertible FPs for pulse-chase imaging, the optical contrast can be dramatically increased compared with labeling with standard FPs. As shown schematically in Figure 3.22a, upon excitation, all vesicles labeled with normal FPs show fluorescence emission. Thus, signals from single vesicles, especially small and fast-moving vesicles, cannot be distinguished easily. However, with labeling via photoconvertible FPs, the cells can be locally irradiated to locally photoconvert the FPs, and transport of vesicles can be easily detected with minimum influence of the background (Figure 3.22b). This technique allowed us to tag a small subset of molecules at an arbitrary location in the cell and trace their movement with exceptionally low background fluorescence. Therefore, it is a powerful tool for the quantitative study of vesicle transport. To this end, the photoconvertible protein mEosFP*thermo* was fused to ChsB to visualize the transport of ChsB containing vesicles.

For pulse-chase experiments, the whole cell was first pre-bleached by intense 561 nm laser irradiation (0.8 – 1 W/cm²). After that, a 405 nm laser was tightly focused into the sample through the FRAP light path of the PALM setup (See Section 3.2) to locally convert a small number of mEosFP*thermo*:ChsB molecules (b). The local conversion area was either at the cell tip or in the body region ~5 µm away from the tip of the cell. After local photoconversion for 1 s, the 561 nm laser was switched on again (200 – 400 W/cm²) to excite photoconverted mEosFP*thermo*:ChsB molecules in the red channel. Image stacks from the pulse-chase experiment were further processed into kymographs to analyze the speed of vesicle transport statistically (Figure 3.22c). Kymographs were generated with the ImageJ software along a straight line tracing the long axis of the cell, and the line width was set equal to the width of the cell to cover the whole cell region. The intensity along the defined line for the entire image stack can be visualized as a kymograph. Transport of vesicles is seen as lines in the kymograph (Figure 3.22c). It should be noted that fungal cells are the ideal system for the kymograph analysis of vesicle transport. Due to the polar growth of the fungal cells, the vesicle transport in the linear-shaped cells can be seen as one-directional motion. Therefore, the speed information of vesicles can be easily calculated by measuring the slopes of the lines in the kymographs. By combining pulse-chase imaging and kymograph analysis, the vesicle transport in *A. nidulans* was clearly visualized. The details will be discussed in Section 5.1.2.

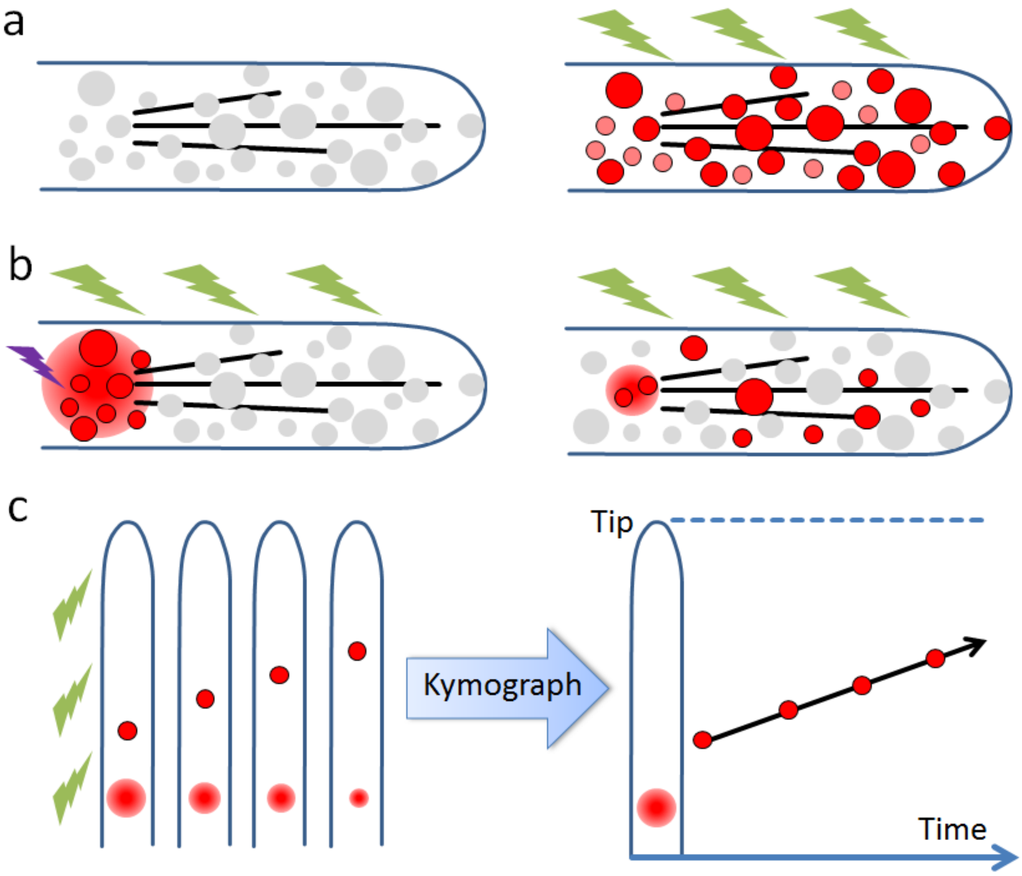

Figure 3.22: Imaging of vesicles labeled with standard FPs (a) and pulse-chase imaging of vesicles labeled with photoconvertible FPs (b). (c) Kymograph analysis of vesicle transport based on the image stack from the pulse-chase experiment.

4. Investigation of dysferlin and MG53 in membrane repair

Skeletal muscle cells are prone to plasma membrane lesions under physiological levels of mechanical stress. To prevent cell death and to avoid unnecessary cycles of muscle regeneration with concomitant depletion of stem cell pools, lesions are rapidly sealed by a repair patch consisting of proteins and lipids [139, 140]. Dysf and MG53 are two essential proteins in the membrane repair process which restores cell integrity [11, 12, 141]. In this chapter, we explain the roles of positively-charged motifs in Dysf and MG53, respectively. Focusing on Dysf, we further investigated the interaction of the positively-charged motif with a membrane phospholipid, phosphatidylserine (PS), and discuss the mechanism of Dysf and PS accumulation in the membrane repair process.

4.1 Positively-charged motifs in MG53 and dysferlin

4.1.1 The role of a positively-charged motif in dysferlin

Dysf is known as a key functional protein for earlier membrane repair, which rapidly recruits to the membrane injury. Investigation showed that it is not the full-length Dysf, but a 72 kDa C-terminal fragment (mini-dysferlin$_{C72}$), which accumulates at the damaged membrane (Figure 4.1a) [24]. Moreover, a shorter C-terminal fragment of Dysf with only 74 amino acids (AAs) including the TM-domain was still sufficient to translocate towards the lesion and accumulate (Figure 4.1a, 74 AA dysferlin) [25]. To further study the mechanism of Dysf accumulation, my collaboration partner Dr. Volker Middel shortened zebrafish Dysf to a C-terminal fragment including the TM-domain with only 48 AAs (zfWRRFK-TM-C) (Figure 4.1a).

Together with Dr. Volker Middel, we injected zebrafish embryos with zfWRRFK-TM-C:Clover and muscle cells of live zebrafish were imaged with a Leica SP2 confocal microscope. As shown in Figure 4.1b and c, the zfWRRFK-TM-C fragment localized correctly on the sarcolemma and the Z-lines. After membrane damage, we observed the active recruitment of the zfWRRFK-TM-C fragment to the lesion. Apparently, the short C-terminal fragment of Dysf, zfWRRFK-TM-C, still functioned correctly during the membrane repair process. Therefore, we further shortened the Dysf fragment by cutting off the five-AA motif WRRFK (Figure 4.1a). Surprisingly, without the five-AA motif WRRFK, the zfTM-C fragment completely lost its membrane targeting ability. Instead, it showed a purely cytosolic distribution (Figure 4.1b). Moreover, accumulation after membrane damage was also abolished (Figure 4.1b, c). Similarly, we also shortened the zfWRRFK-TM-C fragment from the C-terminus to zfWRRFK-TM (Figure 4.1a). However, the accumulation in the repair patch was not influenced by deletion of 14 AAs (KMVGPFSGLGKGTQ) C-terminally (Figure 4.1c). All these fragments were fused with the green fluorescent protein, Clover, in the C-terminus. Taken together, the C-terminal short fragment of zebrafish Dysf, zfWRRFK-TM-C, showed membrane targeting and rapid accumulation at the lesion after membrane damage, similar to full-length Dysf. We conclude that this performance strongly depends on the five-AA motif WRRFK.

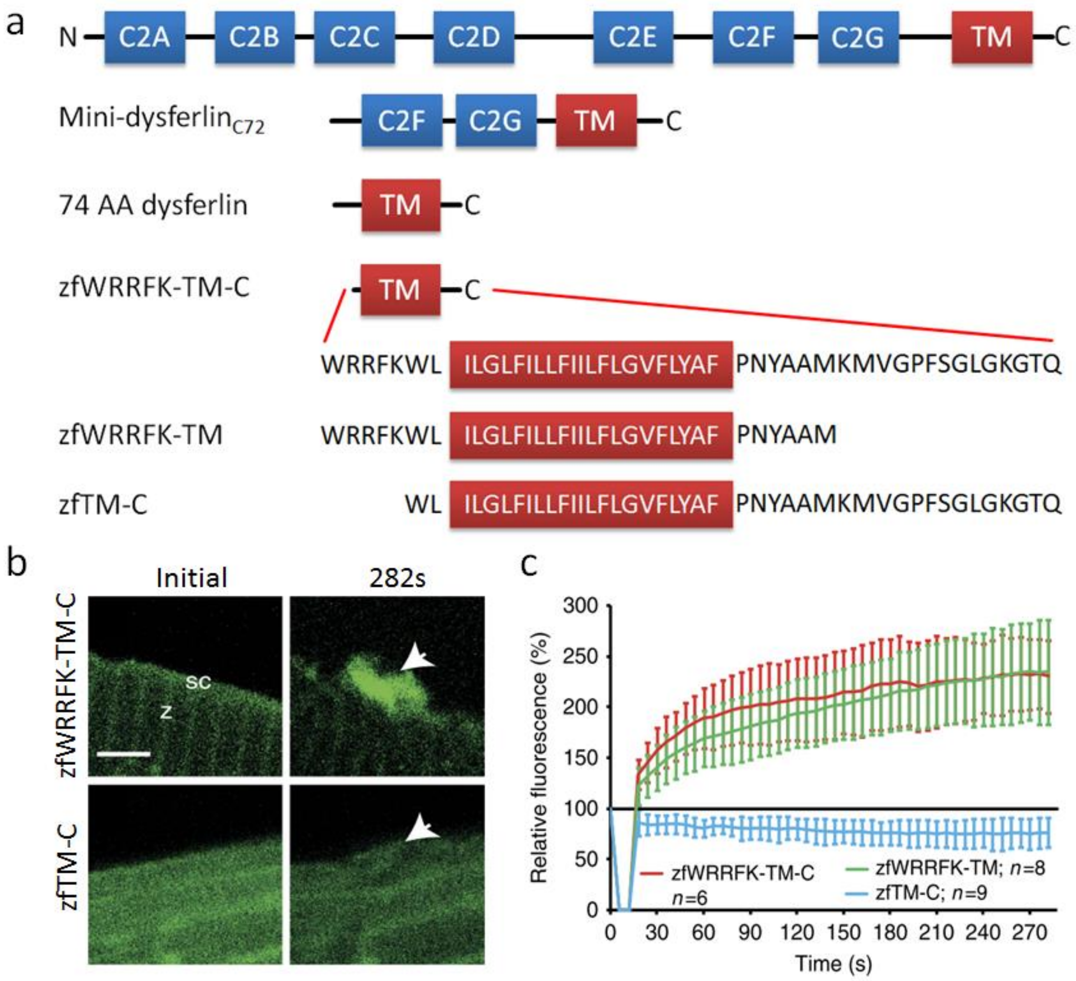

Figure 4.1: Sequences and accumulation properties of zebrafish Dysf fragments. (a) The domain structure and different fragments of zebrafish Dysf. (b) zfWRRFK-TM-C accumulated in the repair patch, but no accumulation showed for zfTM-C. (c) Accumulation kinetics of zfWRRFK-TM-C (red), zfWRRFK-TM (green) and zfTM-C (blue). The data are given as mean ± SD and scaled such that 100% corresponds to fluorescence from the same area before damaging. Scale bar, 4 µm. Image adopted from reference [123].

Among twenty standard AAs, the side chain of arginine (R) and lysine (K) are positively charged. Therefore, WRRFK is a strongly positively charged motif. Considering that the RR was proven to be involved in the protein-membrane interaction [142], the RR in the WRRFK-motif could also perform a crucial role in the short fraction of zebrafish Dysf, zf-WRRMF-TM-C, to direct the accumulation after the membrane injury. Therefore, we mutated either one or both arginines of the motif and tested the mutants in the zebrafish. All the mutants were C-terminally fused to Clover for imaging, and accumulation after the membrane damage was quantified as shown in Figure 4.2a. Translocation of Dysf to the lesion was significantly reduced, indicating that both arginines contribute to Dysf accumulation.

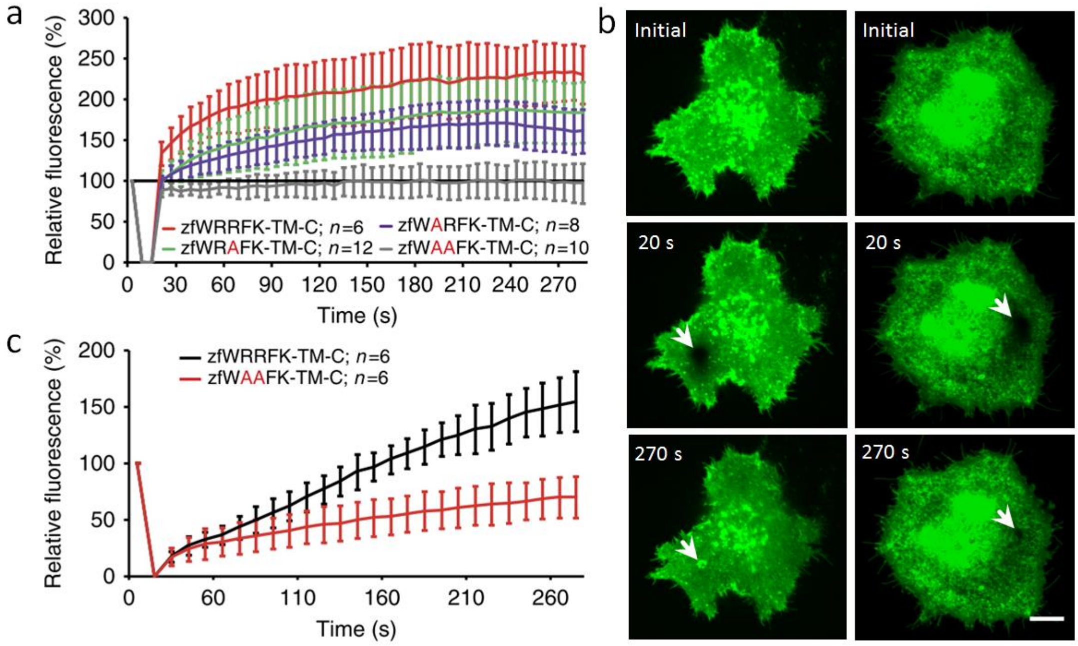

Figure 4.2: The WRRFK-motif is essential for Dysf accumulation. (a) Fluorescence intensities of Dysf mutants at the lesion after membrane damage in the live zebrafish. zfWRRFK-TM-C (red) but not zfWAAFK-TM-C (gray) accumulated rapidly at the lesion. The effect was reduced with the exchange of the first (zfWARFK-TM-C; purple) or second arginine by alanine (zfWRAFK-TM-C; green). (b) In HeLa cells, zfWRRFK-TM-C markedly accumulated at the lesion 270 s after membrane damage (left), whereas zfWAAFK-TM-C showed only fluorescence recovery after photobleaching (right). (c) Fluorescence intensities at the damaged region of zfWRRFK-TM-C and zfWAAFK-TM-C in HeLa cells. Scale bar, 10 µm. Image adopted from reference [123].

To test zfWRRFK-TM-C accumulation in a heterologous system, we also performed the membrane damage experiment in HeLa cells expressing a very low level of endogenous Dysf [143]. We employed a spinning disk confocal microscope to image the damaged cell with the membrane damage achieved by local illumination with a 405 nm laser (See Section 3.3). Significant enrichment of zfWRRFK-TM-C was shown at the damage site 270 s after membrane damage, whereas zfWAAFK-TM-C showed no accumulation in the same time range (Figure 4.2b). To quantitatively analyze the recruitment, averaged fluorescence intensities at the damaged sites in HeLa cells are shown in Figure 4.2c. These experiments suggested that the C-terminal short fragment of Dysf, zfWRRFK-TM-C, accumulates efficiently after membrane damage both in live zebrafish and HeLa cells. The WRRFK-motif, especially the RR, is required for the accumulation of the Dysf fragment in membrane repair process.

Since a key feature of the five-AA motif is the positive net charge, we thus asked what happens to the accumulation of Dysf in response to membrane injury when we mutate the motif but keep the positive charges or gradually remove them. Therefore, we mutated the motifs (zebrafish: WRRFK; human: WRRKR) to different variants by replacing arginines and/or lysines with lysines, arginines and/or alanines in both zebrafish Dysf (WRRFK-TM-C) and human Dysf (WRRFR-TM-C). All mutants were tested in the skeletal musculature of zebrafish embryos (Figure 4.3).

Zebrafish were always injected with the same amount of plasmid, and only well-expressing myofibers with relative bright fluorescence were selected for membrane damage analysis (Figure 4.3a). For zebrafish Dysf, substituting arginines by lysines or vice versa did not lead to a significant change of accumulation (Figure 4.3a, b) suggesting that it is not the structure of the AAs but the positive charge that matters. In the mutants WARFK-TM-C, WRAFK-TM-C, and WAKFK-TM-C, the net positive charge was reduced, resulting in impaired accumulation at the site of lesion (Figure 4.3a, b). Further replacement of double arginines to double alanines led to even weaker accumulation (WAAFR-TM-C, WAAFK-TM-C). Total lack of the positively charged motif (TM-C) completely abolished the recruitment of the Dysf fragment to the lesion site (Figure 4.3a, b). The same phenomenon was observed with the wild-type and mutants of the human Dysf fragment (WRRFR-TM-C) when they were tested in zebrafish (Figure 4.3c).

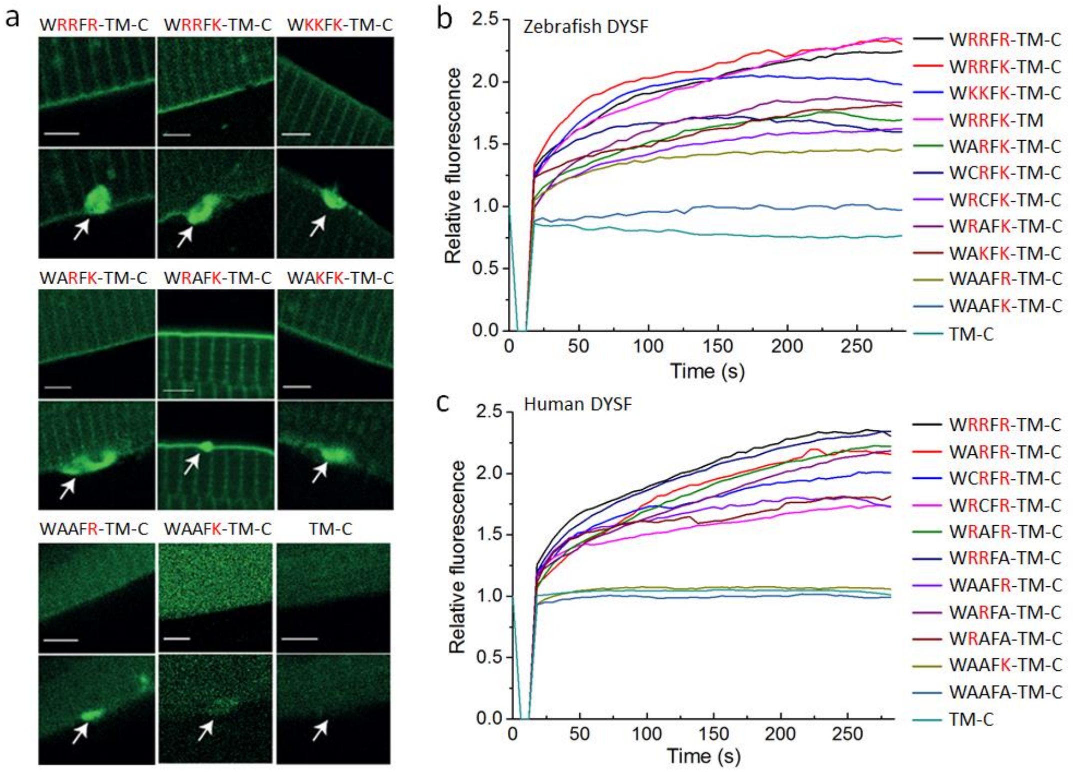

Figure 4.3 Accumulation of Dysf is influenced by the positive charge of the five-AA motif. (a) Representative images show accumulation of a zebrafish Dysf fragment (WRRFK-TM-C) and different mutants. (b, c) Accumulation kinetics of zebrafish Dysf and human Dysf mutants at the damaged region. The data are scaled such that 100% corresponds to fluorescence from the same area before damaging. Intensity courses are averages of 9 – 15 damaged cells. Scale bars, 4 µm.

We further quantitatively analyzed the cytoplasmic fluorescence of zebrafish embryos with different zebrafish Dysf mutants. All mutants in Figure 4.3b were used to calculate the cytoplasmic fluorescence intensity (averaged from 9-15 myofibers for each mutant) before membrane damage. Interestingly, the positive charge also determined the cellular distribution of the Dysf fragments. Constructs with a decreased positive charge from the five-AA motif showed an increased cytoplasmic distribution indicating a reduced plasma membrane and T-tubule localization in the absence of injury (Figure 4.4). Therefore, the increased accumulation in the repair patch of highly positively charged protein fragments may be a simple consequence of the increased amount of protein fragments in the plasma membrane prior to lesioning.

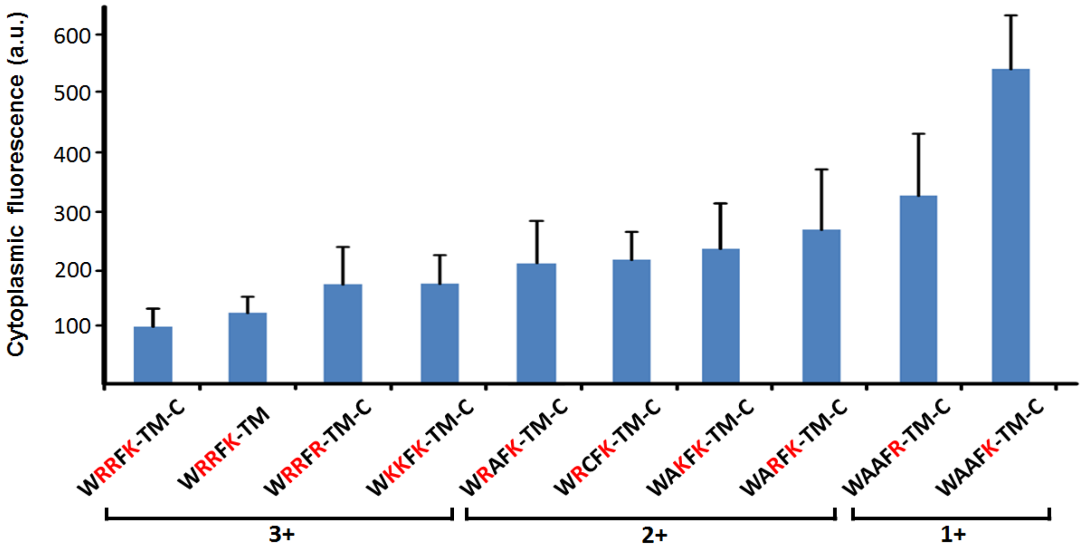

Figure 4.4 The membrane distribution of zebrafish Dysf depends on the positive charge in the WRRFK-motif. The numbers at the bottom show 1 to 3 positive charges contained in different motifs under physiological conditions.

4.1.2 Mutation K279A leads to aggregation of MG53

In mouse MG53, we found a six-AA motif WKKMFR with a high positive charge, which is very similar to the positively-charged motif in zebrafish Dysf (WRRFK) as we discussed above. To investigate the roles of these positively-charged AAs in MG53, we obtained the fusion protein MG53:turboGFP plasmid from OriGene (OriGene, Rockville, MD, USA). We noticed that the C-terminally fused turboGFP leads to a pure cytosolic distribution of MG53 without membrane targeting (Figure 4.5). Since MG53 was reported to be distributed both in the cytosol and on the membrane [12], the C-terminally fused turboGFP apparently influences the membrane targeting of MG53. Similarly, it has also been reported that the MG53:GFP showed mislocalization in the cytosol, whereas the GFP:MG53 localized correctly on the cell membrane [27].

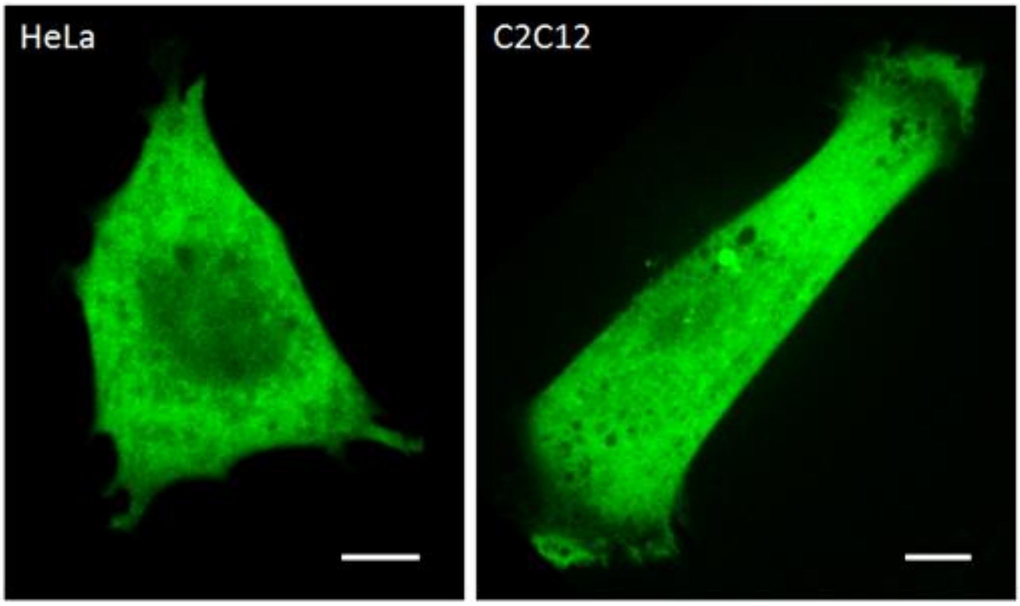

Figure 4.5 Representative images of MG53:turboGFP in a HeLa cell and a C2C12 myoblast, respectively. Different from turboGFP:MG53, the C-terminal turboGFP severely influence the membrane targeting of MG53 and leads to pure cytosolic distribution. Scale bars, 10 µm.

Therefore, our technician Julia Kuhlmann cloned the turboGFP:MG53 for further measurement, where turboGFP was fused N-terminally to the MG53. The positively charged motif (WKKMFR) contains two lysines and one arginine and locates very close to the N-terminus of the SPRY domain connecting to the TRIM domain (Figure 4.6a). TurboGFP:MG53 and its mutants K278A, K279A and R282A were imaged in HeLa cells, respectively. Constructs were modified by site-directed mutagenesis using PCR. As shown in Figure 4.6b, similar to turboGFP:MG53, mutants K278A and R282A distributed both on the membrane and in the cytosol. Surprisingly, the mutation K279A showed a very unusual phenotype with a lot of very bright vesicles. Apparently, the mutant K279A aggregated in intracellular vesicles.

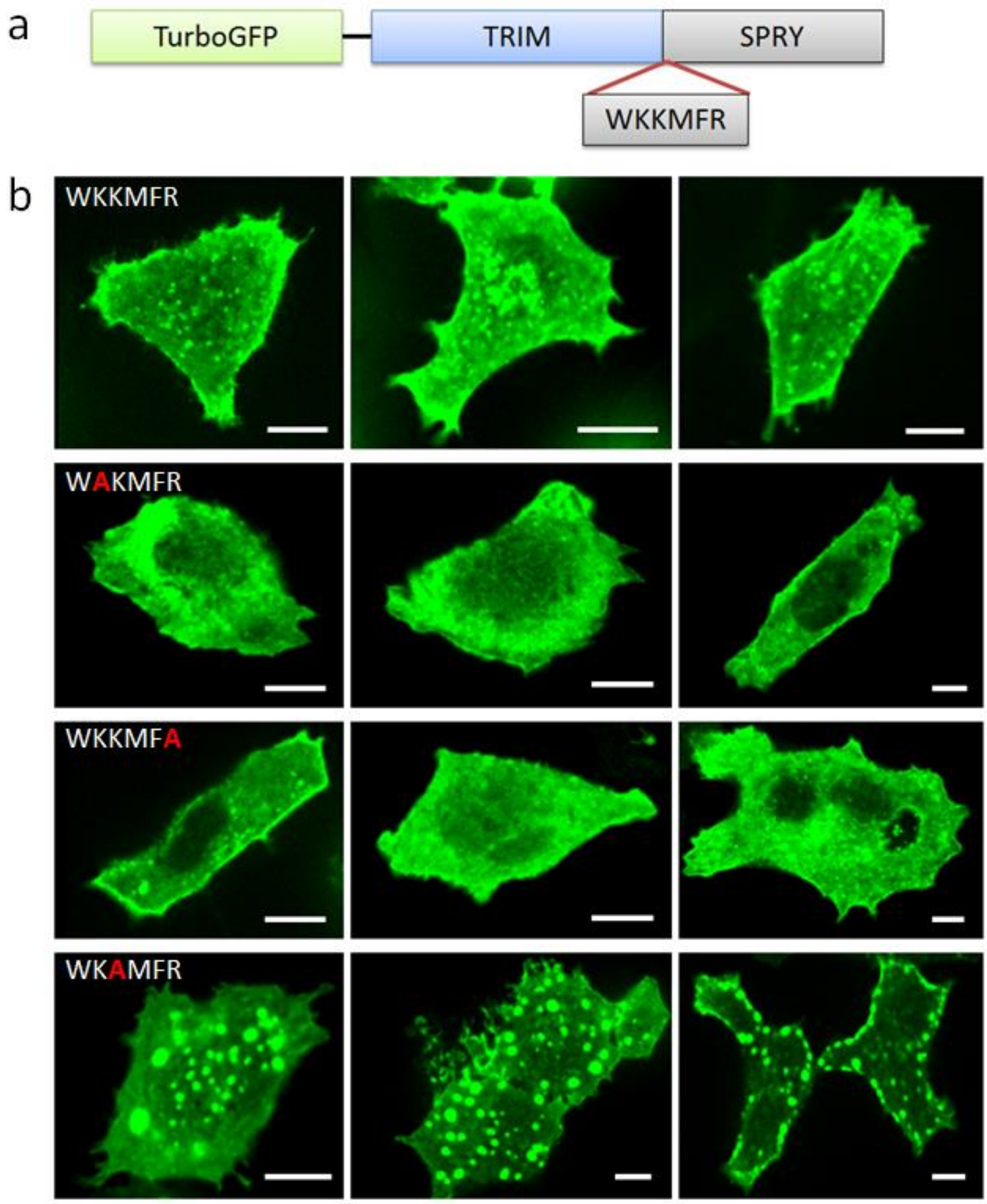

Figure 4.6 Mutation of K279A leads to mislocalization of MG53. (a) Domain structure of the fusion protein turboGFP:MG53. (b) Localization of turboGFP:MG53 and mutants (K278A, K282A, K279A) in HeLa cells. Three representative images are shown for each. Scale bars, 10 µm.

We further tested the same plasmids in the mouse C2C12 cell line, which is known as an immortalized mouse myoblast cell line. The imaging in the C2C12 myoblasts showed the same results as in the HeLa cells (Figure 4.7). The particular vesicular distribution of the mutant K279A in both HeLa and C2C12 cells is very similar to the aggregation of single TRIM domains observed in reference [27]. These observations suggest that the lysine (K279) from the six-AA motif in the SPRY domain plays a significant role in the localization of MG53.

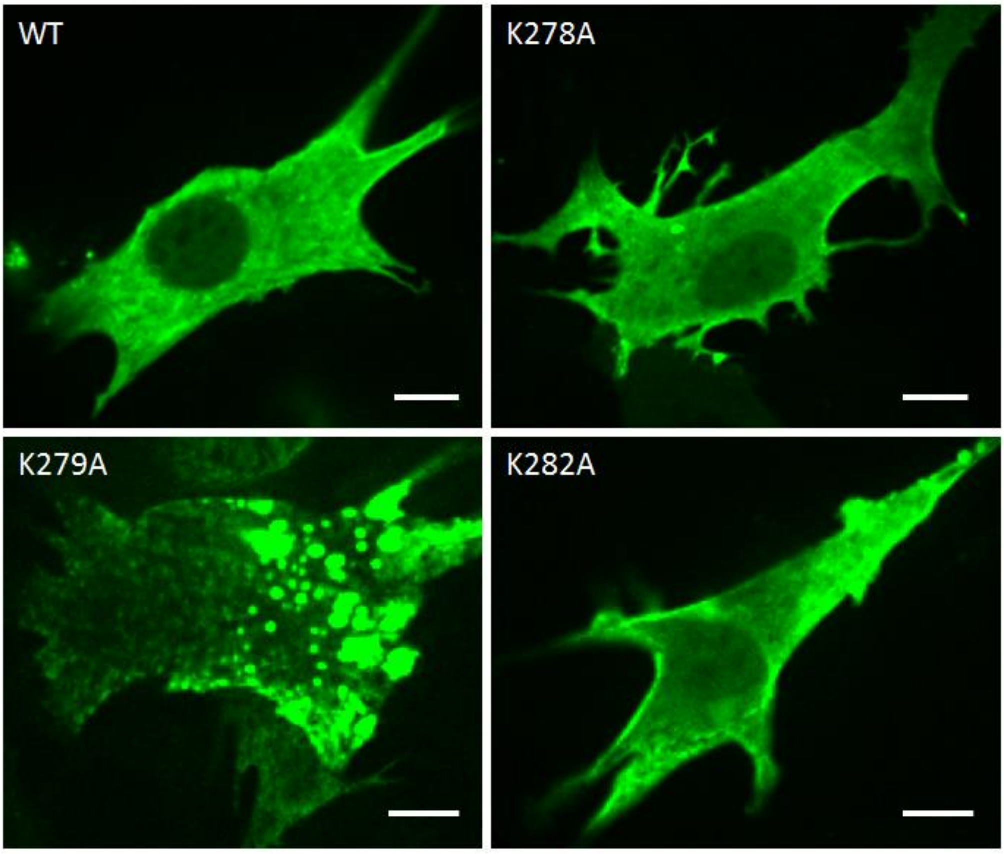

Figure 4.7 Representative images of turboGFP:MG53 and mutants (K278A, K282A, K279A) in C2C12 myoblasts. Similar to HeLa cells, mutant K279A showed significant vesicular distribution. Scale bars, 10 μm.

We also compared the accumulation capacity of turboGFP:MG53 and mutant K279A in HeLa cells. As shown in Figure 4.8a (upper panel), turboGFP:MG53 functioned well in HeLa cells with efficient accumulation after membrane damage. The mutant K279A also showed membrane recruitment in the repair patch (Figure 4.8a, lower panel), however, quantitatively analysis demonstrated that the accumulation was significantly weaker (Figure 4.8b). This could happen because of aggregation of MG53(K279A), which leads to less cytosolic ‘free’ MG53 for oligomerization in the repair patch.

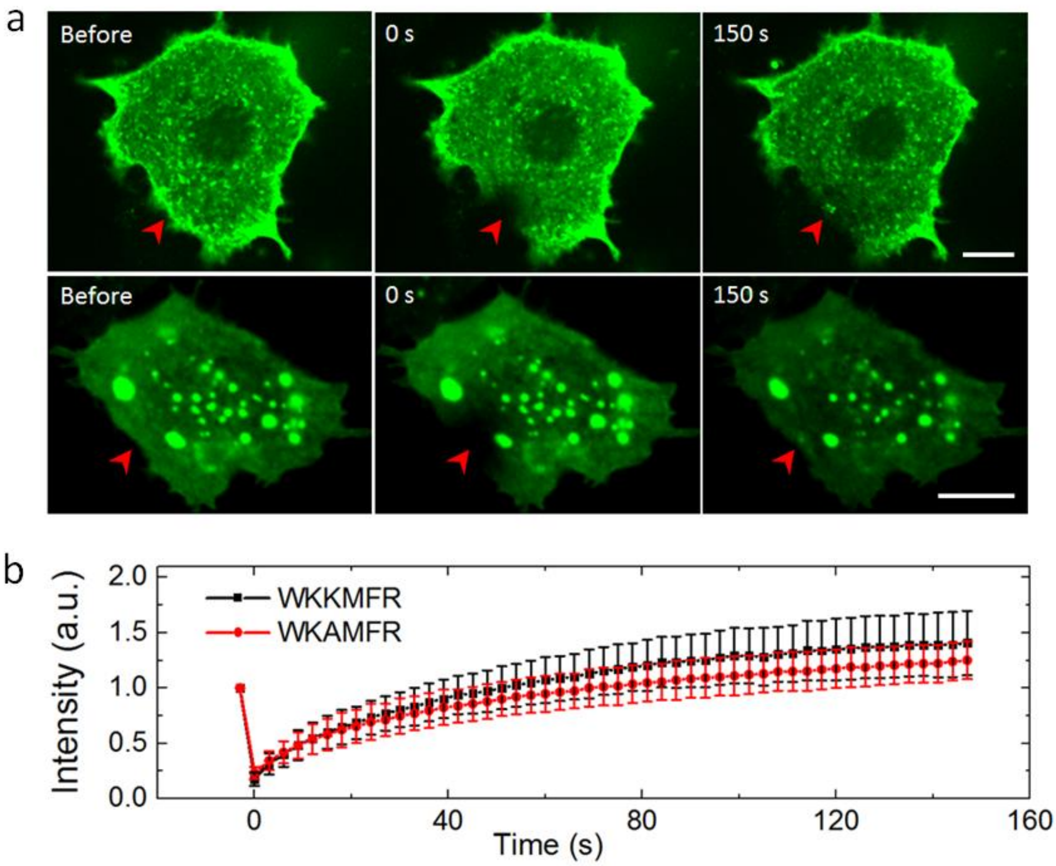

Figure 4.8 Accumulation of MG53 is influenced by K279. (a) Accumulation of MG53 (upper panel) and mutant K279A (lower panel) in HeLa cells after membrane damage. Arrows indicate the damaged region. Scale bars, 10 µm. (b) Normalized intensity courses at the damaged area (10 cells for each, mean ± SD).

We employed two-channel imaging with a spinning-disk confocal microscope to check the colocalization of aggregated MG53(K279A) with early endosomes, late endosomes, lysosomes and inclusion bodies. Early and late endosomes were labeled with mRFP-Rab5A and mRFP-Rab7 [144], respectively. mRFP-Rab5 and mRFP-Rab7 were gifts from Ari Helenius (Addgene plasmid # 14436). As shown in Figure 4.9a and b, small vesicles in the green channel (turboGFP:MG53 (K279A)) showed distinct colocalization with early and late endosomes in the red channel. However, for the big bright MG53(K279A)-enriched vesicles, no colocalization with early or late endosomes can be observed. To check colocalization with lysosomes, LysoTracker Blue DND-22 (Thermo Fisher Scientific) was used to label the lysosomes according to the manufacturer's protocol. Still, no apparent colocalization was observed (Figure 4.9c).

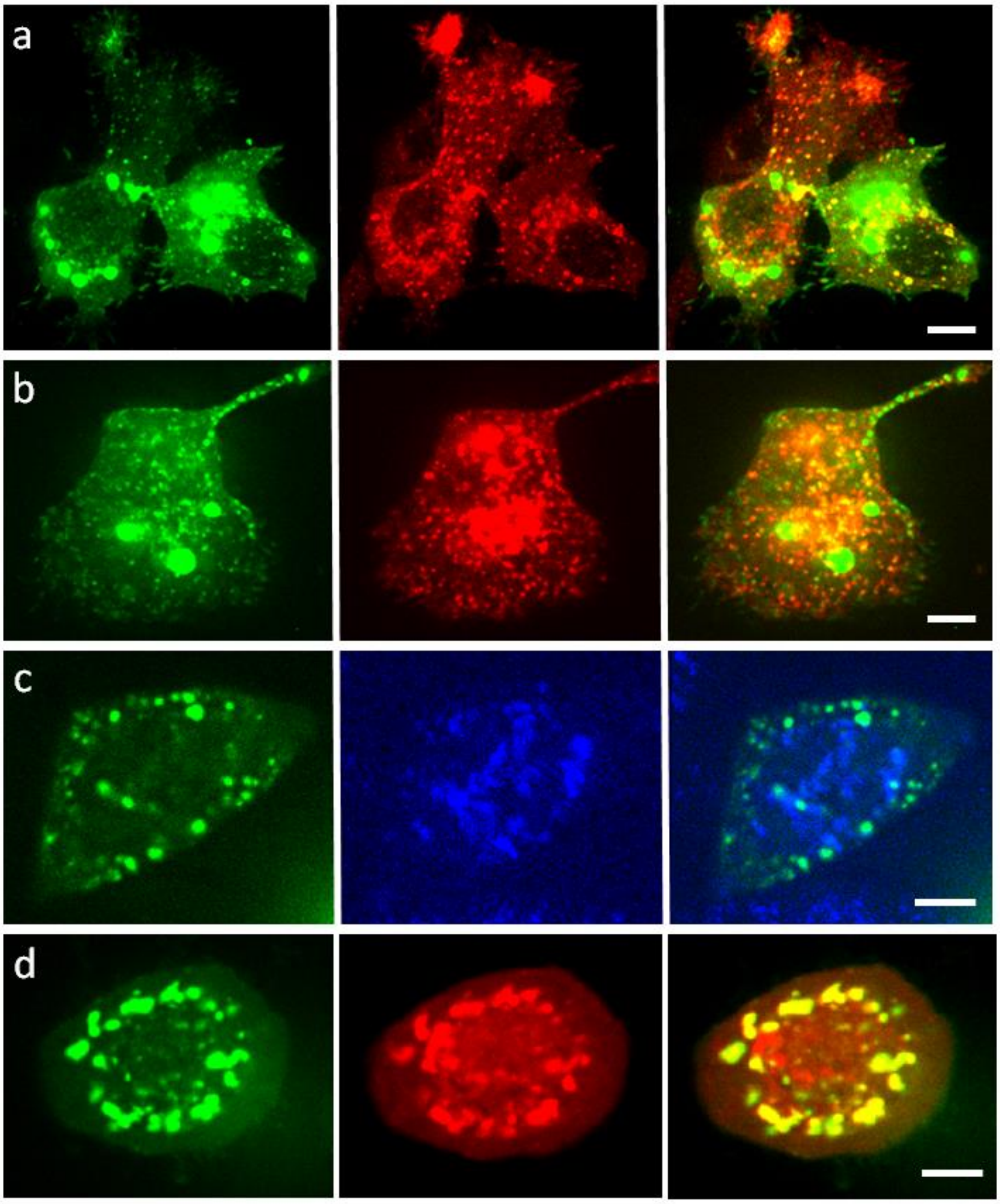

Figure 4.9 Two-channel imaging of turboGFP:MG53 (green) with (a) early endosomes (red), (b) late endosomes (red), (c) lysosomes (blue), and (d) inclusion bodies (red). Scale bars, 10 µm.

Finally, we labeled inclusion bodies with mRFP-ubiquitin [145] to check colocalization with MG53(K279A). The plasmid, mRFP-ubiquitin, was a gift from Nico Dantuma (Addgene plasmid # 11935). Surprisingly, the MG53(K279A) aggregation showed a high degree of colocalization with inclusion bodies (Figure 4.9d). In general, inclusion bodies are formed by aggregation of misfolded protein and will be degraded through autophagy [146]. The single mutation K279A thus appears to result in misfolding of MG53 and formation of aggregates in inclusion bodies.

We further investigated possible reasons for the aggregation of MG53(K279A) in inclusion bodies. One hypothesis is that K279 is essential for phosphorylation of MG53 and the mutant K279A leads to severe failure of phosphorylation and mislocalization. Therefore, we mutated K279 to serine (K279S) and tyrosine (K279Y), respectively, assuming that the serine (S) and/or tyrosine (Y) could rescue phosphorylation [147]. However, mutants K279S and K279Y still showed severe aggregation and no membrane targeting, which suggested that the mislocalization was not related to the phosphorylation (Figure 4.10a). Then we questioned whether the missing positive charge is the reason for this phenotype. Therefore, we mutated K279 to arginine (R) to keep the positive charge in the same position. Surprisingly, mutant K279R showed correct membrane and cytoplasmic distribution as the wildtype, and no distinct aggregation could be observed (Figure 4.10b). These results suggest that the aggregation of MG53(K279A) was induced by losing of the positive charge.

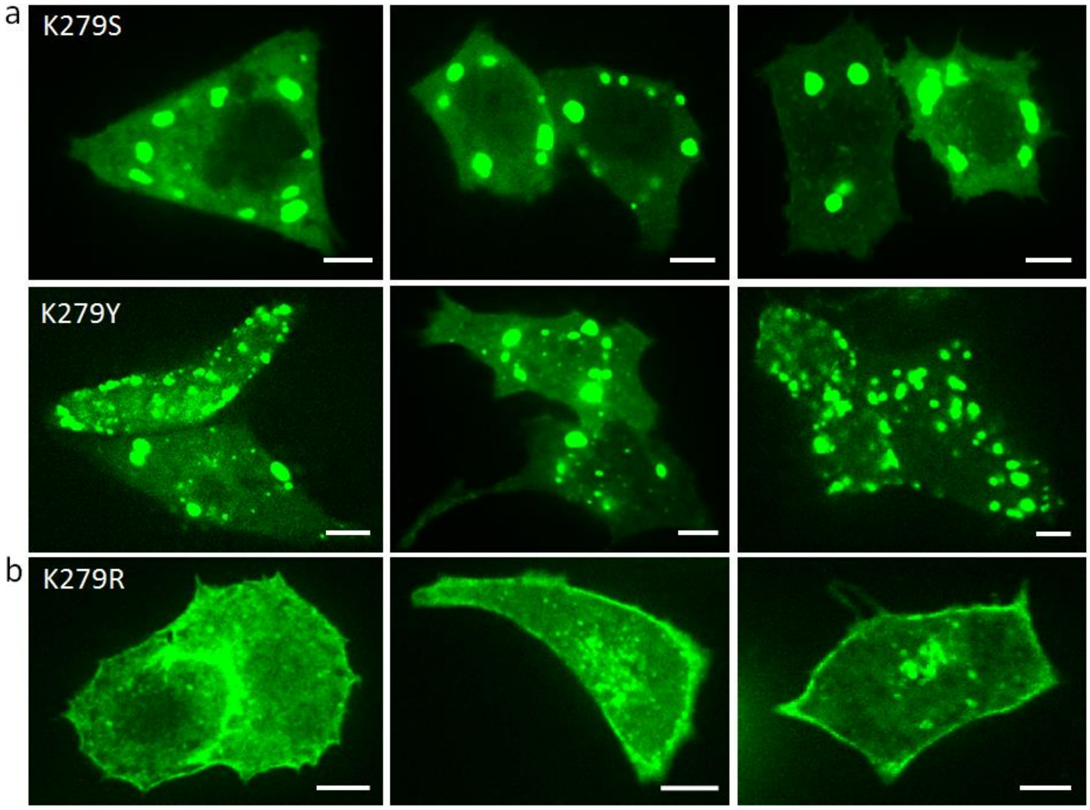

Figure 4.10 Localization of turboGFP:MG53 mutants K279S, K279Y, and K279R in HeLa cells. Three representative images are shown for each. Scale bars, 10 µm.

The same plasmids were also tested in the C2C12 cell line. As shown in Figure 4.11, the same result was observed as in HeLa cells, that K279R rescued the membrane targeting of MG53, whereas K279S and K279Y did not. These results suggest that aggregation of MG53(K279A) was induced by losing the positive charge at a critical AA position (K279), which is consistent with the previous observations on Dysf.

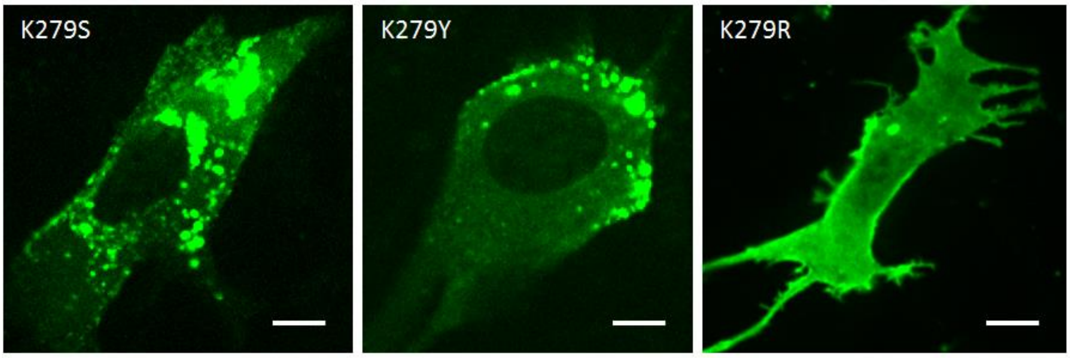

Figure 4.11 Representative images of turboGFP:MG53 with mutation K279S, K282Y, K279R in C2C12 myoblasts. Similar to HeLa cells, K279R rescues the membrane targeting of MG53. Scale bars, 10 µm.

4.2 Dysferlin facilitates PS accumulation

In this work, besides studying the recruitment of functional proteins such as MG53 and Dysf, we also investigated whether different membrane phospholipids can also accumulate at the lesion after membrane damage. Surprisingly, among several tested phospholipids, only phosphatidylserine (PS) and cholesterol showed enrichment selectively in the repair patch [123]. Considering that PS was previously shown to interact with Dysf [15], we thus wondered, whether Dysf plays a role in the accumulation of PS at the membrane lesion.

Together with Dr. Volker Middel, we inflicted membrane wounds in myofibrils expressing the PS sensor LactC2:GFP [120] both in control zebrafish and zebrafish after knock-down (KD) of the endogenous Dysf by a morpholino (MO) [25]. As a control experiment, injection of a 5-base-pair mismatch MO led to normal PS accumulation (Figure 4.12a and c, green curve), whereas injection of Dysf-MO abolished the rapid accumulation of PS in the repair patch (Figure 4.12b and c, red curve). Moreover, co-injection of the Dysf-MO together with the Dysf:mOrange plasmid [25] restored the accumulation of PS in the repair patch (Figure 4.12c, yellow curve). This suggests that PS recruitment in Dysf-KD myofibers is successfully rescued by Dysf:mOrange, which further proves the essential role of Dysf in the PS accumulation.

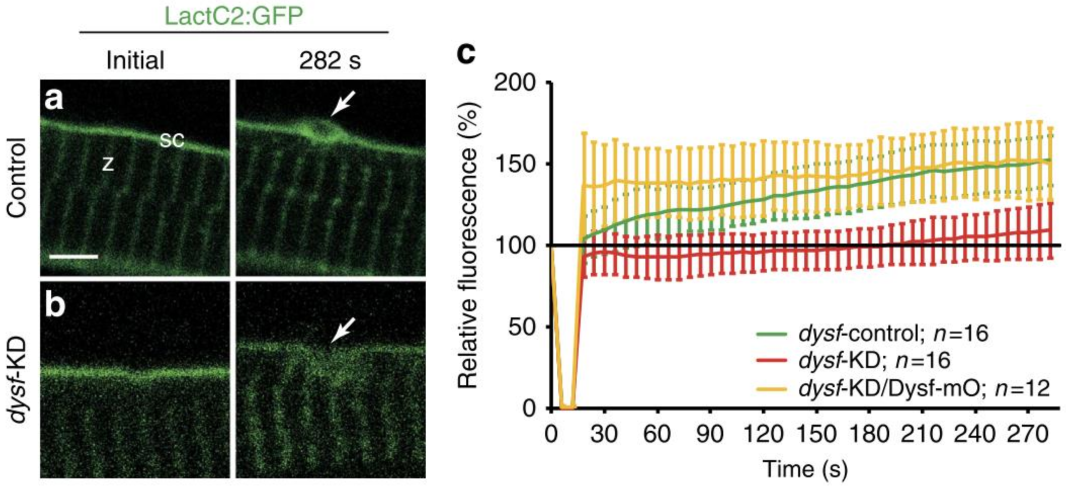

Figure 4.12 Dysferlin facilitates PS accumulation. (a, b) Before damage, LactC2:GFP localized to the sarcolemma (sc) and the Z-line (z) both in control (a) and Dysf-KD myofibers (b). After membrane injury, LactC2:GFP accumulated in the control (a, arrow) but not in the Dysf-KD myofiber (b, arrow). (c) Kinetics of the LactC2:GFP intensity at the damage site in control (green), Dysf-KD (red) and Dysf-KD embryos co-injected with Dysf:mOrange (yellow). Scale bar, 4 µm. Image adopted from reference [123].

A similar experiment was also performed in the HeLa cell line and the mouse C2C12 muscle cell line. HeLa cells express vey low levels of endogenous Dysf [143]. Therefore, different from zebrafish muscle cell, there is no obvious accumulation of PS in HeLa cell after membrane damage (Figure 4.13a). However, co-expression of zebrafish zfWRRFK-TM-C:mCherry with LactC2:GFP led to the high enrichment of PS at the site of lesion (Figure 4.13b, upper panel), which was well colocalized with the accumulated zfWRRFK-TM-C:mCherry at the damage site (Figure 4.13b, lower panel). Thus, the C-terminal fragment of zebrafish Dysf could also mediate PS accumulation at the membrane lesion in human cells.

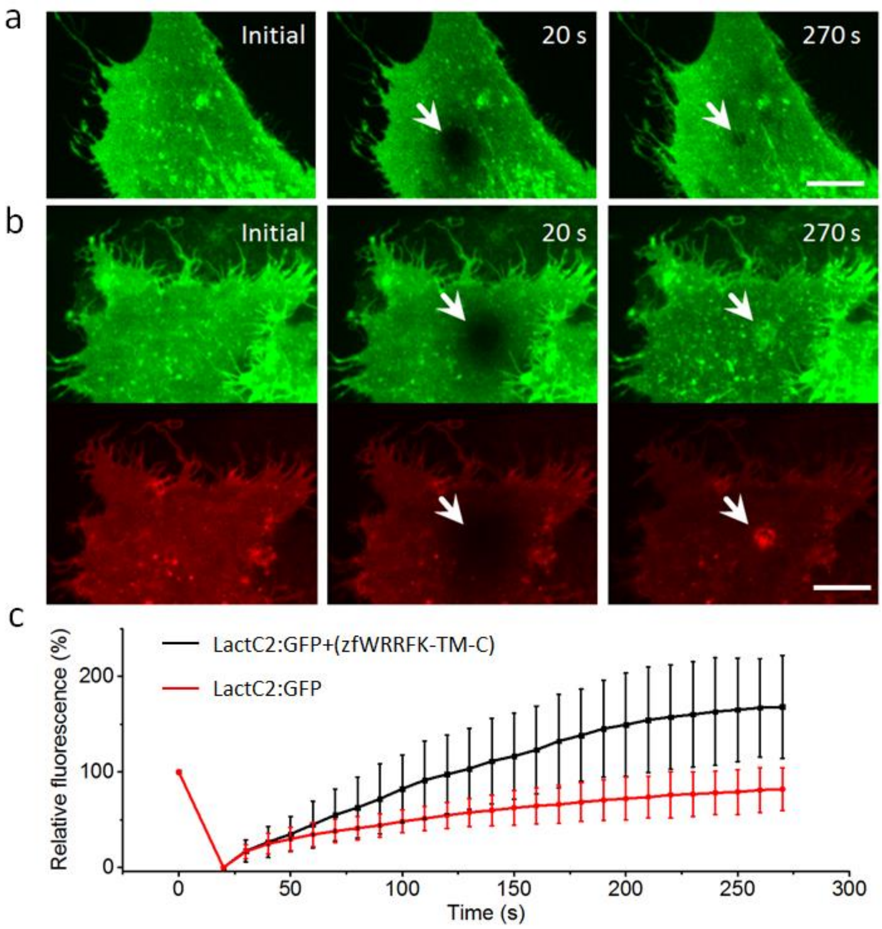

Figure 4.13 Zebrafish Dysf rescues PS accumulation in HeLa cells. (a) HeLa cells transfected with LactC2:GFP and imaged before and after membrane damage (arrows). No obvious accumulation of PS, but only fluorescence recovery after photobleaching occurred at the lesion site. (b) In the presence of zfWRRFK-TM-C:mCherry, LactC2:GFP accumulated (green) within the repair patch (arrows), corresponding with the accumulation of zfWRRFK-TM-C:mCherry (red). (c) Kinetics of LactC2:GFP intensity at the damage site with (black) and without co-expressing zfWRRFK-TM-C:mCherry (red). Scale bars, 10 μm. Image adopted from reference [123].

In the mouse muscle cell line C2C12, the level of endogenous expressed Dysf increases during the muscle cell differentiation process. Similar to HeLa cells, undifferentiated C2C12 myoblasts contain a low amount of endogenous Dysf. Therefore, LactC2:GFP accumulated only when co-expressing with zfWRRFK-TM-C:mCherry (Figure 4.14), which is the same within HeLa cells.

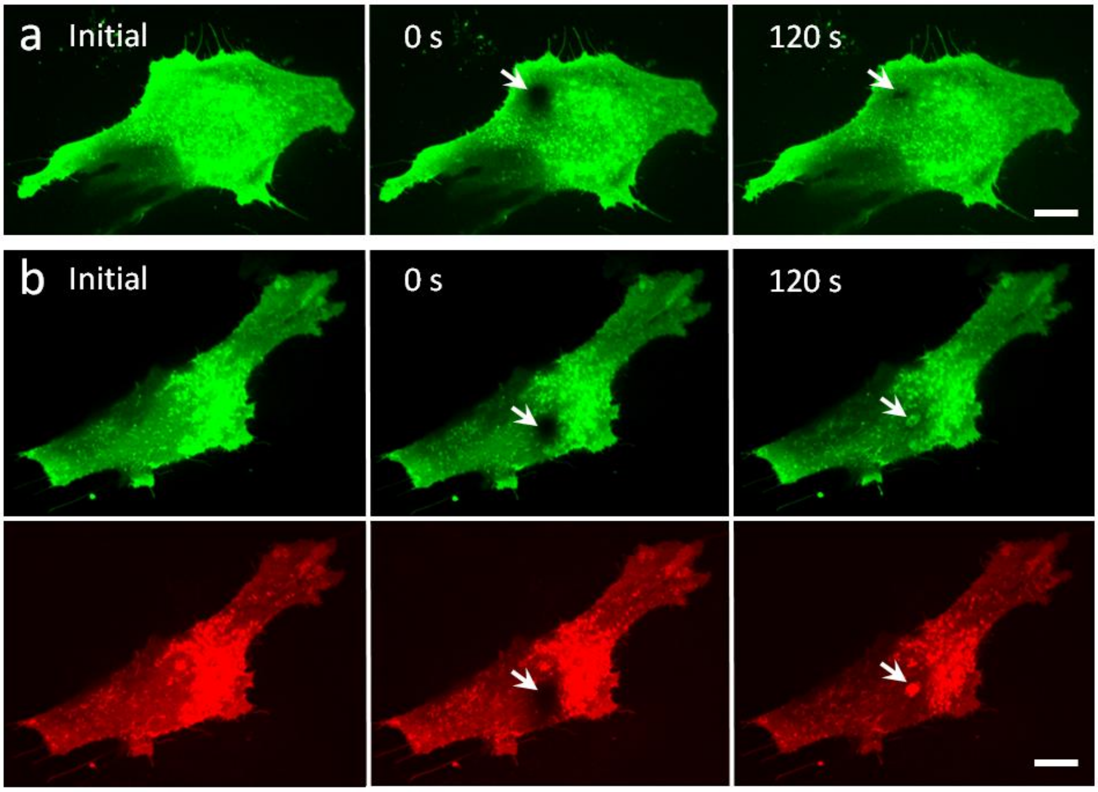

Figure 4.14 Zebrafish Dysf rescues PS accumulation in C2C12 myoblasts. (a) C2C12 cells transfected with LactC2:GFP, imaged before and after membrane damage (arrows). No accumulation of PS appeared at the lesion site. (b) In the presence of zfWRRFK-TM-C:mCherry, LactC2:GFP accumulated (green) within the repair patch (arrows), corresponding with the accumulation of zfWRRFK-TM-C:mCherry (red). Scale bars, 10 µm.

In contrast, when C2C12 cells were differentiated to myotubes, which express high amounts of endogenous Dysf, LactC2:GFP showed enrichment at the lesion even without co-transfection of zfWRRFK-TM-C:mCherry (Figure 4.15). This observation further suggests that PS accumulation is facilitated by Dysf and the underlying mechanisms are conserved in fish, mouse, and human cells.

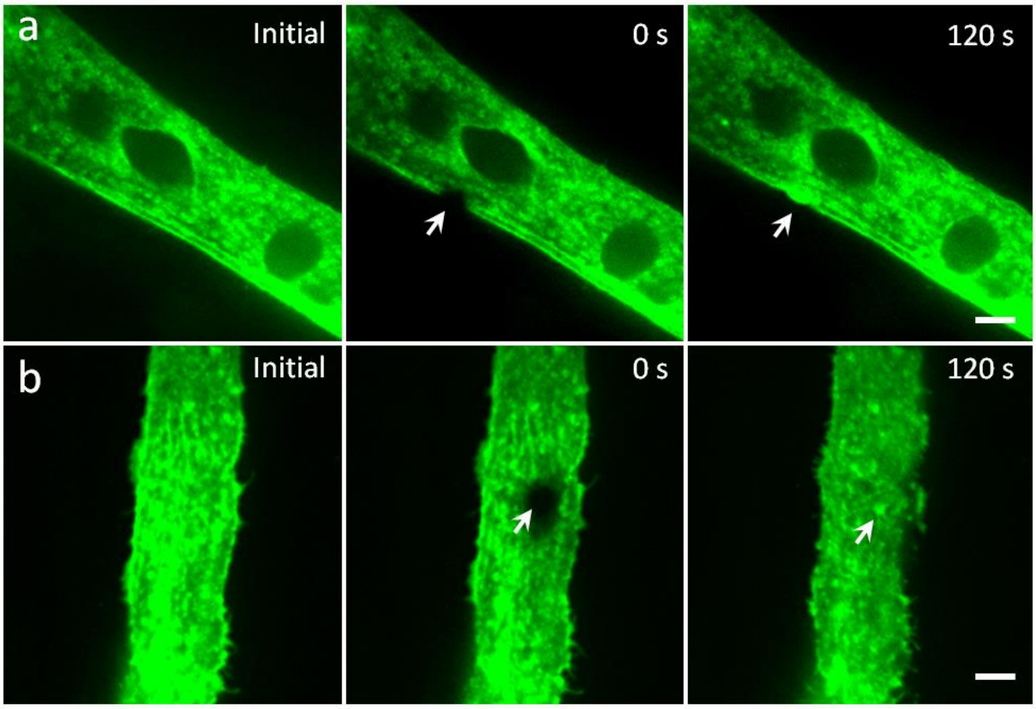

Figure 4.15 PS accumulation in C2C12 differentiated myotubes. C2C12 cells transfected with LactC2:GFP and induced to myotubes. Cells were imaged before and after membrane damage on the side membrane (a) and bottom membrane (b). PS quickly recruits to the damage sites (arrows). Scale bars, 10 µm.

4.3 Dysferlin and PS transport from adjacent membrane to the lesion

To assess the movement of Dysf on the membrane of damaged myofibers, we employed fluorescence loss in photobleaching (FLIP) experiments. Dysf:mOrange expressing myofibers were imaged with a spinning disk confocal microscope and then damaged by targeted 405 nm laser irradiation (See Section 3.3) (Figure 4.16a, upper panel). Light exposure also caused substantial bleaching at the site of the lesion. Subsequently, images were taken for 118 s in steps of 1 s to measure the time course of fluorescence in the regions close to but separated from the irradiated area (Figure 4.16a, upper panel, blue box). As a control, a similar experimental protocol was performed except for irradiating with a 561 nm instead of the 405 nm laser, which only bleaches but does not damage the local membrane (Figure 4.16a, lower panel).

For quantification, a region on the membrane, 5 – 15 µm displaced from the site of lesion/irradiation, was selected to analyze the integrated fluorescence intensity over time (Figure 4.16a, blue boxes). To account for the bleaching effect during image acquisition, data was rescaled by normalizing the local fluorescence intensity based on the fluorescence emission of the entire myofiber. After local bleaching using 561 nm irradiation, there was a fluorescence intensity decrease in the region of interest during the first 50 s followed by slow recovery (Figure 4.16b, black). This loss of fluorescence is because of the redistribution of fluorescence markers to remove concentration gradients due to local photobleaching, an effect utilized by the FLIP method [148]. After local bleaching and membrane damage using 405-nm irradiation, the fluorescence intensity decreased faster and to a significantly lower level (Figure 4.16b, red). The faster kinetics and greater extent of fluorescence loss than in the control experiment suggest that Dysf from adjacent sarcolemmal regions is recruited to the membrane damage site.

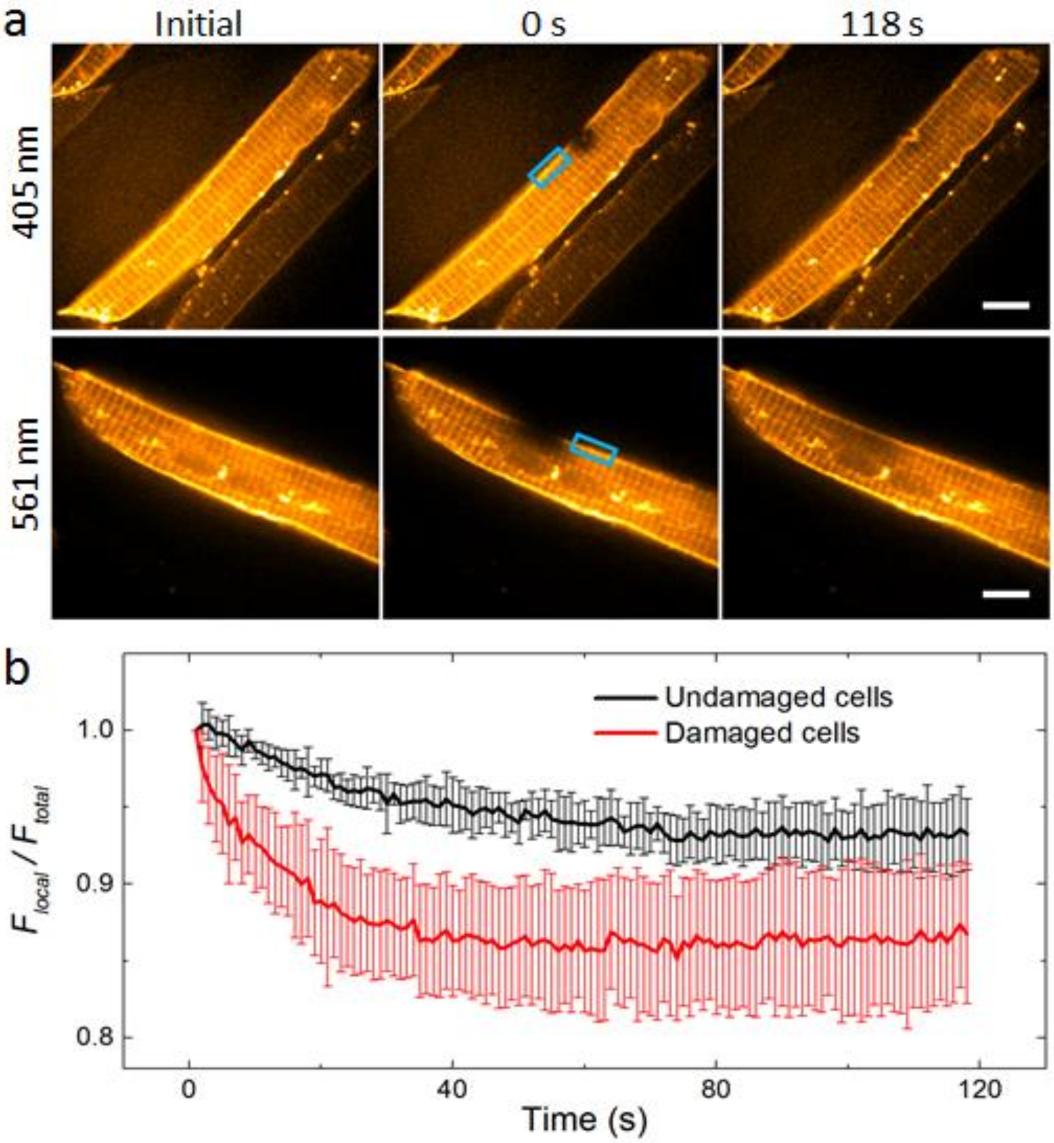

Figure 4.16 FLIP experiment proves that Dysf is recruited from the adjacent membrane. (a) FLIP analysis on selected regions (blue boxes) of live Dysf:mOrange expressing myofibers. Photobleaching and membrane damaging using a 405 nm laser (upper) and photobleaching only using a 561 nm laser (lower). (b) 561 nm irradiation results in an intensity decrease by 6% (black); 405 nm irradiation results in a more rapid decrease by 14% (red). Scale bars, 10 µm. Image adopted from reference [123].

We further employed trajectory analysis based on super-resolution localization microscopy to directly visualize the recruitment of Dysf to the lesion at the single-molecule level. To this end, zfWRRFK-TM-C was N-terminally fused with photoactivatable fluorescent protein mEosFP*thermo* and injected into zebrafish embryos. A membrane lesion was induced by 405 nm laser irradiation on the PALM microscope (See Section 3.3), and the myofiber was imaged within 1 - 2 min after membrane damage. Short trajectories of mEosFP*thermo*:zfWRRFK-TM-C were acquired from the molecule locations in (typically 4 – 5) sequential image frames. To assess the presence of directed motion toward the site of lesion in the adjacent region of the wound, we calculated the R_{proj} value in the adjacent membrane region towards the damage site (see Section 3.5). Molecules from sequential frames were linked with 400 nm maximum displacement between successive frames. By limiting the photon threshold value, only the trajectories the highest precision can be selected (130 ± 5 of typically 500 trajectories) for each measurement and further analyzed within the measured region 2 – 15 µm away from the damage site (Figure 4.17a).

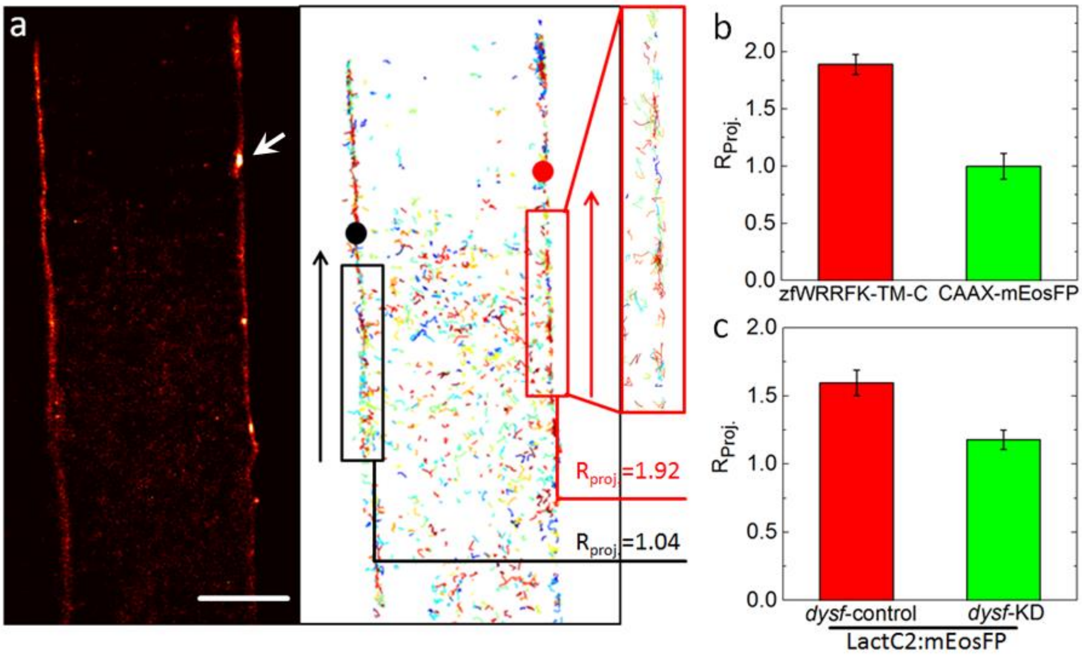

Figure 4.17 Trajectory analysis shows Dysf and PS transport from the adjacent membrane to the lesion. (a) PALM image of mEosFP*thermo*:zfWRRFK-TM-C in zebrafish myofiber and single molecule trajectories calculated from the image data. The arrow indicates the site of the lesion. Molecules near the lesion (red box) show a high tendency ($R_{proj.}$ = 1.92) to move towards the damage site (red dot). In the undamaged sarcolemma, trajectories (black box) did not show directed motion towards the black dot ($R_{proj.}$ = 1.04). (b) mEosFP*thermo*:zfWRRFK-TM-C moved towards the lesion (red column); the control CAAX-mEosFP*thermo* did not (green column; $p<10^{-8}$). (c) The PS sensor LactC2:mEosFP*thermo* moved towards the lesion in the control (red column) but not in the Dysf-KD zebrafish (green column; $p<10^{-8}$). Significance was tested by Student’s t-test. Scale bar, 5 µm.

As shown in Figure 4.17a, for a damaged muscle cell, $R_{proj.} = 1.92$ in the adjacent membrane regions (red box), which indicated a strong tendency to move towards the damage site (red dot) and accumulate at the membrane lesion. For the membrane region on the left (black box), the directional motion is absent, as quantified by $R_{proj} = 1.04$, calculated with respect to a fictive point (black dot). Statistical analysis of zebrafish injected with mEosFP*thermo*:zfWRRFK-TM-C and CAAX:mEosFP*thermo* (control) showed a significant difference of the R_{proj} values within adjacent regions close to the damage site (Figure 4.17b, Student's t-test $p<10^{-8}$). This result clearly proved that Dysf on the adjacent membrane transports positively towards the lesion, instead of the overall membrane shifting after membrane damage.

We performed additional single molecule tracking experiments by using the PS sensor LactC2:mEosFP*thermo* in Dysf-KD and control (5-base-pair mismatch MO) embryos. LactC2:mEosFP*thermo* showed a much higher tendency to move toward the lesion in the control than in the Dysf-KD embryos (Figure 4.17c, $p<10^{-8}$), which further supports our claim that Dysf plays a decisive role in translocating PS within the membrane to the damage site.

4.4 Discussion

Lesions in the cell membrane rapidly lead to repair protein recruitment at the damaged site, such as Dysf and MG53, to form repair patches preventing cell death. The C-terminal short fragment of zebrafish Dysf (WRRFK-TM-C) showed fast accumulation after membrane damage [123]. In this study, we provide evidence that efficient accumulation of Dysf requires positive charges from arginines and lysine in the motif WRRFK. Reducing the positive charges or loss of the motif led to a significant deficiency in the repair function of Dysf. Further investigations showed that the positive charges also strongly influence the localization of Dysf. Fewer positive charges resulted in a more cytoplasmic distribution of Dysf. Therefore, membrane targeting of Dysf highly depends on the positive charges from the five-AA motif, which is presumably a prerequisite for the repair function of Dysf.

We noticed that there is a very similar positively charged motif in mouse MG53 (WKKMFR). Then we questioned whether the positive charges in this motif also influence the localization and repair function of MG53. We observed that a single lysine (K279) is essential for correct localization of MG53. The single mutation K279A led to severe aggregation and vesicular distribution of MG53 in HeLa cells, which is highly similar to the localization of the single TRIM domain of MG53 observed in [27]. This observation suggests the K279 plays a significant role in localization or even further function of MG53. Two-channel imaging provided evidence that MG53(K279A) localized in inclusion bodies. Apparently, mutation K279A leads to misfolding of MG53, and the aggregated MG53(K279A) forms inclusion bodies for further degradation. We assumed two possible reasons for the misfolding and mislocalization of MG53(K279A): (1) failure of phosphorylation; (2) loss of the positive charge at the critical position, as in Dysf. We successfully rescued the localization of MG53 with the mutation K279R, but failed with the mutation K279Y and K279S. This observation firmly proves that K279 is essential for proper localization of MG53 due to its positive charge, but not its role in phosphorylation. Therefore, the functions of the positive charge in the two similar motifs from Dysf and MG53 are consistent.

Our research of the membrane repair process did not only focus on functional proteins, such as Dysf and MG53, but also on membrane phospholipids. Among the lipids tested, only PS accumulated efficiently in the repair patch, suggesting that the lesion patch is selectively enriched in PS. This is in agreement with the observation that general membrane markers do not accumulate at the site of lesion [25], and also in line with our previous observation that vesicles do not play a crucial role as sources of lipid in the repair patch of the zebrafish embryo [25]. Moreover, we found that PS and Dysf accumulate at the lesion site with similar kinetics, which indicates a potential involvement of Dysf in the PS translocation to the damage site. FLIP experiments and single molecule tracking showed that directed movement of PS along the membrane to the lesion depends on Dysf. Mutation of the RR in the five-AA motif from Dysf abolished PS accumulation, which further proved the interaction between PS and the positively-charged motif in Dysf. Binding of Dysf to PS was previously shown to occur via the C2A-domain of Dysf [149]. Our data suggest that the five-AA arginine-rich motif plays an additional and significant role in PS transport to the lesion. Some RR-containing peptides are known to bind PS [142]. Thus, PS may directly interact with the positively-charged motif of Dysf via the double arginine. Reducing the positive charges in the five-AA motif leads to more cytosolic distribution of Dysf in uninjured myofibers. This suggests that Dysf has to be localized correctly to the sarcolemma to allow efficient transport of PS to the lesion.

As a conclusion, we found positively-charged motifs, which play an essential role in MG53 and Dysf. For both proteins, their properties of membrane targeting and rapid accumulation are influenced by the positive charges of the motif. Further investigation of Dysf reveals an underlying interaction between Dysf and PS via the positively-charged motif. By using PALM and single molecule tracking techniques, the motion of both Dysf and PS along the membrane was clearly visualized. Quantitative trajectory analysis further proved that Dysf facilitates the transport of PS from the adjacent membrane to the damage site, which opens a new window for applying localization microscopy.

5. Super-resolution imaging and analysis of vesicle dynamics in fungal cells

5.1 Investigation of ChsB protein in *Aspergillus nidulans*

The highly polarized growth of filamentous fungi requires continuous transport of construction materials to and from the hyphal tip. To this end, proteins and other biomolecules are packaged in vesicles and transported by motor proteins along the microtubule and actin cytoskeletons. To investigate localization and transport of vesicles in *A. nidulans*, a chitin synthase, ChsB, was fused with mEosFP*thermo* for super-resolution PALM imaging, cluster analyses, and pulse-chase experiments.

5.1.1 PALM imaging and cluster analysis

ChsB localizes to the hyphal tips and concentrates particularly in the Spitzenkörper [54]. To quantitatively analyze the spatio-temporal development of the Spitzenkörper with high resolution, we employed the PALM technique to image hyphae expressing the mEosFP*thermo*:ChsB fusion protein. A pronounced fluorescent cluster of mEosFP*thermo*:ChsB at the hyphal tip was clearly visualized, representing the Spitzenkörper (Figure 5.1a, b). Moreover, multiple speckles mostly near the plasma membrane were also observed (Figure 5.1a, b). ChsB clusters at the hyphal tip were identified by the cluster analysis algorithm, as described in Section 3.6 (Figure 5.1c).

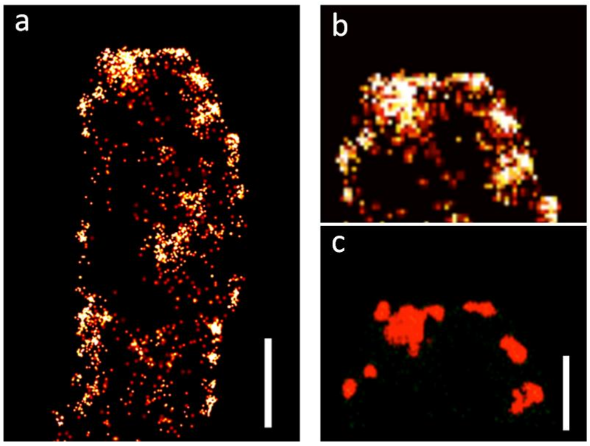

Figure 5.1: Superresolution imaging of the Spitzenkörper. (a) Localization image of a hypha labeled with mEosFP*thermo*:ChsB. (b) Zoomed image of (a) at the hyphal tip. (c) ChsB clusters identified by the cluster analysis. Scale bars, (a) 1 µm, (b, c) 300 nm. Image adopted from reference [126].

To investigate the dynamics of clusters at the hyphal apex, cluster images within 2.5 s intervals for a total period of 125 s were generated (Figure 5.2a) with the moving-window binning technique (500 frames binning with 50 frames shift, see Section 3.6) [137]. Cluster areas and numbers of mEosFP*thermo*:ChsB molecules within each cluster were calculated over the time course of the experiment (Figure 5.2b, c). The distributions of the cluster area and the number of molecules of each single cluster were also compiled in histograms (Figure 5.2d, e).

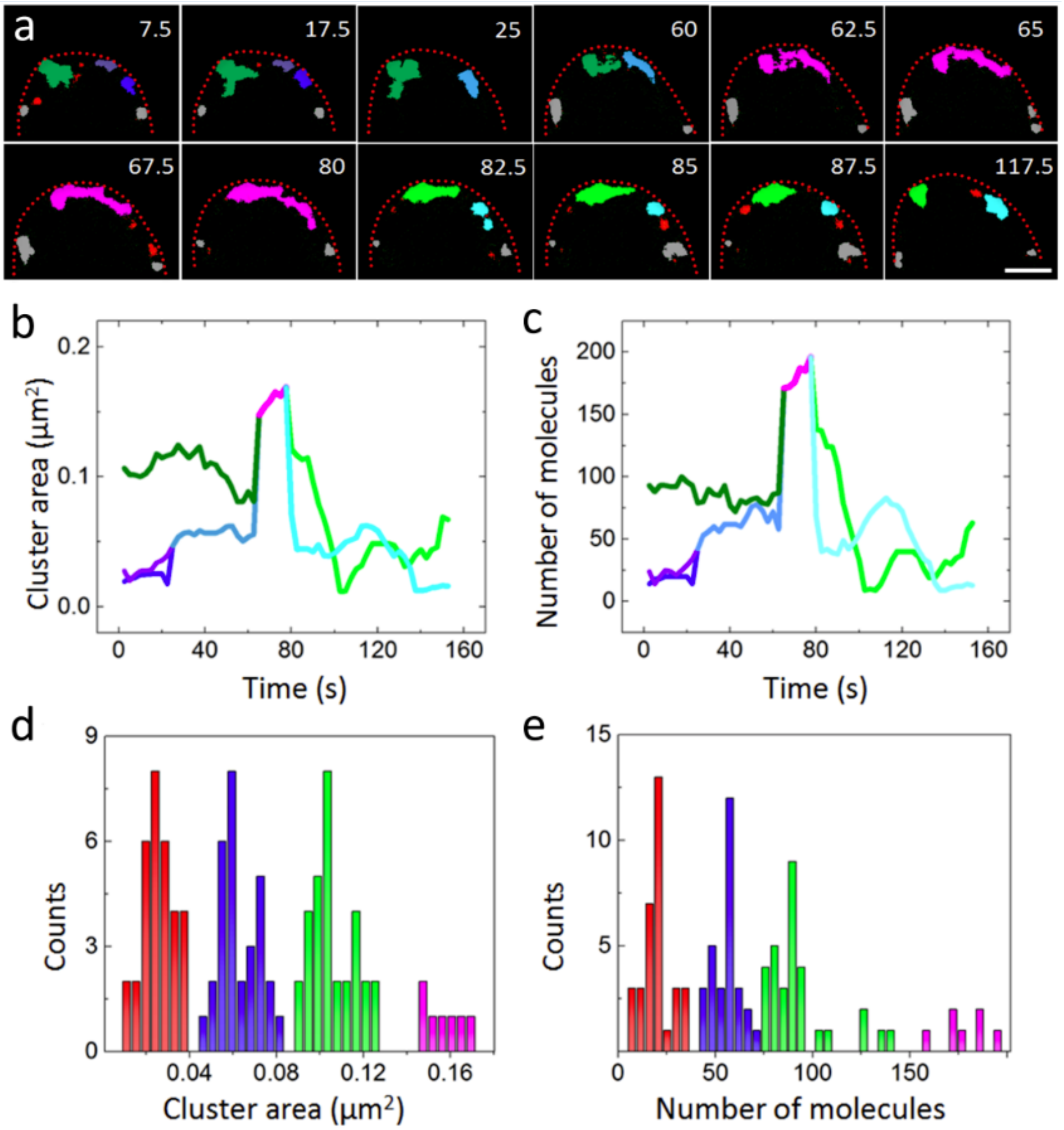

Figure 5.2: Cluster analysis of ChsB clusters in the hyphal tip region. (a) The image sequence of ChsB clusters rendered from PALM images reconstructed by moving-window binning. The elapsed time is given in seconds. (b, c) Time courses of the cluster area (b) and the number of molecules (c). Lines are drawn in the colors corresponding to the clusters in (a). (d, e) Distributions of the cluster area (d) and the number of molecules (e) from all 80 analyzed clusters. Scale bar, 300 nm. Image adopted from reference [126].

We observed that the shapes of the clusters changed from globular to crescent. This shape change may indicate a transition from the accumulation of vesicles before exocytosis to the fusion of vesicles with the apical plasma membrane during exocytosis. As shown in Figure 5.2b and c, the dark green cluster of 0.1 μm^2 containing ~100 molecules was visible from 7.5 – 60 s. Through fusion with other clusters, it grew and evolved into the pink, crescent-shaped cluster of ~0.2 μm^2 containing ~200 molecules, which was visible from 62.5 – 80 s. Subsequently, this cluster split into two smaller ones (~0.05 – 0.1 μm^2, ~50 – 100 molecules), depicted in light green and light blue. During the observation time (125 s), we identified a total of 80 clusters in this hyphal tip. By analyzing the areas and molecule numbers of the clusters (Figure 5.2d,e), we determined four subdistributions of cluster sizes (Figure 5.2d), with average areas of 0.03 ± 0.01 μm^2 (red), 0.06 ± 0.01 μm^2 (blue), 0.11 ± 0.01μm^2 (green) and 0.16 ± 0.01 μm^2 (pink). The overall average was 0.07 ± 0.04 μm^2. The corresponding average numbers of mEosFP*thermo*:ChsB molecules of the clusters registered in the four subdistributions were 20 ± 8 (red), 56 ± 7 (blue), 92 ± 17 (green), and 178 ± 12 (pink), respectively (Figure 5.2e). This observation further reflected evolution of the clusters, including the fusion of small clusters and the splitting of big clusters during growth of the hyphal tip.

We also analyzed the temporal evolution of the hyphal apex from the PALM images with 20 s intervals (Figure 5.3a, b). Apparently, the extension rate of the hyphal tip varied over time. The largest displacements occurred from 50 to 70 s and from 90 to 110 s (Figure 5.3b, asterisks), which corresponded with the major changes of cluster shapes (Figure 5.3a, 50 – 70 s, asterisks) and an apparent reduction of the cluster size (Figure 5.3a, 90 – 110 s, asterisks), respectively. These results suggested that secretory vesicles accumulated at the Spitzenkörper during the slow growth phase. Subsequently, they fused with the plasma membrane and spurred the fast growth. The observation is in agreement with the transient polarity assembly model, which states that the assembly or disassembly of polarity markers and local exocytosis coordinate the growth of fungal cells resulting in local membrane extension [137]. Moreover, we merged the cluster images from the entire time sequence (Figure 5.3c). In addition to the crescent domain along the apical membrane, we also observed two separated sub-apical domains (Figure 5.3c). This result agrees with previous work, which stated that endocytosis mainly occurs in an annular structure around the hyphal tube, spatially separated from the hyphal apex where SVs are delivered for exocytosis [150].

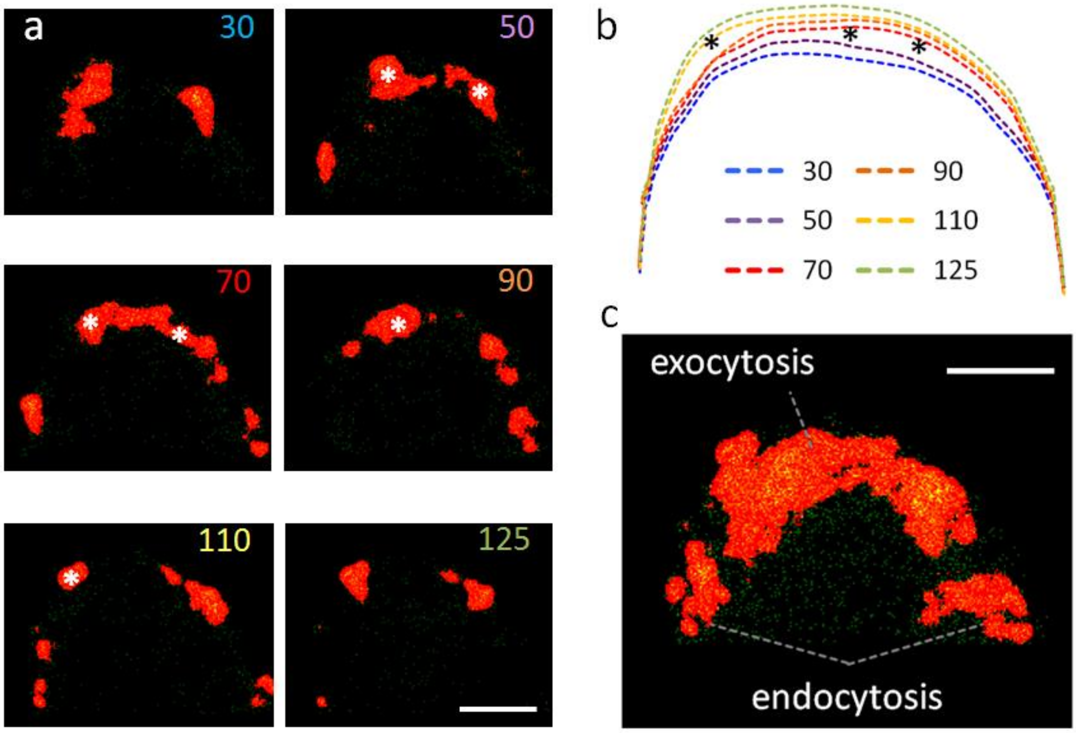

Figure 5.3: Distribution of ChsB clusters in the hyphal tip region during cell growth. (a) The sequence of images from the cluster analysis. The elapsed time is given in second. (b) Overlay of the corresponding tip profiles. Asterisks indicate significant extensions of the apical membrane. (c) Merged image of the image series shown in (a). Scale bars, 300 nm. Image adopted from reference [126].

5.1.2 Pulse-chase analysis of vesicle transport

5.1.2.1 Pulse-chase analysis in wildtype hyphae

Vesicle transport in fungal cells is fundamental to sustaining polar growth. To investigate this process, we employed high-speed pulse-chase imaging of mEosFP*thermo*:ChsB to study the mechanism of the ChsB transport. As described in Section 3.7, a 561 nm laser was first used to photobleach all red-emitting molecules. Subsequently, a spot ~5 µm behind the hyphal tip was irradiated by a tightly focused 405 nm laser beam for 1 s to locally photoconvert mEosFP*thermo*-ChsB to its red-emitting form. As shown in Figure 5.4a, image ‘0’ shows the red fluorescence of mEosFP*thermo* excited by the 405 nm laser, and also shows indicated the local photoconversion spot. After irradiation with a 405 nm laser (Figure 5.4a, image ‘1’), we switched on the 561 nm laser again, and acquired images for 15 – 30 s with a camera dwell time of 50 ms (Figure 5.4a). After photoconversion, the large red emitting spot appeared, gradually faded and finally dispersed, revealing vesicle transport away from the photoconversion region. A kymograph was generated along the axis of the hypha based on the image stacks (Figure 5.4b). By taking advantage of the low background of the pulse-chase imaging technique, we observed both anterograde (from back to tip) and retrograde (from tip to back) vesicle transport in the kymograph (Figure 5.4b). As described in Section 3.7, the transport of vesicles can be visualized in the kymograph by lines (Figure 5.4b, arrows). Typically, the linear vesicle displacements were occasionally interrupted by brief stops (Figure 5.4b, c), and there were also some immobile spots. It was also obvious that the fluorescence from the hyphal tip (Figure 5.4b, blue dashed line) stayed constant beyond ~5 s after photoconversion because of exocytosis of vesicles.

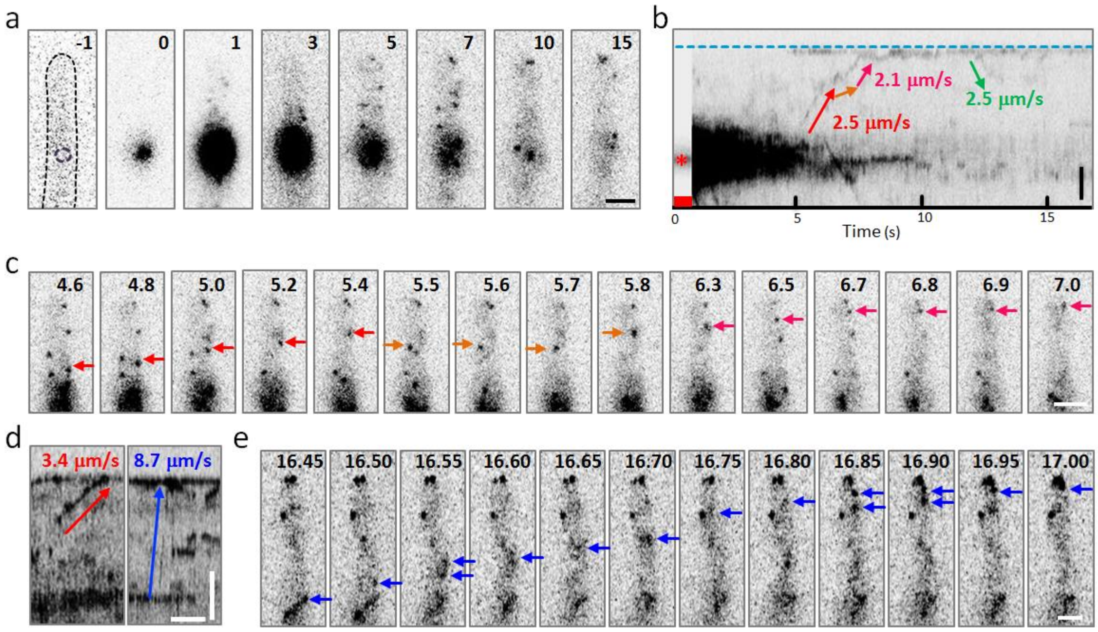

Figure 5.4: Pulse-chase analysis of mEosFP*thermo*:ChsB in the hyphal tip region. (a) Image sequences upon local photoconversion ~5 µm behind the hyphal tip. (b) Kymograph processed from the image sequence shown in (a); the red square indicates the photoconversion interval; the blue dashed line and the red asterisk mark the positions of the hyphal tip and the photoconversion locus; the arrows indicate anterograde and retrograde transports of ChsB, respectively. (c) Image sequence of vesicle transport from 4.6 – 7 s after photoconversion marked by the arrows with colors corresponding to (b). (d) Kymographs of slow (red) and fast (blue) transport of mEosFP*thermo*:ChsB. (e) Image sequence of the fast transport process marked by the blue arrow in (d) observed from 16.45 – 17 s. The elapsed time is given in seconds. Scale bars (a, b, c, d vertical, e) 2 µm. Scale bar (d horizontal), 1 s. Image adopted from reference [126].

The speed of the vesicles can be calculated based on the slopes of the lines in the kymograph. From the observations of a large number of hyphae, most displacements occurred at the speeds of 2 – 4 µm s^{-1}; however, there were also apparently faster transport events with speeds of 7 – 10 µm s^{-1} (Figure 5.4d, e). Accordingly, the speed histogram of anterograde movements appeared to consist of two subdistributions. The predominant distribution was below ~7 µm s^{-1}, associated with the slow transport centered on 3.0 ± 1.0 µm s^{-1} (mean ± SD, n = 42) (Figure 5.5a, b, red). Another smaller distribution was above ~7 µm s^{-1} representing fast transport centered on 8.3 ± 0.7 µm s^{-1} (mean ± SD, n = 7) (Figure 5.5a, b, blue). Retrograde transport was less frequent (15% of events, n = 9) with an average speed of 2.9 ± 0.8 µm s^{-1}, which was identical within the error to that of slow anterograde transport (Figure 5.5b).

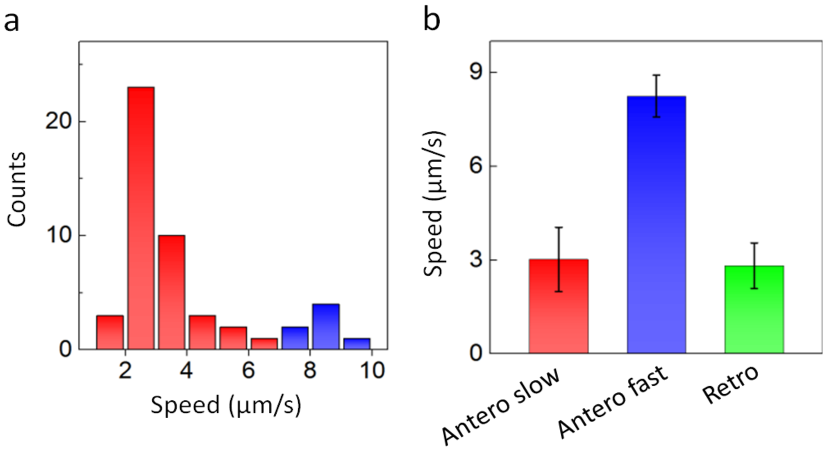

Figure 5.5: Distributions of vesicle transport speeds. (a) Speed distribution of anterograde transports. (b) Speed of anterograde slow (red), anterograde fast (blue) and retrograde (green) transports (mean ± SD, n = 42, 7, 9, respectively). Image adopted from reference [126].

To further investigate the two putative types of transport, the transport speed of GFP:RabA as a marker protein of early endosomes (EEs) was measured [47]. As shown in Figure 5.6a, both anterograde and retrograde movements of vesicles were visible in the kymograph generated along the hyphal axis. The same average speed of anterograde and retrograde transport was 2.0 ± 0.5 µm s^{-1} (mean ± SD, n = 76 and 62, respectively) (Figure 5.6c). Moreover, the pulse-chase experiment was also performed on hyphae expressing mEosFP*thermo*:TeaR (Figure 5.6b), a fusion protein containing the membrane-associated polarity marker TeaR known to be transported on secretory vesicles (SVs) [57, 69]. Significantly, more events of fast transport were observed compared with mEosFP*thermo*:ChsB. The average speed for anterograde movements was 7.9 ± 3.6 µm s^{-1} (mean ± SD, n = 95) and for retrograde movements was 8.3 ± 3.8 µm s^{-1} (mean ± SD, n = 87) (Figure 5.6c). The average speeds of slow transport of mEosFP*thermo*:ChsB and transport of GFP:RabA labeled vesicles, and of fast transport of mEosFP*thermo*:ChsB and mEosFP*thermo*:TeaR labeled vesicles were identical within the error. The histograms of individual events also showed similar distributions (Figure 5.6d). These results strongly suggest that slow and fast transport events of ChsB represent ChsB moving on EEs and SVs, respectively.

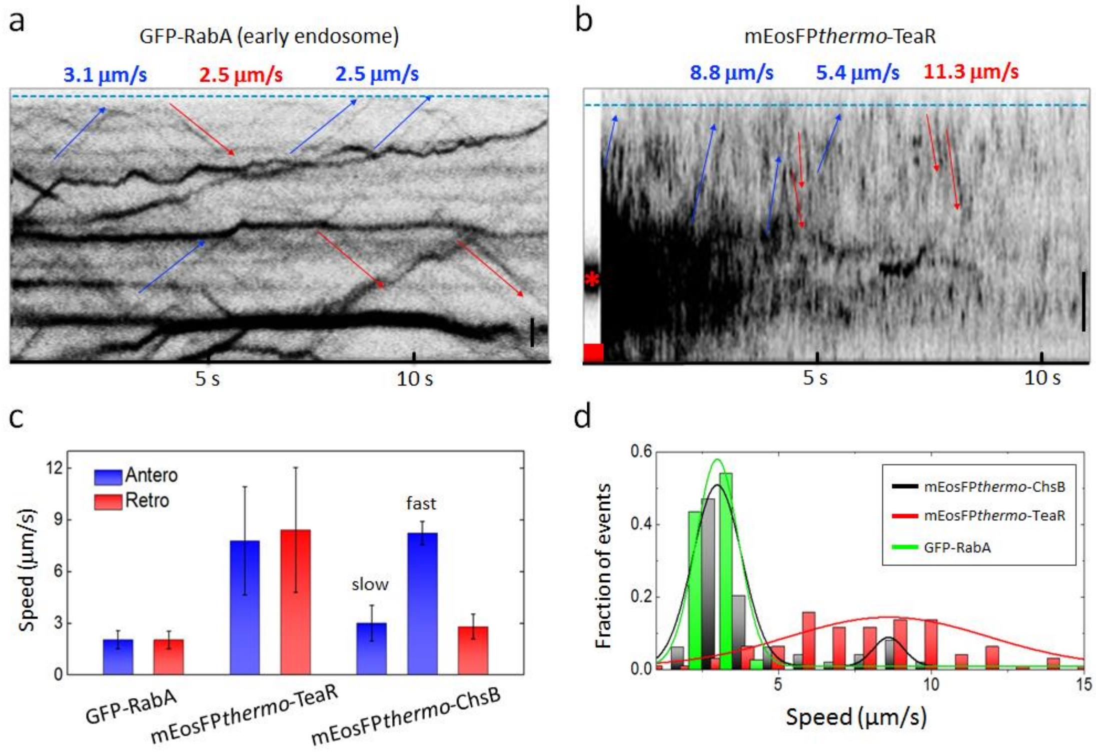

Figure 5.6: Transport speeds of early endosomes and secretory vesicles. (a) Kymograph of RabA:GFP movements. Arrows indicate anterograde (blue) and retrograde (red) transport. (b) Kymograph of mEosFP*thermo*:TeaR movements. Arrows indicate anterograde (blue) and retrograde (red) transport. (c) Speeds of anterograde (blue) and retrograde (red) transport of GFP:RabA, mEosFP*thermo*:TeaR and mEosFP*thermo*:ChsB (mean ± SD). (d) Speed distributions of anterograde transport of GFP:RabA, mEosFP*thermo*:TeaR and mEosFP*thermo*:ChsB. Scale bars (a, b), 2 µm. Image adopted from reference [126].

5.1.2.2 Pulse-chase analysis using microtubule or actin destabilizing drugs

To further investigate the involvement of cytoskeleton components in ChsB transport, pulse-chase experiments were also performed on mEosFP*thermo*-ChsB expressing hyphae treated with either microtubule or F-actin destabilizing drugs. The microtubule-destabilizing drug, benomyl [152], and the F-actin destabilizing drug, cytochalasin A [32], were used at a concentration of 2 µg/ml to treat the cells for 5 – 30 min before imaging. In the presence of benomyl, we observed mostly immobile spots near the photoconversion locus (Figure 5.7a); anterograde and retrograde transport events were rarely visible. In contrast, both anterograde and retrograde transport events were found in the cells treated with cytochalasin A

(Figure 5.7b). The intensity courses at the hyphal tip region and the photoconversion region defined in Figure 5.7c after the photoconversion were plotted (Figure 5.7d, e). The intensity courses from both benomyl and cytochalasin A treated cells showed no accumulation of mEosFP*thermo*-ChsB at the hyphal tips (Figure 5.7d, green and red, respectively), which was significantly different from the control cells (Figure 5.7d, black). Surprisingly, the signal intensity at the photoconversion locus in the benomyl treated cells persisted much longer than in the control and cytochalasin A treated cells. All these results suggest that the transport of SVs depends both on the microtubule and F-actin cytoskeletons. F-actin is especially required at the hyphal tip to accept the SVs transported from microtubules and to guide them to the sites of exocytosis [153].

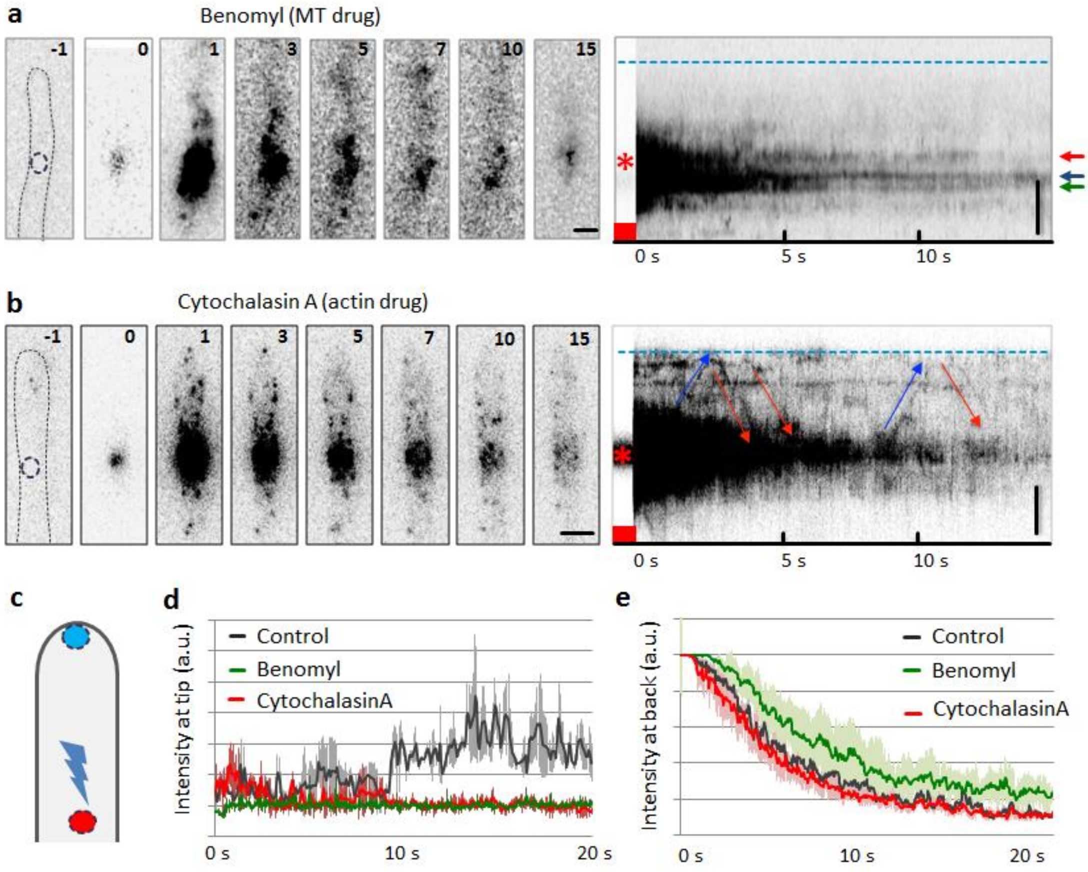

Figure 5.7: Pulse-chase imaging and kymograph analyses of mEosFP*thermo*-ChsB in the presence of microtubule (a) or actin (b) depolymerizing drugs. Image sequences and relative kymographs were acquired upon photoconversion in a spot ~5 µm behind the hyphal tip. The elapsed time is given in seconds. Scale bars, 2 µm. (c) Definition of hyphal tip region (blue) and photoconversion region (red) for the intensity measurements in (d) and (e). (d, e) Fluorescence intensities at the hyphal tip (d) and the photoconversion locus (e) of the control (black), benomyl treated (green) and cytochalasin A (red) treated cells (mean ± SD, n = 3 – 5). Image adopted from reference [126].

5.1.2.3 Pulse-chase analysis using kinesin-1, kinesin-3 and myosin-5 deletion strains

We also performed pulse-chase experiments and kymograph analyses with the kinA (kinesin-1), uncA (kinesin-3) or myoV (myosin-5) deletion strains to further understand the involvement of specific motor proteins in the ChsB transport (Figure 5.8a, b, c). We also measured the intensity courses after photoconversion at two different loci: the hyphal tip regions (Figure 5.8d) and the photoconversion regions at ~5 µm behind the hyphal tip (Figure 5.8e).

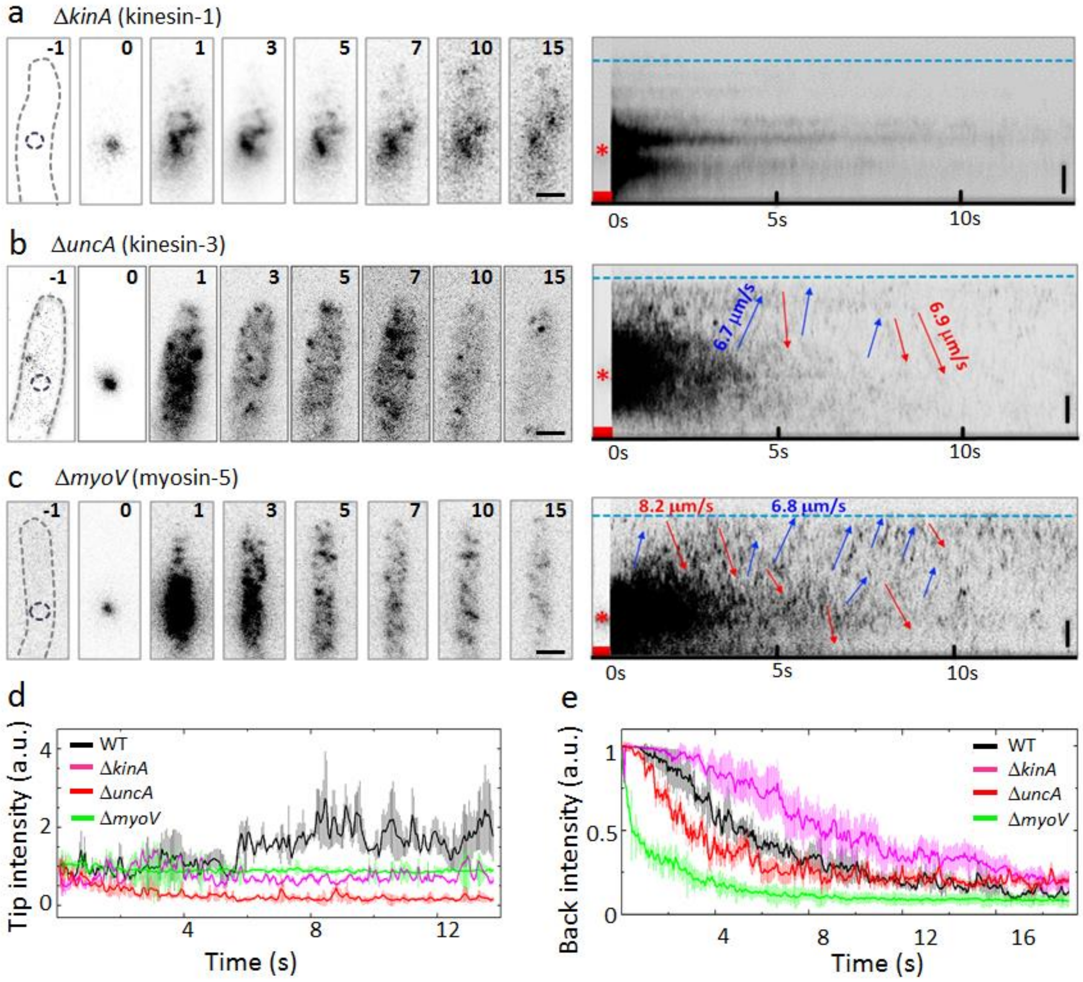

Figure 5.8: Pulse-chase imaging and kymograph analyses of mEosFP*thermo*-ChsB in the cells of kinA (a), uncA (b) and myoV (c) deletion strains. Image sequences and kymographs were acquired upon photoconversion in a spot ~5 µm behind the hyphal tip. The elapsed time is given in seconds. Arrows indicate anterograde (blue) and retrograde (red) transport. Vertical scale bars, 2 µm. (d, e) Fluorescence intensity at the hyphal tip (d) and the photoconversion locus (e) of the control (black), Δ*kinA* (pink), Δ*uncA* (red) and Δ*myoV* (green) cells (mean ± SD, n = 3 – 5). Image adopted from reference [126].

In the kinA deletion strain, neither transport nor signal accumulation at the hyphal tip can be observed after photoconversion, whereas some vesicles remained immobile, as in the benomyl treated cells (Figure 5.8a, d). These results support the common view that kinesin-1 transports SVs over long distances along microtubules to hyphal tips [32, 152].

In the uncA deletion strain, the fluorescent signal spread markedly faster than in the wildtype cells after photoconversion (Figure 5.8b). Interestingly, we also observed that some spots reached the hyphal tip and immediately reverted. Therefore, no accumulation at the hyphal tip was observed (Figure 5.8d). Because kinesin-3 transports EEs [43, 153], absence of slow transport in the uncA-deletion strain further strengthens our assignment that the fast and slow transport events of ChsB correspond to the movement on SVs and EEs, respectively.

Myosin-5 is known to transport SVs along actinfibers for exocytosis at the hyphal tip region [35, 37, 54]. Thus, the myoV deletion strain showed severe growth defects. After photoconversion, we observed faster spreading of the fluorescence signal than in the wildtype cells, which was very similar to the uncA deletion strain (Figure 5.8c). Moreover, the traces of vesicle transport in the kymographs were analogous to the cytochalasin A treated cells. The traces apparently showed that the spots reaching the hyphal tip moved backward immediately, instead of accumulating there. Hence, there was no intensity increase at the hyphal tip, which was significantly different from the control cells. These results suggest that both myoV and actin cables are necessary for capturing SVs from microtubules and further transport them to hyphal tips.

We also analyzed the transport speeds of vesicles from both uncA deletion and myoV deletion strains. It was evident that the fast transport events in both directions were more frequently observed in the kymographs in comparison to the wildtype cells (Figure 5.9a). For uncA deletion cells, the average transport speeds were 8.3 ± 2.0 µm s^{-1} for the anterograde (mean ± SD, n = 44) and 8.6 ± 3.1 µm s^{-1} for the retrograde movements (mean ± SD, n = 51) (Figure 5.9b). The average speeds for the myoV deletion cells were 7.2 ± 2.9 µm s^{-1} for the anterograde (mean ± SD, n = 46) and 5.9 ± 2.6 µm s^{-1} for the retrograde movements (mean ± SD, n = 38) (Figure 5.9b). These values are identical within the error to the speed of the fast transport in the wildtype cells. By analyzing the fraction of transport speed events (Figure 5.9c), the speed distributions in both uncA and myoV deletion cells were similar to that of the fast transport in the wildtype cells.

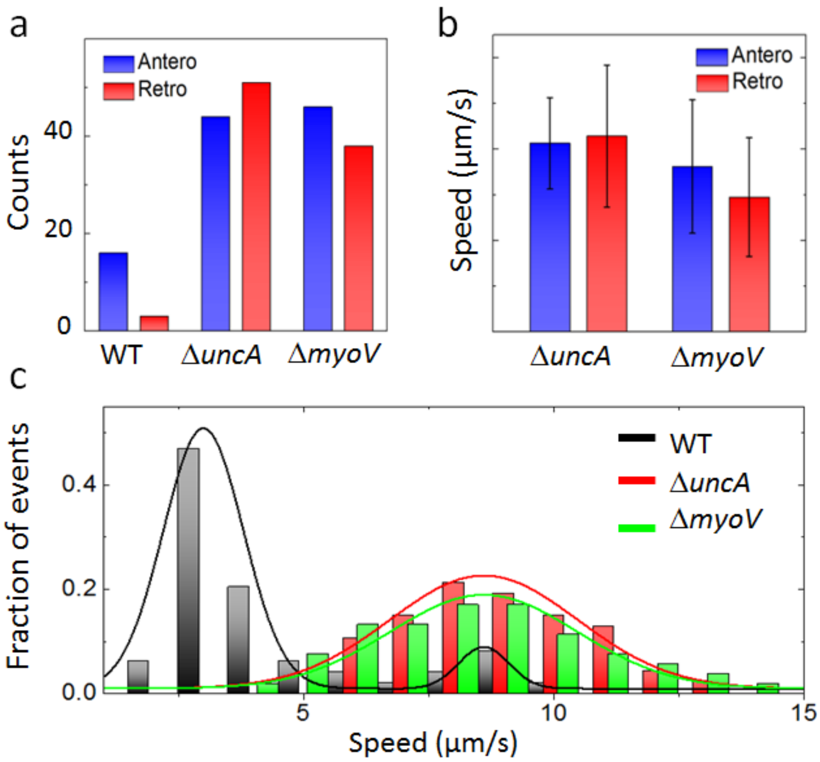

Figure 5.9: Analyses of transport speeds in uncA and myoV deletion strains. (a) Numbers of anterograde (blue) and retrograde (red) transport events in wildtype, ΔuncA, and ΔmyoV cells, respectively. Six cells were measured for each strain. (b) Speed of anterograde (blue) and retrograde (red) transport in ΔuncA and ΔmyoV cells (mean ± SD). (c) Speed distribution of anterograde transport from wildtype (black), ΔuncA (red), and ΔmyoV (green) cells. Image adopted from reference [126].

To compare the number of photoconverted proteins in Figure 5.8a, we performed a quantitative intensity analysis of the different strains, focusing on the first frame after photoconversion (at 1 s). In Figure 5.10a, we marked the regions in which the local intensities were determined with red ellipses. Importantly, all analyzed images were acquired with similar power of the 405 nm laser (photoconversion) and 561 nm laser (fluorescence excitation). The background was subtracted from the local intensity of each image using ImageJ. For each cell strain, images of five individual cells were analyzed and the local intensities (camera A/D counts) were averaged (Figure 5.10b, left axis). Since all measured data were acquired with the same camera settings for imaging, we can convert the local intensity value (A/D count) to the local molecule number. With our a-livePALM software, the photon number of single emitters can be precisely determined. However, because vesicles typically carry multiple mEosFPthermo-ChsB molecules (Figure 5.10c, red spots), the challenge is how to obtain photon numbers of single fluorophores. To this end, we selectively analyzed the last few frames from single vesicles before complete photobleaching, which are likely to contain only a single fluorescing mEosFPthermo-ChsB molecule (Figure 5.10c). The very final frame contains variable photon numbers because it is unclear at which point during the 50 ms camera exposure time the mEosFPthermo photobleaches. Therefore, we analyzed the fluorescence from the penultimate frame of individual vesicles. To be even further on the safe side, we selected only those vesicles that can be observed in at least three continuous frames.

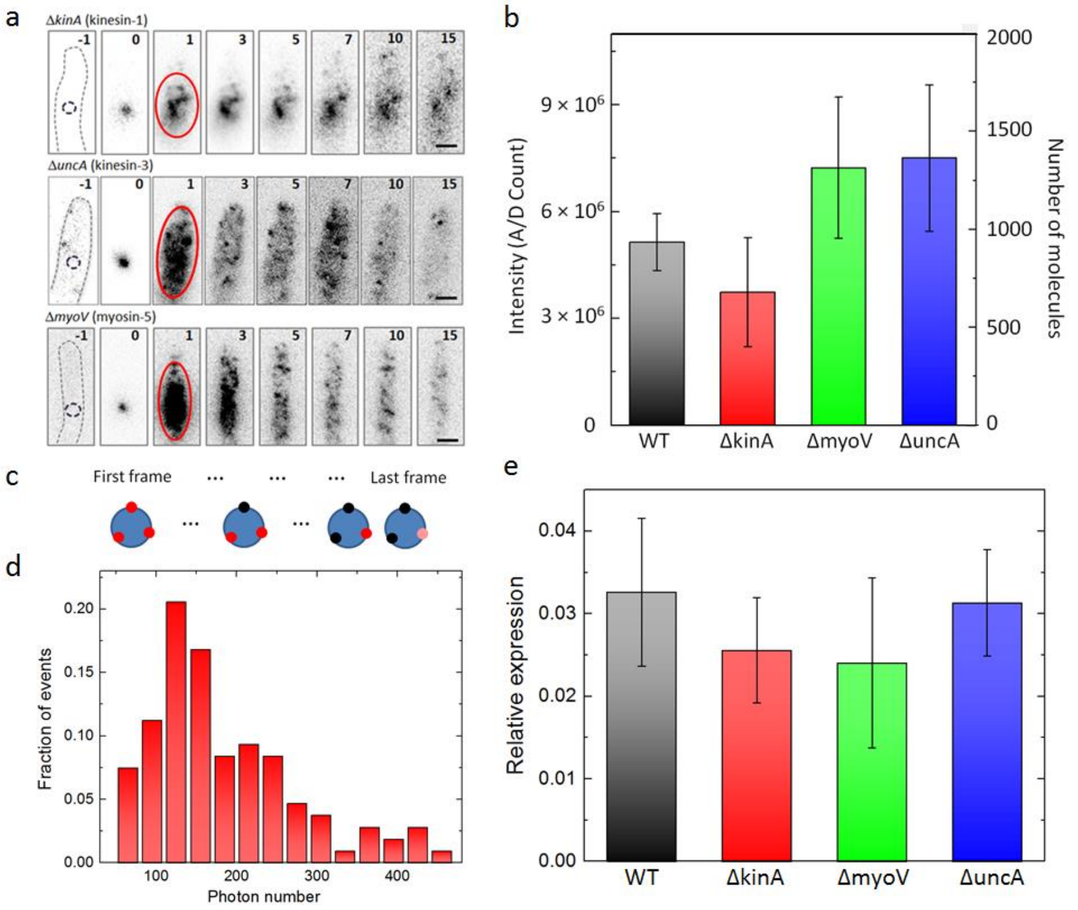

Figure 5.10: (a, b) Intensity-based counting of red-converted fluorescent protein molecules. (a) Selected image sequences of hyphal tips before, during and after photoconversion; quantitative analysis was based on the intensities within the local regions marked by red ellipses. (b) Local intensity (left axis) and number of molecules (right axis) for the different cell strains. (c) Schematic of the approach used for detecting single fluorophores: Fluorescent proteins (mEosFPthermo) on the same vesicle were gradually bleached, resulting in the detection of single-molecule emission in the last few frames. (d) Distribution of photon numbers from individual mEosFPthermo molecules as measured on wildtype cells. (e) Relative expression levels of ChsB in the wildtype strain and the motor deletion strains measured by qRT-PCR. Image adopted from reference [126].

The analysis was done with wildtype cells, for which vesicle transport is slower than for the other strains, so they are more easily tracked. We analyzed the images from 30 – 45 s (frames 600 – 900) after photoconversion because most of the mEosFP*thermo* molecules are already bleached in this time interval, leading to a high probability to observe only emission from vesicles containing a single mEosFP*thermo* fluorophore. With a total of 107 events detected from three wildtype cells, we obtained an average number of photons of 184 ± 92 (SD) per molecule; the distribution of photon numbers is shown in Figure 5.10d. The system readout rate and the EM gain of our camera were set to 10 MHz and 150, respectively. With this readout rate, the EMCCD sensitivity (electrons per A/D count) is 4.61, as given by the camera datasheet. With the average photon number per molecule calculated above, we can convert the intensity value (Figure 5.10b, left vertical axis) to the number of molecules (Figure 5.10b, right vertical axis). Typically, 500 – 1500 molecules were locally photoconverted by 1 s exposure to the 405 nm laser spot. In the uncA-deletion and myoV-deletion strains, the number of locally photoconverted mEosFP*thermo*-ChsB in the pulse-chase experiments is increased by 46 % and 40 % with respect to the wildtype (Figure 5.10b). Two reasons may explain this phenomenon: (1) difference in the expression level; (2) different degrees of diffusion during photoconversion (1 s), leading to the partial escape of molecules from the region that was analyzed.

To quantitatively analyze the expression levels of different cell strains, my collaboration partner Valentin Wernet employed the quantitative real-time PCR (qRT-PCR). The qRT-PCR was performed using SensiFASt SYBR and Fluorescein One-Step kit (Bioline, London, UK). Each reaction was carried out with 0.2 µM primer and 100 ng RNA in a total volume of 25 µl. For normalization of the expression, the histone 2b gene was used, and each reported expression level was averaged over three biological and technical replicates. As shown in Figure 5.10e, the expression levels of ChsB among the strains are of comparable magnitude within the error. Therefore, the difference in the numbers of photoconverted molecules (Figure 5.10b) may reflect different degrees of escape from the observation volume during photoconversion.

5.1.2.4 Pulse-chase analysis with photoconversion at the hyphal tip

We performed the same pulse-chase experiments with photoconversion at the hyphal tip region on wildtype, benomyl or cytochalasin A treated, and uncA-deleted hyphae, respectively.

For the wildtype cell, a large spot appeared at the hyphal tip right after photoconversion. Subsequently, the spot gradually shrank and dispersed at the hyphal tip, accompanied by vesicles moving away (Figure 5.11a).

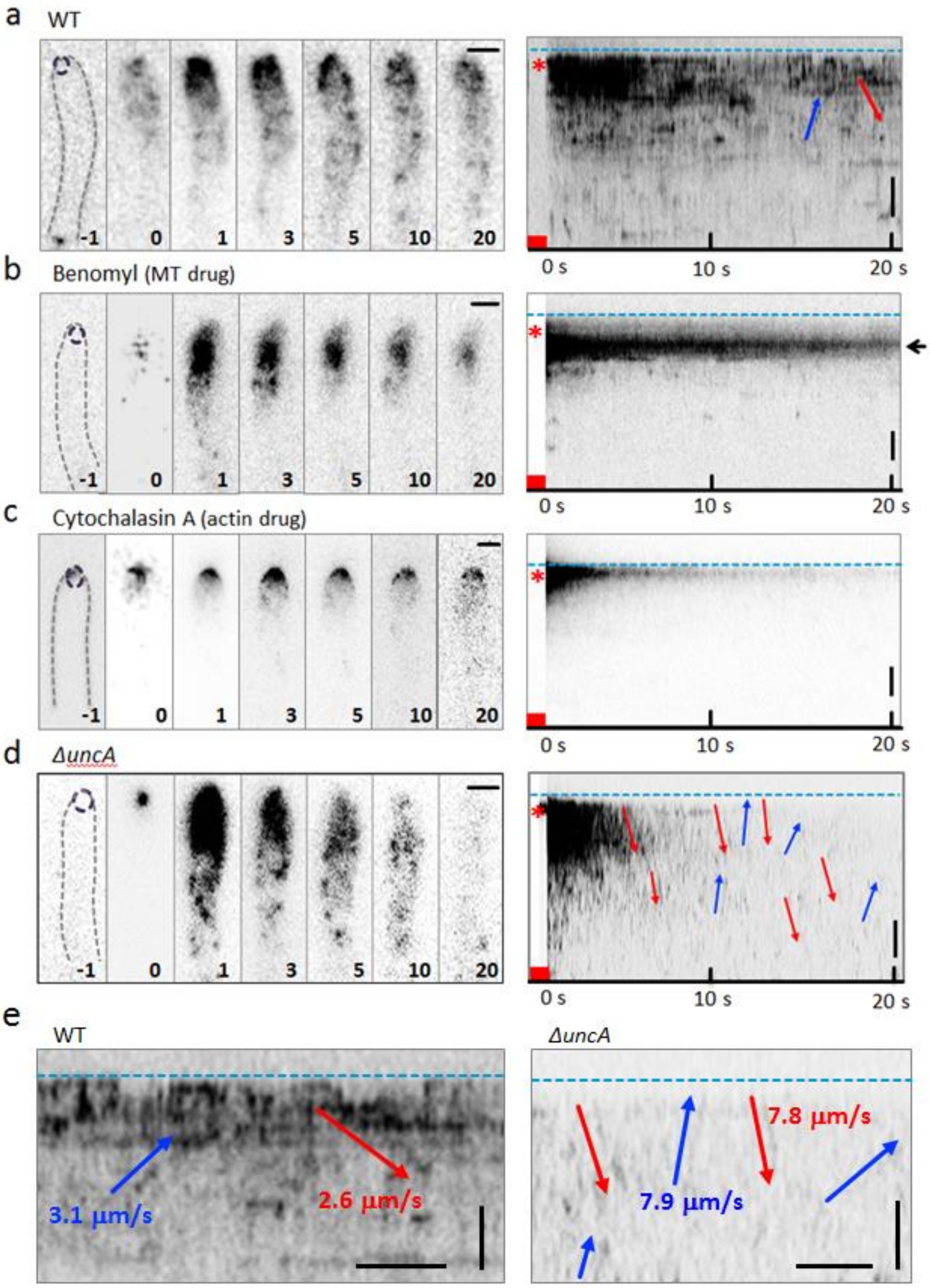

Figure 5.11: Pulse-chase analyses after mEosFP*thermo*-ChsB photoconversion at the hyphal tip. (a-d) Left: Image sequences upon photoconversion at the hyphal tip from a wildtype cell without drugs (a), in the presence of benomyl (b) or cytochalasin A (c), and a cell from the uncA-deletion strain (d). The elapsed time is given in seconds. Right: corresponding kymographs; (e) Enlarged kymographs of wildtype (left) and ΔuncA (right) cells. Arrows show anterograde (blue) and retrograde (red) transport events. Vertical and horizontal scale bars, 2 µm and 1 s. Image adopted from reference [126].

We observed both anterograde and retrograde transport events in the kymograph (Figure 5.11a, e). Statistical analyses showed that 40% of the transport events were anterograde and 60% retrograde, and both had average speeds of ~2 – 3 µm s^{-1} (mean ± SD, n = 42). The average speed was identical to the slow speed of EEs, which was observed in the pulse-chase experiments with photoconversion at the hyphal body region. These results suggest the transport events from the wildtype cell in Figure 5.11a were movements of EEs along microtubules.

For both benomyl (2 µg/ml) and cytochalasin A (2 µg/ml) treated cells (5 – 30 min prior to imaging), transport events were hardly detected. However, localization of ChsB showed a significant difference in benomyl and cytochalasin A treated cells. For benomyl treated cells, ChsB was found near the hyphal tip but not at the apical membrane (Figure 5.11b). Differently, in cytochalasin A treated cells, ChsB localized exactly at the apical membrane (Figure 5.11c). This observation indicates that an intact actin cytoskeleton is crucial for ChsB endocytosis and its transport away from the apical membrane region. Microtubules are dispensable for the endocytosis of ChsB but are necessary for its further transport away from the hyphal tip region.

In the uncA-deletion strain, the ChsB fluorescence spreads faster from the hyphal tip than in the wildtype (Figure 5.11d). As shown in Figure 5.11e (right), both anterograde and retrograde transport events were observed with the average speeds of 8.0 ± 1.8 µm s^{-1} and 7.7 ± 2.4 µm s^{-1} (mean ± SD, n = 41 and 43), respectively. These fast speeds suggest that ChsB in the uncA-deletion strain is transported in both directions mainly on SVs along the microtubules.

5.1.3 Discussion

Cell-wall synthesis at the hyphal tip is essential for cell extension. We employed super-resolution microscopy and pulse-chase imaging to elucidate the transport mechanism of ChsB, a cell-wall-synthesizing enzyme, to the hyphal tips. The supply of SVs carrying ChsB along the apical membrane does not occur in a steady but in a clustered fashion. The Spitzenkörper is constructed by fusion of such clusters. It has been observed that the polarity marker TeaR forms transient local hot spots along the apical membrane [137]. In this work, by using the super-resolution PALM imaging technique and cluster analysis, we clearly observed characteristic shape changes of the Spitzenkörper from globular to crescent. This regular change indicats the membrane extension for cell polar growth. Apparently, SVs accumulate at the Spitzenkörper during phases of slow growth followed by fusion with the plasma membrane, generating bursts of fast growth. Afterwards, the material is consumed and needs to be replenished. These findings support the model of transient polarity assembly for polar growth of fungal cells [137]. Moreover, it was also recently reported that the pulsatory Ca^{2+} influx controls actin polymerization and exocytosis, resulting in stepwise cell extension [154]. This typical stepwise growth may enable cells to respond more rapidly to chemical or mechanical cues.

We also studied the dynamics of ChsB transport by employing a high-speed pulse-chase experiment. Surprisingly, two different speed ranges of ChsB transport events, below and above ~7 µm s^{-1}, were found from the quantitative analysis. By omparison with the transport of EE and SV markers, fast and slow speeds can be unambiguously assigned to transport of ChsB associated with EEs and SVs, respectively. It is the first time that transport of SVs with the fast speed of ~7 – 10 µm s^{-1} was directly observed in filamentous fungi. In fungi, EEs are 4 – 5 times larger than SVs [154, 155]. The faster transport of SVs is probably because of the size effect of the cargo. Of note, in cultured mammalian cells, the speeds of kinesin-1 and kinesin-3 are similar, ~1 – 2 µm s^{-1} [156]. Based on this work, we propose a schematic depiction of the ChsB transport mechanism as shown in Figure 5.12.

From the pulse-chase experiments involving cytoskeleton-destroying drugs, we conclude that ChsB molecules are transported on microtubules to the hyphal tip, where actin cables further transport them to the sites of exocytosis [153]. By using hyphal strains with deletion of different motor proteins, markedly different growth of wildtype, ΔkinA, ΔuncA and ΔmyoV strains was observed (Figure 5.12a). In this work, high-speed pulse-chase experiments were employed to study the essential role of these motor proteins in the polar growth of hyphae.

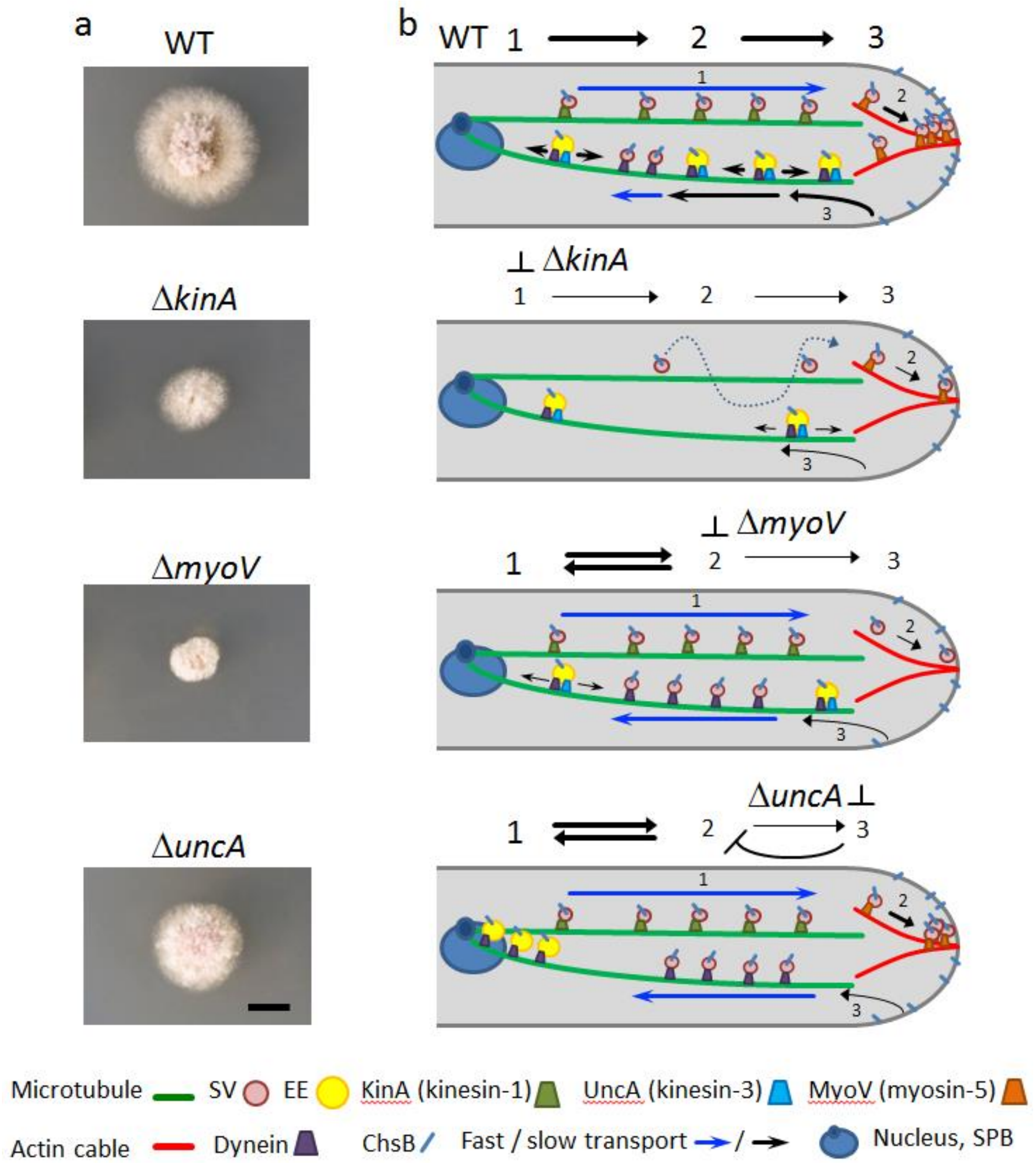

Figure 5.12: Images of fungal colonies and schematic depictions of ChsB transport in wildtype, ΔkinA, ΔmyoV and ΔuncA strains. (a) Images taken on the same spatial scale; scale bar, 5 mm. Strains were grown on the same minimal medium glucose agar plate for two days. (b) Depictions of ChsB transport processes in the four strains as discussed in the text. The symbol legend is included below. Image adopted from reference [126].

Kinesin-1 is required for transport of SVs over long distances along microtubules to hyphal tips, which was proved with the kinA (kinesin-1) deletion strain [54]. As shown in Figure 5.12, without kinesin-1, the active transport of SVs ceases. Only free diffusion of SVs can be observed, and polar growth of hyphae is strongly impaired.

Myosin-5 is known to move along actin cables and transport SVs to the sites of exocytosis [40]. In our observation, the myoV (myosin-5) deletion strains showed fast transport of ChsB in both directions but no signal accumulation at the hyphal tip. Without actin cables or myosin-5, SVs cannot be captured at the hyphal tip region for further transport. Instead, SVs reaching the tip region immediately reflected, resulting in circular transport of SVs in both directions, as with a microtubule-based conveyor belt (Figure 5.12b) [153]. The impaired exocytosis leads to severe growth defects, as shown in Figure 5.12a. Of note, only a small fraction of ChsB transport on EEs after endocytosis can be observed because ChsB can hardly reach the hyphal tip without myosin-5.

In the uncA (kinesin-3) deletion strain, ChsB was transported at high speed bi-directionally. Because kinesin-3 transports EEs along microtubules [43, 124, 153], the absence of slow movement in the uncA-deletion strain indicates that ChsB is transported predominantly on fast-moving SVs by kinesin-1 (Figure 5.12b). Even though myosin-5 is present, no accumulation at the hyphal tip can be observed, which means SVs are not captured for exocytosis. This surprising result may be explained in the following way. In the vesicle recycling pathway, kinesin-3 and dynein are assumed to transport EEs bi-directionally along microtubules. Therefore, this transport branch is severely suppressed because of the deletion of kinesin-3, resulting in the machinery becoming clogged with EEs blocked at the end of microtubules. Because the balance of exocytosis and endocytosis is essential to regulate the supply of SVs for exocytosis, the putative defect of endocytosis in the kinesin-3 deletion strains might affect exocytosis and lead to circular transport of secretory vesicles. This assumption is supported by the lower growth rate of the kinesin-3 deletion strains compared with the wildtype, but it is still higher than that of the kinesin-1 or myosin-5 deletion strains (Figure 5.12a).

In summary, by using the PALM technique and the pulse-chase experiment, the fundamental molecular mechanisms of materials transport during fungal tip growth were well elucidated. With these techniques, the vesicle transport can be visualized with extremely low background fluorescence, which offers a prominent method to study vesicle dynamics quantitatively. The essential roles of motor proteins kinesin-1, kinesin-3, myosin-5 in vesicle transport for the polar growth of *A. nidulans* were also well explained. These new insights will be beneficial for the development of fungal-based biotechnology applications in fields such as agriculture, pharmacology, food science and medicine.

5.2 Investigation of Num1 protein in *Ustilago maydis*

5.2.1 PALM imaging of Num1

To study the fundamental mechanisms of the Num1 protein in *Ustilago maydis* (*U. maydis*), fusion proteins of Num1 with fluorescent proteins were needed to visualize the Num1 in live cells. In the previous study, the Num1 was fused with GFP and the cytoplasmic signals from the fusion protein were detected with conventional fluorescence microscopy [48]. However, the signal of the fusion protein was too weak to assign any specific cellular structure. By using the PALM technique, the imaging sensitivity and the capability of localizing the emitters can be dramatically improved. To this end, my collaboration partner Dr. Theresa Obhof constructed the fusion proteins of Num1 with both mEos2 and tdEosFP and they were tested in this work (See Section 3.1.3.2).

The two fusion proteins Num1:mEos2 and Num1:tdEosFP were first tested with a spinning-disk confocal microscopy and the PALM setup. In acquired images, Num1:tdEosFP appeared significantly brighter than Num1:mEos2 within the green channel (Figure 5.13a, left). The images were taken with irradiation by a 488 nm laser and detection with a 525/50 nm (peak wavelength/width) bandpass filter to visualize the green species of EosFPs. The PALM setup was also used to localize Num1:mEos2 or Num1:tdEosFP in AB31 sporidia, respectively. Raw images were acquired with 561 nm laser excitation and additional weak 405 nm laser irradiation for continuous green-to-red photoconversion of the fluorescent proteins and the emission was filtered with a 607/70 nm band-pass filter. PALM images were rendered from 1000 raw frames with a photon number threshold of 100 for collecting fluorescence events (Figure 5.13a, right). In both strains, as expected, the main signal was from the nuclear region. Clear signals, however, were also visible from the cytoplasm (Figure 5.13a, right), indicating a dispersed cytoplasmic localization of Num1. Both the number of detected fluorescence events as well as the detected photon numbers per event were much higher in sporidia expressing Num1:tdEosFP than in those expressing Num1:mEos2. The histograms in Figure 5.13b display the number of localization events as a function of the registered photons per frame for each event. For Num1:mEos2, the average number of photons from 192 detected fluorescence events was 198. For Num1:tdEosFP, however, the number of detected fluorescence events significantly increased to 965 with a higher average photon number of 236. These data underscore that tdEosFP is much superior to mEos2 for super-resolution imaging of Num1.

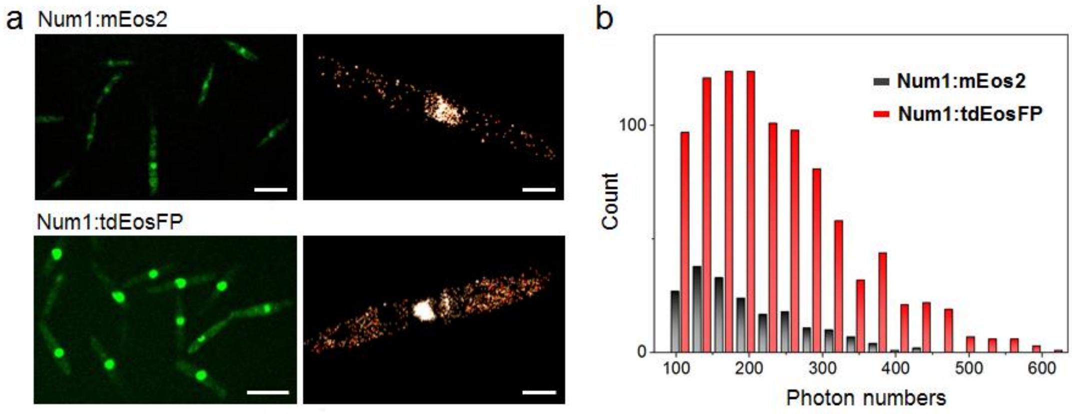

Figure 5.13: Comparison between Num1:mEos2 and Num1:tdEosFP. (a) *U. maydis* AB31 sporidia expressing Num1:mEos2 (upper panels) and Num1:tdEosFP (lower panels) were imaged with a spinning disk confocal microscopy (left) and PALM (right). Both PALM images were reconstructed from 1000 raw camera frames, using a photon number threshold of 100. Scale bars: 10 µm (left), 2 µm (right). (b) Photon number distributions of fluorescence events collected from the cytoplasmic regions of the two cells from (a), showing the number of fluorescence events as a function of the registered photons per frame for each event.

The localization precision of a fluorophore scales roughly with the inverse square root of the number of photons collected during exposure. Effects such as fluorophore movement or a slight defocus may lead to lower photon numbers obtained from an individual molecule and, therefore, less accurate localization. Such events can be excluded by setting a proper photon threshold, below which the events are discarded. Hence, using a higher photon number threshold in image reconstruction leads to a smaller number of events but selective inclusion of more precise localized events. Consequently, the image quality improves as long as the number of localization events is still sufficient for image reconstruction. In Figure 5.14, PALM images were reconstructed with the same raw data, but different photon number thresholds of 100 to 300. Under these more stringent conditions, the Num1:tdEosFP protein still showed dispersed distribution over the entire cytoplasm.

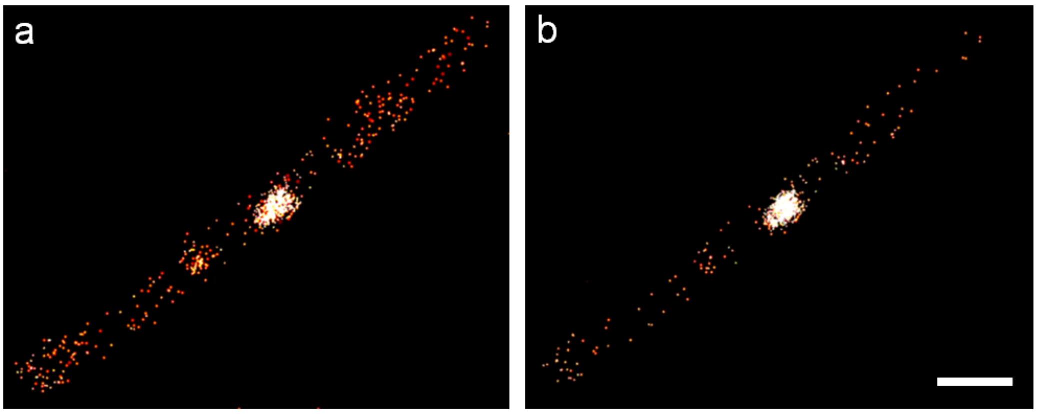

Figure 5.14: PALM super-resolution images of an AB31 sporidium expressing Num1:tdEosFP. The images were rendered from the same raw data, with photon number threshold set to 100 (a) and 300 (b). Scale bar, 2 µm.

Num1 was proven to interact with the microtubule-associated motor protein kinesin-1, and deletion of Num1 affects the movement of early endosomes, which are transported via a microtubule-dependent machinery [48]. These findings suggest that Num1 might be associated with either microtubules and/or early endosomes. To address a possible relationship between Num1 and the microtubule cytoskeleton, we expressed a GFP:Tub1 fusion protein [157] in AB31 num1:tdEosFP to visualize microtubules. Cells were sequentially imaged in the green (GFP:Tub1) and red channel (num1:tdEosFP). Molecule localizations of Num1:tdEosFP were collected and rendered to yield the super-resolved localization image overlaid with the regular image from the green channel of GFP:Tub1. Of note, the amount of cytosolic Num1 is extremely low. Therefore, the green emission from tdEosFP has no influence on imaging of GFP:Tub1 in the cytosol.

Num1:tdEosFP showed a partial colocalization to the microtubules in AB31 sporidia (Figure 5.15a). However, the tdEosFP signals were also visible in regions distinct from microtubules. To quantitatively analyze the colocalization of Num1 with microtubules, we calculated the density of Num1:tdEosFP (1) in the microtubule region and (2) the cytoplasmic region of the entire cell. Based on the microtubule images in the green channel, lines were drawn by hand to trace the microtubules, and the microtubule region was defined as locations closer than 300 nm (12 pixels with 25 nm pixel size) to the center of the lines (Figure 5.15b, middle). The ±300 nm tolerance was chosen to account for possible movements of microtubules during imaging in the red channel (1000 frames, 50 s). As a comparison, we also calculated the density of Num1:tdEosFP localization events for the whole cytoplasmic region, i.e., the entire cell without the nuclear region (Figure 5.15b, right). Averaged over nine cells, we obtained molecule density of 6.5 ± 0.8 μm^{-2} for the microtubule region, which is significantly greater than the value of 4.5

± 1.1 μm^{-2} for the cytoplasmic region (Student's t-test, $p < 0.0005$) (Figure 5.15c). This quantitative analysis supports the notion that Num1 is partially colocalized with microtubules rather than freely diffusing in the cytoplasm.

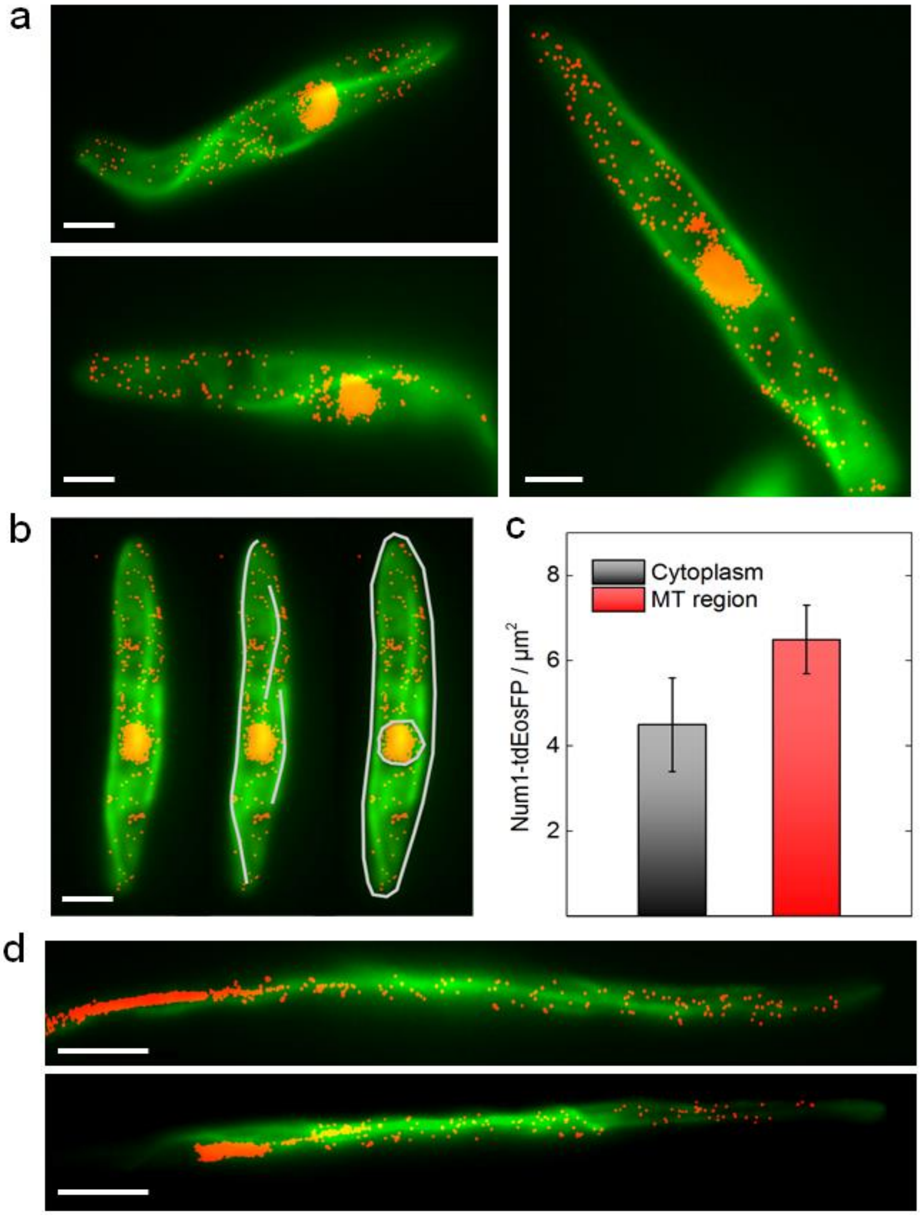

Figure 5.15: Elevated Num1 localization in the vicinity of microtubules. (a) Two-channel images of AB31 sporidia, with the microtubule structure (GFP:Tub1) (green) and individual Num1:tdEosFP proteins (orange spots). Scale bar: 2 µm. (b) Illustration how the image (left) was processed to define microtubule (middle) and cytoplasmic regions (right) for Num1:tdEosFP density calculations given in (c); signals from the nuclear region were excluded in these calculations. (c) Densities of Num1:tdEosFP molecules in the cytoplasm and the microtubule regions depicted in (b) (mean ± SD, n = 9). (d) Two-channel images of AB31 filamentous cells expressing GFP:Tub1 and Num1:tdEosFP.

To address the localization of Num1 in filamentous cells, we incubated the AB31 strain in the arabinose-containing medium for 6 h before imaging. The resulting hyphae showed no distinct phenotype concerning the morphology, septum formation or nuclear distribution, as described previously for *num1* gene deletion-strains [48]. These observations suggested that the Num1:tdEosFP fusion protein was functional in filamentous cells. As shown in Figure 5.15d, similar to sporidia, the primary signal of Num1:tdEosFP resided within the nucleus which appears as a stretched, extended structure in *U. maydis* hyphae [48]. Close to the nucleus, Num1:tdEosFP showed remarkable linear distributions and colocalized with microtubules (Figure 5.15d). Of note, similar to the observations in sporidia, there were also additional signals independent from microtubules.

It has been shown that the deletion of Num1 affects the movement of early endosomes [48]. We addressed a potential colocalization of Num1 with these vesicles. Early endosomes were labeled with a GFP:Rab5a fusion protein that has been used successfully as a specific marker for early endosomes [158]. To exclude the influence of vesicle movement in living cells during the imaging process, we used fixed cells (8% formaldehyde) to check the colocalization precisely. As shown in Figure 5.16a, GFP:Rab5a labeled early endosomes distributed throughout the cytoplasm. The frequently observed linear array of their localization was because of their microtubule association. However, no apparent colocalization between the GFP:Rab5a and Num1:tdEosFP signals can be observed, indicating that Num1 does not localize to early endosomes.

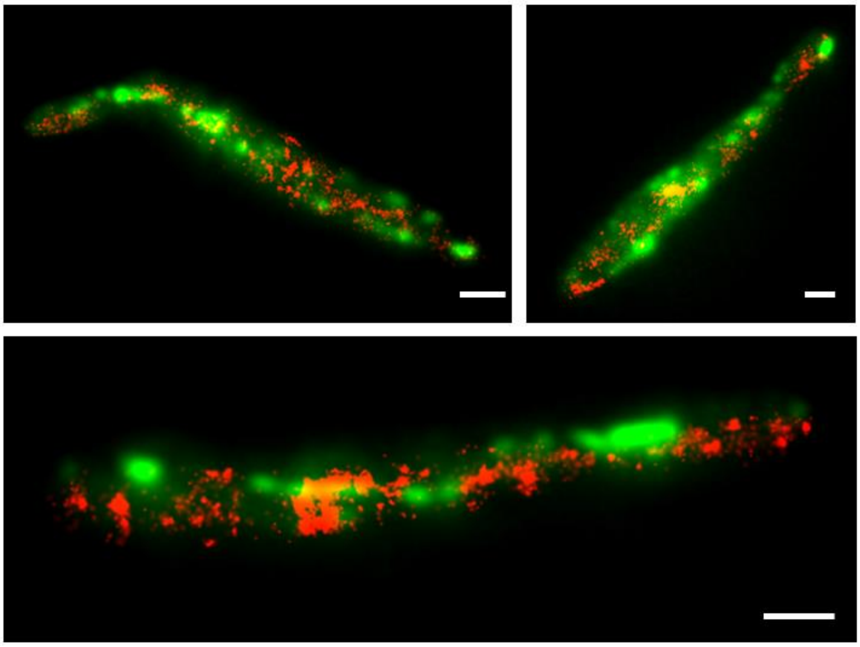

Figure 5.16: Num1 is not associated with early endosomes. The widefield image of GFP:Rab5 (green) is overlaid with the PALM image of Num1:tdEosFP (red). Scale bars, 2 µm.

5.2.2 Mechanisms of Num1 transport

To investigate the transport of the Num1 protein within the cytoplasm, kymographs were generated along a straight line tracing the long axis of the cells. As shown in Figure 5.17a (upper panel), Num1:tdEosFP signals were not static but showed bi-directional movements. The proteins traveled from the nucleus towards the sporidia tips and reversed direction to move back towards the nucleus.

Cells were treated with the microtubule-destabilizing drug benomyl [159] to test the influence of the microtubule cytoskeleton on the movement of Num1 in the cytoplasm. Wide field images of benomyl-treated cells revealed that the signal of Num1:tdEosFP in the cytoplasm was significantly reduced after benomyl (40 µM) treatment (Figure 5.17a, lower panel). The kymographs of benomyl-treated sporidia showed markedly reduced transport traces of Num1:tdEosFP in the cytoplasm. Some signals in benomyl treated cell showed horizontal lines, indicating that Num1 molecules were immobilized as a result of the disintegrated microtubule cytoskeleton. Quantitative analysis of 500 continuous frames revealed that 461 ± 47 cytoplasmic fluorescence events of Num1:tdEosFP were detected from the control cells with the photon number threshold of 100. However, the fluorescence events detected from benomyl-treated cells decreased significantly to 171 ± 45 events (Figure 5.17b). The data suggest that integrity of the microtubule cytoskeleton is required for both cytoplasmic localization as well as for cytoplasmic movement of Num1.

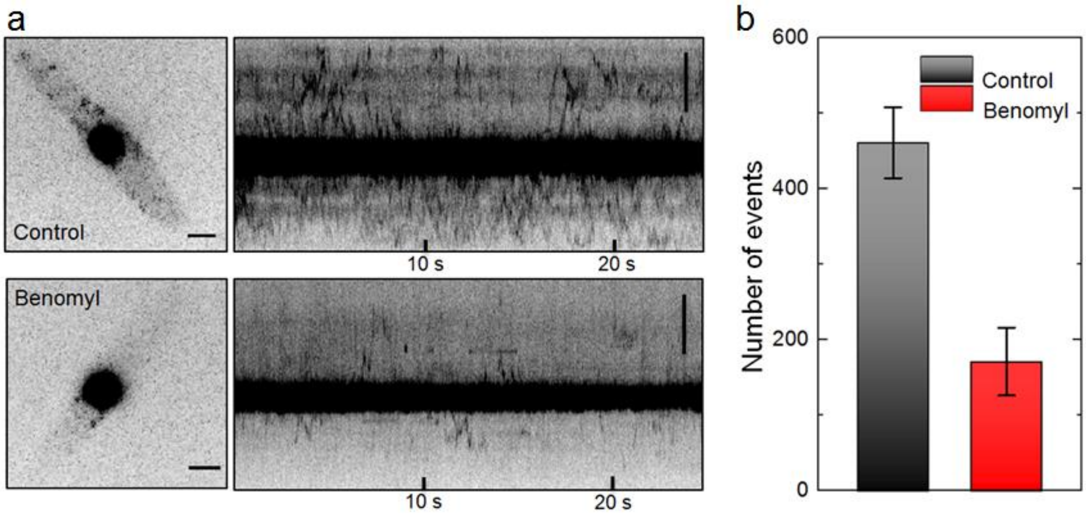

Figure 5.17: Cytoplasmic movement of Num1:tdEosFP depends on intact microtubules. (a) Images and corresponding kymographs of AB31 sporidia expressing Num1:tdEosFP. Images were taken in untreated control (top) and benomyl-treated cells (bottom), respectively. Scale bars, left, 2 µm; right, 5 µm. (b) Numbers of detected fluorescence events of Num1:tdEosFP in the cytoplasm of control and benomyl-treated cells (mean ± SD, n=8).

The requirement of an integer microtubule cytoskeleton suggests that cytoplasmic localization and mobility might depend on microtubule-dependent motor proteins, which would be in line with the previously observed interaction of Num1 with kinesin-1 [48]. Consequently, we assessed the involvement of the two microtubule-associated motor proteins kinesin-1 and kinesin-3 on Num1 transport. My collaborator partner Dr. Theresa Obhof replaced the *kin1* or the *kin3* gene in the AB31 strain by homologous recombination. In the resulting AB31 sporidia and induced hyphae, the movement of num1:tdEosFP was analyzed via kymographs, respectively (Figure 5.18).

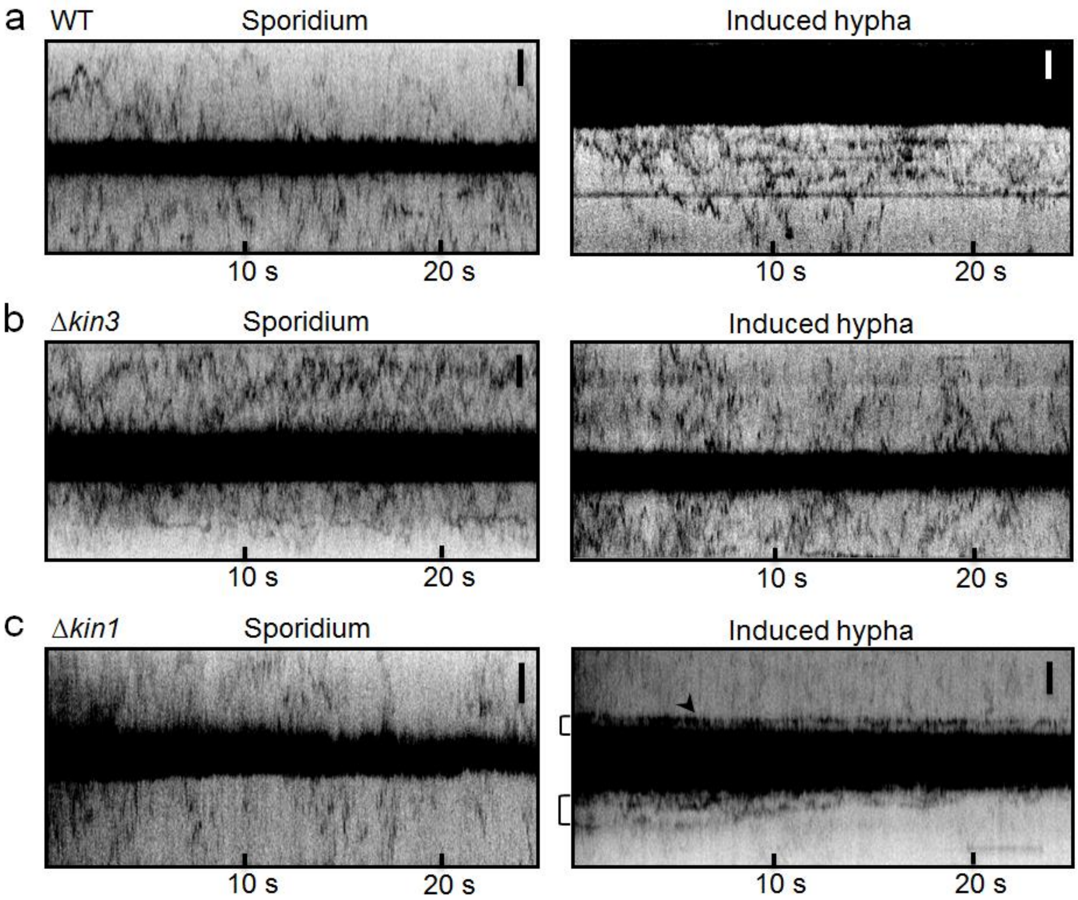

Figure 5.18: Motility of Num1:tdEosFP in AB31 strains depends on kinesin-1 but not kinesin-3. Kymographs of AB31 sporidia and induced hyphae (6 h arabinose induction) expressing Num1:tdEosFP. Images were taken with control cells (a), *kin1* (b) and *kin3* (c) deletion derivatives, respectively. Scale bars, 2 µm.

In control cells, the transport of Num1:tdEosFP in both sporidium, as well as induced hypha, was clearly observed (Figure 5.18a). Similar to wildtype cells, transport of Num1:tdEosFP in the cytoplasm was still visible in *U. maydis* sporidia and induced hyphae upon *kin3* deletion (Figure 5.18b). Cytoplasmic localization and transport of Num1:tdEosFP partially decreased in *kin1*-deleted *U. maydis* sporidia, whereas in the induced hyphae, nearly no traces of transport can be observed in the cytoplasm (Figure 5.18c). This result corresponds with the observation that the morphological phenotype of *kin1*-deleted strains was only visible after induction of filamentous growth. Moreover, after 6 h of induction, localization of Num1:tdEosFP appeared to be restricted to a defined region close to the nucleus (Figure 5.18c). Apparently, the Num1 molecules are “trapped” close to the nucleus and cannot move further into the cytoplasm. These observations suggest that the transport of Num1 depends on kinesin-1 but not kinesin-3.

5.2.3 Discussion

Due to the small amount of cytoplasmically distributed Num1 protein, the detection and study of Num1 were significantly restricted by the labeling efficiency. As the first attempt for super-resolution imaging of Num1, we tested the fusion protein Num1:mEos2. However, the signal was still quite weak for the detection of single molecules with high localization precision. To overcome this problem, we employed tdEosFP, a tandem dimer construct of EosFP. which has previously been used in HEK293 cells [131]. In this work, images and quantitative analyses showed that tdEosFP is superior to monomeric mEos2 concerning both sensitivity and brightness. Compared with the Num1:mEos2 fusion protein, Num1:tdEosFP showed about 4-fold more number of molecule localization events, with a 1.2-fold increased average photon number.

We further investigated the functionality of the fusion protein, Num1:tdEosFP. The replacement of the native *num1* gene with a Num1:tdEosFP fusion construct did not lead to any phenotype accompanied by non-functional Num1 protein, such as altered hyphal morphology or alteration of the motility of early endosomes. These results suggest that the fusion did not affect the function of Num1. Thus, tdEosFP appears to be a feasible tool in *U. maydis* for super-resolution microscopy.

Num1 has been shown to function in the spliceosome-associated NTC-complex, and the predominant localization of Num1 is within the nuclear region. The interaction of Num1 with several cytoplasmic proteins, including the microtubule-dependent motor protein kinesin-1, was observed in previous work [48]. These observations indicated an additional localization of Num1 within the cytoplasm. Faint cytoplasmic signals were detected by using a Num1-GFP fusion protein, however, due to the weak signals, a precisely defined localization was not detectable. In this work, employing the newly established tdEosFP construct the PALM technique, both the cytoplasmic localization and the transport mechanisms of Num1 protein were well studied.

Deletion of the *num1* gene has been shown to affect the transport of early endosomes. However, in this work, no colocalization of Num1:tdEosFP with the early endosome marker, Rab5a, was observed. Moreover, the motility of Num1 was affected by the deletion of *kin1* but not *kin3* gene. Kinesin-3 is the motor protein required for the transport of early endosomes on microtubules [43, 160]. The impact of the *kin3* deletion on motility of Num1 was not observed, which suggested a weak association of Num1 with early endosomes. Therefore, we can exclude that the transport of Num1 depends on kinesin-3 and early endosomes. Indeed, localization of Num1 in *kin1* deletion strains was restricted to a region close to the nucleus, which further proves that transport of Num1 depends on kinesin-1.

As localization and motility of Num1 depend on both the integrity of the cytoskeleton and the motor protein kinesin-1, we assumed a microtubule-associated localization of Num1. By quantitative analyses of two-channel images, we obtained the higher density of Num1:tdEosFP in the area around microtubules than in the entire cytoplasm. This observation also suggests an interaction of Num1 with microtubules. Of note, cytosolic Num1 was not only colocalized with microtubules. The existence of free distributed Num1 proteins could be explained by a weak interaction with microtubule-bound kinesin-1. Indeed, the interaction between the two proteins seems to be rather weak, as the co-purification is only possible after crosslinking [48]. Such a weak interaction would be because of a transient function of Num1 in controlling the dynamics of the kinesin-1 containing complexes on microtubules.

As a conclusion, the fusion protein of Num1 with optimized fluorescent protein tdEosFP has made super-resolution PALM imaging in *U. maydis* feasible. Cytoplasmic localization and the microtubules and kinesin-1 dependent motility have been proven. In general, EosFP in PALM microscopy is a promising tool for studying the cell biology of *U.maydis*.

6. Summary

Live-cell imaging significantly relies on far-field optical microscopic techniques, such as wide-field microscopy and confocal microscopy. Since the discovery of the diffraction barrier in the 19th century, massive efforts have been undertaken to overcome the resolution limit. Over the decades, multiple super-resolution techniques have been developed, among which localization-based super-resolution microscopy opened up a new opportunity to study both the cellular structure and the molecular dynamics at sub-diffraction resolution. In this work, we employed PALM and other conventional microscopic techniques to investigate two biological problems: (1) the membrane repair process in mammalian cells and zebrafish; (2) vesicle dynamics in fungal cells.

6.1 Cell membrane repair process

To study the cell membrane repair process, we first demonstrated a successful method to damage cell membranes by irradiation with a 405 nm laser both on the PALM microscope and the spinning disk confocal microscope. The PALM technique was employed to visualize muscle cells of live zebrafish before and after the membrane damage. By combining the FRC and cross-correlation based drift correction methods to PALM imaging of zebrafish muscle cells, the influence of sample drift during imaging could be significantly reduced. This technique can be further applied for PALM imaging of other live cells, in particular, for imaging of structures such as microtubules and actin cytoskeletons in live cells. For the muscle cell repair process, besides super-resolution imaging, directional motions of functional proteins are also particularly important, especially for investigating the mechanism of protein accumulation. Therefore, we implemented a method of trajectory analysis focusing on directional motion of proteins, which was aimed to observe the protein recruitment process at the single molecule level. With these techniques of PALM imaging and trajectory analysis, we analyzed the roles of proteins, such as MG53 and Dysf, in the membrane repair process both in mammalian cells and zebrafish.

MG53 and Dysf are two essential proteins which facilitate resealing membrane lesion. In this work, we found positively-charged motifs, WKKMFR and WRRFK, which play a significant role in MG53 and Dysf, respectively. For both proteins, their abilities of membrane targeting and rapid accumulation are influenced by the positive charges of the motif. For MG53, a single mutation K279A in the WKKMFR motif led to severe aggregation and vesicular distribution of MG53 in

HeLa cells. Further experiments proved that the mutant accumulated in inclusion bodies due to loss of the positive charge in this crucial position. Similarly, in zebrafish Dysf, loss of the positive charges in the WRRFK motif dramatically impaired membrane targeting and accumulation of Dysf. By using PALM and single molecule tracking techniques, the motion of Dysf along the membrane in damaged zebrafish muscle cell was clearly visualized. Quantitative trajectory analysis further proved that Dysf was recruited from the adjacent membrane to the damaged site. Furthermore, we also investigated the underlying interaction between Dysf and PS via the positively charged motif and concluded that Dysf facilitates transport of PS from the adjacent membrane to the damage site.

In this work, PALM technique was proven to be a powerful tool to study membrane repair process. Especially, the localization-based trajectory analysis focusing on protein directional motion opens a new window for applying localization microscopy. This method could be further applied to the study of other functional proteins and their interactions during membrane repair such as Annexins and Caveolins.

6.2 Vesicle dynamics in fungal cells

The highly polarized growth of filamentous fungi requires continuous transport of construction materials to and from the hyphal tip. To this end, proteins and other biomolecules are packaged in vesicles and transported by motor proteins along the microtubule and actin cytoskeletons. In this work, we studied transport mechanism of the ChsB protein in *A. nidulans* and the Num1 protein in *U. maydis* using the PALM technique, respectively.

By imaging mEosFP*thermo*:ChsB and employing localization-based cluster analysis, we quantitatively analyzed the spatio-temporal development of the Spitzenkörper during cell growth with high resolution. Indeed, vesicle transport in fungal cells is fundamental to sustain the development of the Spitzenkörper and polar growth. We employed high-speed pulse-chase experiments to study transport of ChsB containing vesicles in *A. nidulans*. This technique is a powerful tool for quantitative study of vesicle transport, which allowed us to tag a small subset of molecules at an arbitrary location in the cell and trace their movement with exceptionally low background fluorescence. By combining pulse-chase imaging and kymograph analysis, we determined two different speed ranges of ChsB transport events, below and above ~7 µm s^{-1}, which can be assigned to the transport of ChsB associated with EEs and SVs, respectively. It is the first time that the transport of SVs with a fast speed of ~7 – 10 µm s^{-1} was directly observed in filamentous fungi. From the pulse-chase experiments involving cytoskeleton-destroying drugs, we conclude that ChsB molecules are transported on microtubules to the hyphal tip, where they are further transported on the actin cables to the sites of exocytosis. Further experiments in cell strains with deletion of different motor proteins (kinesin-1, kinesin-3, myosin-5) revealed essential roles of these motor proteins in the polar growth of *A. nidulans*.

We also employed the PALM technique to visualize and study the Num1 protein in *U. maydis* by using the Num1:tdEosFP fusion protein. PALM images showed an apparent dispersed distribution of Num1 over the entire cytoplasm. Two-channel imaging of Num1:tdEosFP and GFP:Tub1 labeled microtubule, and further quantitative analysis of their colocalization suggests that Num1 is partially colocalized with microtubules rather than freely diffusing in the cytoplasm. We further studied the transport mechanism of Num1 by performing kymograph analysis with images acquired on *kin1* or *kin3* deletion cell strains, which showed that the motility of Num1 was regulated by the motor protein kinesin-1 but not kinesin-3. Indeed, we found that localization of Num1 in *kin1* deletion strains was restricted to a region close to the nucleus, which could further prove that transport of Num1 depends on kinesin-1. These results provide evidence that, in addition to its function of pre-mRNA splicing in the nucleus, Num1 also plays a role in the cytosol.

To conclude, we showed the feasibility of super-resolution PALM imaging in fungal cells, e.g., *A. nidulans* and *U. maydis*. Moreover, we demonstrated that the employment of PA-FPs, such as mEosFP*thermo* and tdEosFP in the PALM microscopy is a promising tool for the study of cell biology in hyphae. The investigation of the vesicle dynamics from this work will be beneficial for the development of fungal-based biotechnology applications in research fields such as agriculture, pharmacology, food science and medicine. It will also be promising to further apply the PALM techniques developed in this work to study the vesicle dynamics in mammalian cell lines or tissues in a 2D or 3D space.

Zusammenfassung

Die Bildgebung in lebenden Zellen beruht im Wesentlichen auf optischen fernfeldmikroskopischen Techniken, wie zum Beispiel der Weitfeldmikroskopie und der konfokalen Mikroskopie. Seit der Entdeckung der Auflösungsgrenze im 19. Jahrhundert wurden massive Anstrengungen unternommen, um diese Grenze zu überwinden. Im Laufe der Jahrzehnte wurden mehrere hochauflösende mikroskopische Techniken entwickelt. Die lokalisierungsbasierte hochauflösende Mikroskopie eröffnete eine neue Möglichkeit, sowohl die zelluläre Struktur als auch die molekulare Dynamik unterhalb der Auflösungsgrenze zu untersuchen. In dieser Arbeit wurden PALM und andere konventionelle mikroskopische Techniken verwendet, um zwei biologische Probleme zu untersuchen: (1) den Membranreparaturprozess in Säugerzellen und Zebrafischen; (2) die Vesikeldynamik in Pilzzellen.

Zellmembran-Reparaturprozess

Um den Reparaturprozess der Zellmembran zu untersuchen, zeigten wir zuerst eine erfolgreiche Methode, um Zellmembranen durch Bestrahlung mit Hilfe eines 405 nm Lasers sowohl auf einem PALM-Mikroskop als auch einem Spinning-Disk-Mikroskop zu beschädigen. Die PALM-Technik wurde verwendet, um Muskelzellen von lebenden Zebrafischen vor und nach der Membranschädigung sichtbar zu machen. Durch die Kombination der FRC- und kreuzkorrelationsbasierten Driftkorrekturmethoden mit der PALM-Bildgebung von Zebrafisch-Muskelzellen konnte der Einfluss des Probendrifts während der Bildgebung signifikant reduziert werden. Diese Technik kann weiterhin für die PALM-Bildgebung anderer lebender Zellen angewendet werden, insbesondere für die Bildgebung von Strukturen wie Mikrotubuli und Aktin-Zytoskeletten in lebenden Zellen. Für die Erforschung des Muskelzellenreparaturprozesses ist die Analyse der gerichteten Bewegungen funktioneller Proteine wichtig, um insbesondere den Mechanismus der Proteinakkumulation zu untersuchen. Daher wurde eine Methode der Trajektorien-Analyse implementiert, die sich auf die gerichtete Bewegung von Proteinen konzentriert, um den Proteinrekrutierungsprozess auf Einzelmolekülebene zu beobachten. Mit diesen Techniken der PALM-Bildgebung und der Trajektorien-

Analyse konnte die Rolle von Proteinen wie MG53 und Dysf im Membranreparaturprozess sowohl in Säugetierzellen als auch in Zebrafischen analysiert werden.

MG53 und Dysf sind zwei essenzielle Proteine, die das erneute Versiegeln der Membranläsion erleichtern. In dieser Arbeit fanden wir positiv geladene Motive, WKKMFR und WRRFK, die eine signifikante Rolle in MG53 bzw. Dysf spielen. Bei beiden Proteinen sind ihre Fähigkeit zur Membran-Targeting und schnelle Akkumulation durch die positiven Ladungen des Motivs beeinflusst. Bei MG53 führte eine einzelne Mutation K279A im WKKMFR-Motiv zu einer starken Aggregation und vesikulären Verteilung von MG53 in HeLa-Zellen. Weitere Experimente bestätigten, dass die Mutante in den Einschlusskörpern aufgrund des Verlusts der positiven Ladung in dieser entscheidenden Position akkumuliert wurde. In ähnlicher Weise beeinträchtigte der Verlust der positiven Ladungen in dem WRRFK-Motiv in Zebrafisch Dysf dramatisch das Membran-Targeting und die Akkumulation von Dysf. Durch die Verwendung von PALM- und Einzelmolekül-Tracking-Techniken wurde die Bewegung von Dysf entlang der Membran in beschädigten Zebrafisch-Muskelzellen sichtbar gemacht. Die quantitative Trajektorien-Analyse zeigte weiter, dass Dysf von der angrenzenden Membran zur beschädigten Stelle rekrutiert wurde. Darüber hinaus wurde die zugrundeliegende Wechselwirkung zwischen Dysf und PS über das positiv geladene Motiv untersucht. Es konnte gezeigt werden, dass Dysf den Transport von PS von der benachbarten Membran zur Schadensstelle erleichtert.

In dieser Arbeit erwies sich die PALM-Technik als ein leistungsfähiges Werkzeug zur Untersuchung des Membranreparaturprozesses. Insbesondere die Trajektorien-Analyse, die sich auf die gerichtete Bewegung von Proteinen konzentriert, stellt eine weitere Anwendung der Lokalisationsmikroskopie dar. Diese Methode könnte weitergehend auf die Untersuchung anderer funktioneller Proteine und ihrer Wechselwirkungen während der Membranreparatur wie Annexine und Caveoline angewendet werden.

Vesikeldynamik in Pilzzellen

Das stark polarisierte Wachstum von filamentösen Pilzen erfordert einen kontinuierlichen Transport von Baumaterialien zu und von der Hyphenspitze. Zu diesem Zweck werden Proteine und andere Biomoleküle in Vesikeln verpackt und durch Motorproteine entlang den Mikrotubuli und Aktin-Zytoskeletten transportiert. In dieser Arbeit wurde der Transportmechanismus des ChsB-Proteins in *A. nidulans* und Num1-Proteins in *U. maydis* mit der PALM-Technik untersucht.

Durch Bildgebung von mEosFP*thermo*:ChsB und Verwendung lokalisationsbasierter Clusteranalyse wurde die räumlich-zeitliche Entwicklung des Spitzenkörpers während des Zellwachstums mit hoher Auflösung quantitativ analysiert. Der Vesikeltransport in Pilzzellen ist grundlegend, um die Entwicklung des Spitzenkörpers und des polaren Wachstums zu unterstützen. Es wurden Hochgeschwindigkeits-Pulse-Chase-Experimente verwendet, um den Transport von ChsB-enthaltenden Vesikeln in *A. nidulans* zu untersuchen. Diese Technik ist ein leistungsfähiges Werkzeug für die quantitative Untersuchung des Vesikeltransports. Es kann eine kleine Untergruppe von Molekülen an einer beliebigen Stelle in der Zelle markiert und deren Bewegung mit einer außergewöhnlich niedrigen Hintergrundfluoreszenz verfolgt werden. Durch Kombination der Pulse-Chase-Bildgebung mit der Kymograph-Analyse konnten zwei verschiedene Geschwindigkeitsbereiche von ChsB-Transportereignissen unterhalb und oberhalb von ~ 7 µm s^{-1} bestimmt werden, die dem Transport von ChsB zugewiesen werden können, der mit EEs bzw. SVs assoziiert ist. Erstmalig konnte der Transport von SVs mit einer hohen Geschwindigkeit von ~ 7 - 10 µm s^{-1} direkt in filamentösen Pilzen beobachtet werden. Aus den Pulse-Chase-Experimenten mit den Zytoskelett-zerstörenden Medikamenten schlossen wir, dass ChsB-Moleküle auf Mikrotubuli zur Hyphal-Spitze transportiert werden, wo die Aktin-Kabel sie weiter zu den Stellen der Exozytose transportieren. Weitere Experimente in Zellstämmen mit Deletion verschiedener Motorproteine (Kinesin-1, Kinesin-3, Myosin-5) zeigten die essentielle Rolle dieser Motorproteine im polaren Wachstum von *A. nidulans*.

Die PALM-Technik wurde verwendet, um das Num1-Protein in *U. maydis* unter Verwendung des Num1:tdEosFP-Fusionsproteins zu visualisieren und untersuchen. PALM-Bilder zeigten eine scheinbare dispergierte Verteilung von Num1 über das gesamte Zytoplasma. Zwei-Kanal-Bildgebung von Num1:tdEosFP und GFP:Tub1 markierten Mikrotubuli und weitere quantitative Analysen ihrer Kolokalisation deuten darauf hin, dass Num1 teilweise kolokalisiert mit Mikrotubuli ist, anstatt frei im Zytoplasma zu diffundieren. Wir untersuchten weiter den Transportmechanismus von Num1 durch Kymograph-Analyse mit den Bildern, die von *kin1*- oder *kin3*-Deletionszellstämmen erhalten wurden, die zeigten, dass die Motilität von Num1 durch das Motorprotein Kinesin-1, nicht aber Kinesin-3 reguliert wurde. Tatsächlich fanden wir, dass die Lokalisation von Num1 in kin1-Deletionsstämmen auf eine kernnahe Region beschränkt ist, was weiter belegen könnte, dass der Transport von Num1 vom Kinesin-1-Motorprotein abhängt. Diese Ergebnisse liefern einen Beweis dafür, dass Num1 zusätzlich zu seiner Funktion des prä-mRNA-Spleißens im Zellkern auch eine Rolle im Zytosol spielt.

Abschließend zeigten wir die Durchführbarkeit der hochauflösenden PALM-Bildgebung in Pilzzellen, z.B. *A. nidulans* und *U. maydis*. Darüber hinaus haben wir gezeigt, dass die Verwendung von PA-FPs wie mEosFP*thermo* und tdEosFP in der PALM-Mikroskopie ein vielversprechendes Werkzeug für das Studium der

Zellbiologie in Hyphen ist. Die Untersuchung der Vesikeldynamik aus dieser Arbeit wird für die Entwicklung pilzbasierter biotechnologischer Anwendungen in Forschungsbereichen wie Landwirtschaft, Pharmakologie, Lebensmittelkunde und Medizin von Vorteil sein. Es wird auch vielversprechend sein, die in dieser Arbeit entwickelten PALM-Techniken weiter zu verwenden, um die Vesikeldynamik in Säugerzelllinien oder -geweben in einem 2D- oder 3D-Raum zu untersuchen.

References

[1] W. Bechtel, The cell: locus or object of inquiry? *Stud. Hist. Philos. Sci. Part C Stud. Hist. Philos. Biol. Biomed. Sci.*, **41**, 172–182, (2010).

[2] B. N. G. Giepmans, S. R. Adams, M. H. Ellisman, and R. Y. Tsien, The Fluorescent Toolbox for Assessing Protein Location and Function. *Science*, **312**, 217–224, (2006).

[3] J. R. A. and S. T. R. and M. W. Davidson, Single molecule localization microscopy for superresolution. *J. Opt.*, **15**, 94001, (2013).

[4] F. Yang, L. G. Moss, and G. N. Phillips Jr, The molecular structure of green fluorescent protein. *Nat. Biotechnol*, **14**, 1246–1251, (1996).

[5] C. Schröter, L. Herrgen, A. Cardona, G. J. Brouhard, B. Feldman, and A. C. Oates, Dynamics of zebrafish somitogenesis. *Dev. Dyn.*, **237**, 545–553, (2008).

[6] S. W. Hell, Toward fluorescence nanoscopy. *Nat. Biotechnol*, **21**, 1347–1355, (2003).

[7] M. G. L. Gustafsson, Nonlinear structured-illumination microscopy: Wide-field fluorescence imaging with theoretically unlimited resolution. *Proc. Natl. Acad. Sci. USA*, **102**, 13081–13086, (2005).

[8] E. Betzig *et al.*, Imaging Intracellular Fluorescent Proteins at Nanometer Resolution. *Science*, **313**, 1642–1645, (2006).

[9] M. J. Rust, M. Bates, and X. Zhuang, Stochastic optical reconstruction microscopy (STORM) provides sub-diffraction-limit image resolution. *Nat. Meth.*, **3**, 793–795, (2006).

[10] A. G. Godin, B. Lounis, and L. Cognet, Super-resolution Microscopy Approaches for Live Cell Imaging. *Biophys. J.*, **107**, 1777–1784, (2014).

[11] D. Bansal, K. Miyake, S. Vogel, and S. Groh, Defective membrane repair in dysferlin-deficient muscular dystrophy. *Nature*, **423**, 1–5, (2003).

[12] C. Cai *et al.*, MG53 nucleates assembly of cell membrane repair machinery. *Nat. Cell Biol.*, **11**, 56–64, (2009).

[13] J. Liu *et al.*, Dysferlin, a novel skeletal muscle gene, is mutated in Miyoshi myopathy and limb girdle muscular dystrophy. *Nat. Genet.*, **20**, 31–36, (1998).

[14] R. Bashir *et al.*, A gene related to Caenorhabditis elegans spermatogenesis factor fer-1 is mutated in limb-girdle muscular dystrophy type 2B. *Nat. Genet.*, **20**, 37–42, (1998).

[15] C. Therrien, S. Di Fulvio, S. Pickles, and M. Sinnreich, Characterization of Lipid Binding Specificities of Dysferlin C2 Domains Reveals Novel Interactions with Phosphoinositides. *Biochemistry*, **48**, 2377–2384, (2009).

[16] N. J. Lennon, A. Kho, B. J. Bacskai, S. L. Perlmutter, B. T. Hyman, and R. H. Brown, Dysferlin interacts with annexins A1 and A2 and mediates sarcolemmal wound-healing. *J. Biol. Chem.*, **278**, 50466–50473, (2003).

[17] V. Gerke, C. E. Creutz, and S. E. Moss, Annexins: linking Ca2+ signalling to membrane dynamics. *Nat. Rev. Mol. Cell Biol.*, **6**, 449–461, (2005).

[18] J. Bandorowicz-Pikula, M. Wos, and S. Pikula, Do annexins participate in lipid messenger mediated intracellular signaling? A question revisited. *Mol. Membr. Biol.*, **29**, 229–242, (2012).

[19] U. Roostalu and U. Strähle, In Vivo Imaging of Molecular Interactions at Damaged Sarcolemma. *Dev. Cell*, **22**, 515–529, (2012).

[20] C. Matsuda, Y. K. Hayashi, M. Ogawa *et al.*, The sarcolemmal proteins dysferlin and caveolin-3 interact in skeletal muscle. *Hum. Mol. Genet.*, **10**, 1761-1766, (2001).

[21] D. J. Hernández-Deviez, M. T. Howes, S. H. Laval, K. Bushby, J. F. Hancock, and R. G. Parton, Caveolin Regulates Endocytosis of the Muscle Repair Protein, Dysferlin. *J. Biol. Chem.*, **283**, 6476–6488, (2008).

[22] C. Cai *et al.*, Membrane repair defects in muscular dystrophy are linked to altered interaction between MG53, caveolin-3, and dysferlin. *J. Biol. Chem.*, **284**, 15894–15902, (2009).

[23] G. Redpath *et al.*, Calpain cleavage within dysferlin exon 40a releases a synaptotagmin-like module for membrane repair. *Mol. Biol. Cell*, **25**, 3037–3048, (2014).

[24] A. Lek *et al.*, Calpains, cleaved mini-dysferlinC72, and L-type channels underpin calcium-dependent muscle membrane repair. *J. Neurosci.*, **33**, 5085–5094, (2013).

[25] U. Roostalu and U. Strähle, In vivo imaging of molecular interactions at damaged sarcolemma. *Dev. Cell*, **22**, 515–529, (2012).

[26] C. Cai *et al.*, Zinc Binding to MG53 Protein Facilitates Repair of Injury to Cell Membranes. *J. Biol. Chem.*, **290**, 13830–13839, (2015).

[27] C. Cai *et al.*, MG53 regulates membrane budding and exocytosis in muscle cells. *J. Biol. Chem.*, **284**, 3314–3322, (2009).

[28] J. E. Stajich, F. S. Dietrich, and S. W. Roy, Comparative genomic analysis of fungal genomes reveals intron-rich ancestors. *Genome Biol.*, **8**, R223, (2007).

[29] G. Morel *et al.*, Erratum: Corrigendum: Differential gene retention as an evolutionary mechanism to generate biodiversity and adaptation in yeasts. *Sci. Rep.*, **5**, 12596–12612, (2015).

[30] N. W. Goehring and S. W. Grill, Cell polarity: mechanochemical patterning. *Trends Cell Biol.*, **23**, 72–80, (2013).

[31] P. E. Sudbery, Regulation of polarised growth in fungi. *Fungal Biol. Rev.*, **22**, 44–55, (2008).

[32] A. Bergs, Y. Ishitsuka, M. Evangelinos, G. U. Nienhaus, and N. Takeshita, Dynamics of Actin Cables in Polarized Growth of the Filamentous Fungus *Aspergillus nidulans*. *Front. Microbiol.*, **7**, 682–697, (2016).

[33] M. Schuster, S. Treitschke, S. Kilaru, J. Molloy, N. J. Harmer, and G. Steinberg, Myosin-5, kinesin-1 and myosin-17 cooperate in secretion of fungal chitin synthase. *EMBO J.*, **31**, 214–227, (2012).

[34] G. Steinberg and J. Perez-Martin, *Ustilago maydis*, a new fungal model system for cell biology. *Trends Cell Biol.*, **18**, 61–67, (2008).

[35] M. J. Egan, K. Tan, and S. L. Reck-Peterson, Lis1 is an initiation factor for dynein-driven organelle transport, *J. Cell Biol.*, **197**, 971–982, (2012).

[36] N. Takeshita, R. Manck, N. Grün, S. H. de Vega, and R. Fischer, Interdependence of the actin and the microtubule cytoskeleton during fungal growth. *Curr. Opin. Microbiol.*, **20**, 34–41, (2014).

[37] S. D. Harris, The Spitzenkörper: a signalling hub for the control of fungal development? *Mol. Microbiol.*, **73**, 733–736, (2009).

[38] M. Riquelme and E. Sánchez-León, The Spitzenkörper: a choreographer of fungal growth and morphogenesis, *Curr. Opin. Microbiol.*, **20**, 27–33, (2014).

[39] M. Pinar *et al.*, TRAPPII regulates exocytic Golgi exit by mediating nucleotide exchange on the Ypt31 ortholog RabE(RAB11). *Proc. Natl. Acad. Sci. USA*, **112**, 4346–4351, (2015).

[40] N. Taheri-Talesh, Y. Xiong, and B. R. Oakley, The Functions of Myosin II and Myosin V Homologs in Tip Growth and Septation in *Aspergillus nidulans*. *PLoS One*, **7**, e31218, (2012).

[41] S. Seiler, F. E. Nargang, G. Steinberg, and M. Schliwa, Kinesin is essential for cell morphogenesis and polarized secretion in Neurospora crassa. *EMBO J.*, **16**, 3025–3034, (1997).

[42] N. Requena *et al.*, Genetic evidence for a microtubule-destabilizing effect of conventional kinesin and analysis of its consequences for the control of nuclear distribution in *Aspergillus nidulans*. *Mol. Microbiol.*, **42**, 121–132, (2001).

[43] M. Schuster, S. Kilaru, G. Fink, J. Collemare, Y. Roger, and G. Steinberg, Kinesin-3 and dynein cooperate in long-range retrograde endosome motility along a nonuniform microtubule array. *Mol. Biol. Cell*, **22**, 3645–3657, (2011).

[44] J. H. Lenz, I. Schuchardt, A. Straube, and G. Steinberg, A dynein loading zone for retrograde endosome motility at microtubule plus-ends. *EMBO J.*, **25**, 2275–2286, (2006).

[45] N. Zekert and R. Fischer, The *Aspergillus nidulans* Kinesin-3 UncA Motor Moves Vesicles along a Subpopulation of Microtubules. *Mol. Biol. Cell*, **20**, 673–684, (2009).

[46] J. F. Abenza, A. Galindo, A. Pantazopoulou, C. Gil, V. de los Ríos, and M. A. Peñalva, Aspergillus RabB(Rab5) Integrates Acquisition of Degradative Identity with the Long Distance Movement of Early Endosomes. *Mol. Biol. Cell*, **21**, 2756–2769, (2010).

[47] J. F. Abenza, A. Pantazopoulou, J. M. Rodríguez, A. Galindo, and M. A. Peñalva, Long-distance movement of *Aspergillus nidulans* early endosomes on microtubule tracks. *Traffic*, **10**, 57–75, (2009).

[48] N. Kellner, K. Heimel, T. Obhof, F. Finkernagel, and J. Kämper, The SPF27 Homologue Num1 Connects Splicing and Kinesin 1-Dependent Cytoplasmic Trafficking in *Ustilago maydis*. *PLoS Genet.*, **10**, e1004046, (2014).

[49] L. E. Rogg, J. R. Fortwendel, P. R. Juvvadi, and W. J. Steinbach, Regulation of expression, activity and localization of fungal chitin synthases, *Med. Mycol.*, **50**, 2–17, (2012).

[50] M. D. Lenardon, C. A. Munro, and N. A. R. Gow, Chitin synthesis and fungal pathogenesis. *Curr. Opin. Microbiol.*, **13**, 416–423, (2010).

[51] K. Fukuda, K. Yamada, K. Deoka, S. Yamashita, A. Ohta, and H. Horiuchi, Class III Chitin Synthase ChsB of *Aspergillus nidulans* Localizes at the Sites of Polarized Cell Wall Synthesis and Is Required for Conidial Development. *Eukaryot. Cell*, **8**, 945–956, (2009).

[52] M. D. Lenardon, C. A. Munro, and N. A. R. Gow, Chitin synthesis and fungal pathogenesis. *Curr. Opin. Microbiol.*, **13**, 416–423, (2010).

[53] C. Sacristan, A. Reyes, and C. Roncero, Neck compartmentalization as the molecular basis for the different endocytic behaviour of Chs3 during budding or hyperpolarized growth in yeast cells. *Mol. Microbiol.*, **83**, 1124–1135, (2012).

[54] N. Takeshita *et al.*, Transportation of *Aspergillus nidulans* Class III and V Chitin Synthases to the Hyphal Tips Depends on Conventional Kinesin. *PLoS One*, **10**, e0125937, (2015).

[55] J. Kamper *et al.*, Insights from the genome of the biotrophic fungal plant pathogen *Ustilago maydis*. *Nature*, **444**, 97–101, (2006).

[56] T. Brefort, G. Doehlemann, A. Mendoza-Mendoza, S. Reissmann, A. Djamei, and R. Kahmann, *Ustilago maydis* as a Pathogen. *Annu. Rev. Phytopathol.*, **47**, 423–445, (2009).

[57] M. Schuster, R. Lipowsky, M. A. Assmann, P. Lenz, and G. Steinberg, Transient binding of dynein controls bidirectional long-range motility of early endosomes. *Proc. Natl. Acad. Sci. USA*, **108**, 3618–3623, (2011).

[58] S. Baumann, T. Pohlmann, M. Jungbluth, A. Brachmann, and M. Feldbrügge, Kinesin-3 and dynein mediate microtubule-dependent co-transport of mRNPs and endosomes. *J. Cell Sci.*, **125**, 2740–2752, (2012).

[59] M. Grote *et al.*, Molecular Architecture of the Human Prp19/CDC5L Complex. *Mol. Cell. Biol.*, **30**, 2105–2119, (2010).

[60] K. Nasmyth and P. Nurse, Cell division cycle mutants altered in DNA replication and mitosis in the fission yeast Schizosaccharomyces pombe. *Mol. Gen. Genet. (MGG)*, **182**, 119–124, (1981).

[61] R. Ohi *et al.*, The Schizosaccharomyces pombe cdc5+ gene encodes an essential protein with homology to c-Myb. *EMBO J.*, **13**, 471–483, (1994).

[62] H. S. Bernstein and S. R. Coughlin, A Mammalian Homolog of Fission Yeast Cdc5 Regulates G2 Progression and Mitotic Entry. *J. Biol. Chem.*, **273**, 4666–4671, (1998).

[63] M. Brendel *et al.*, Role of PSO genes in repair of DNA damage of Saccharomyces cerevisiae. *Mutat. Res. Rev. Mutat. Res.*, **544**, 179–193, (2003).

[64] N. Zhang, R. Kaur, X. Lu, X. Shen, L. Li, and R. J. Legerski, The Pso4 mRNA Splicing and DNA Repair Complex Interacts with WRN for Processing of DNA Interstrand Cross-links. *J. Biol. Chem.*, **280**, 40559–40567, (2005).

[65] B. D. Beck, S. J. Park, Y. J. Lee, Y. Roman, R. A. Hromas, and S. H. Lee, Human Pso4 Is a Metnase (SETMAR)-binding Partner That Regulates Metnase Function in DNA Repair, *J. Biol. Chem.*, **283**, 9023–9030, (2008).

[66] X. Lu and R. J. Legerski, The Prp19/Pso4 Core complex Undergoes Ubiquitylation and Structural Alterations in Response to DNA Damage. *Biochem. Biophys. Res. Commun.*, **354**, 968–974, (2007).

[67] R. J. Legerski, The Pso4 complex splices into the DNA damage response. *Cell Cycle*, **8**, 3448–3449, (2009).

[68] J. Wiedenmann *et al.*, EosFP, a fluorescent marker protein with UV-inducible green-to-red fluorescence conversion. *Proc. Natl. Acad. Sci. USA*, **101**, 15905–15910, (2004).

[69] K. Nienhaus, G. U. Nienhaus, J. Wiedenmann, and H. Nar, Structural basis for photo-induced protein cleavage and green-to-red conversion of fluorescent protein EosFP. *Proc. Natl. Acad. Sci. USA*, **102**, 9156–9159, (2005).

[70] S. T. Hess, T. P. K. Girirajan, and M. D. Mason, Ultra-High Resolution Imaging by Fluorescence Photoactivation Localization Microscopy. *Biophys. J.*, **91**, 4258–4272, (2006).

[71] E. Abbe, Beiträge zur Theorie des Mikroskops und der mikroskopischen Wahrnehmung. *Arch. für mikroskopische Anat.*, **9**, 413–468, (1873).

[72] L. RAYLEIGH, On the Theory of Optical Images, with Special Reference to the Microscope. *J. R. Microsc. Soc.*, **23**, 447–473, (1903).

[73] P. N. Hedde and G. U. Nienhaus, Optical imaging of nanoscale cellular structures. *Biophys. Rev.*, **2**, 147–158, (2010).

[74] R. E. Thompson, D. R. Larson, and W. W. Webb, Precise nanometer localization analysis for individual fluorescent probes. *Biophys. J.*, **82**, 2775–2783, (2002).

[75] R. Wombacher *et al.*, Live-cell super-resolution imaging with trimethoprim conjugates. *Nat. Meth.*, **7**, 717–719, (2010).

[76] H. Deschout *et al.*, Precisely and accurately localizing single emitters in fluorescence microscopy. *Nat. Meth.*, **11**, 253–266, (2014).

[77] S. W. Hell, *Far-field optical nanoscopy*. *Science*, **316**, 1153–1158, (2007).

[78] H. Shroff, C. G. Galbraith, J. A. Galbraith, and E. Betzig, Live-cell photoactivated localization microscopy of nanoscale adhesion dynamics. *Nat. Meth.*, **5**, 417–423, (2008).

[79] S. H. Shim *et al.*, Super-resolution fluorescence imaging of organelles in live cells with photoswitchable membrane probes. *Proc. Natl. Acad. Sci. USA*, **109**, 13978–13983, (2012).

[80] R. Henriques, C. Zimmer, T. A. Laurence, and B. A. Chromy, QuickPALM : 3D real-time photoactivation nanoscopy image processing in ImageJ. *Nat. Meth.*, 339–340, (2010).

[81] P. N. Hedde, J. Fuchs, F. Oswald, J. Wiedenmann, and G. U. Nienhaus, Online image analysis software for photoactivation localization microscopy. *Nat Meth.*, **6**, 689–690, (2009).

[82] F. Huang *et al.*, Video-rate nanoscopy using sCMOS camera-specific single-molecule localization algorithms. *Nat. Meth.*, **10**, 653–658, (2013).

[83] O. Shimomura, F. H. Johnson, and Y. Saiga, Extraction, Purification and Properties of Aequorin, a Bioluminescent Protein from the Luminous Hydromedusan, *Aequorea*. *J. Cell. Comp. Physiol.*, **59**, 223–239, (1962).

[84] D. C. Prasher, V. K. Eckenrode, W. W. Ward, F. G. Prendergast, and M. J. Cormier, Primary structure of the Aequorea victoria green-fluorescent protein. *Gene*, **111**, 229–233, (1992).

[85] M. Chalfie, Y. Tu, G. Euskirchen, W. W. Ward, and D. C. Prasher, Green fluorescent protein as a marker for gene expression. *Science*, **263**, 802-805, (1994).

[86] P. N. Hedde and G. U. Nienhaus, Super-resolution localization microscopy with photoactivatable fluorescent marker proteins. *Protoplasma*, **251**, 349–362, (2014).

[87] K. A. Lukyanov, D. M. Chudakov, S. Lukyanov, and V. V. Verkhusha, Photoactivatable fluorescent proteins. *Nat. Rev. Mol. Cell Biol.*, **6**, 885–890, (2005).

[88] J. Lippincott-Schwartz and G. H. Patterson, Fluorescent Proteins for Photoactivation Experiments. *Meth. Cell Biol.*, **85**, 45–61, (2008).

[89] J. Lippincott-Schwartz and G. H. Patterson, Photoactivatable fluorescent proteins for diffraction-limited and super-resolution imaging. *Trends Cell Biol.*, **19**, 555–565, (2009).

[90] G. H. Patterson and J. Lippincott-Schwartz, A Photoactivatable GFP for Selective Photolabeling of Proteins and Cells. *Science*, **297**, 1873–1877, (2002).

[91] F. V Subach, G. H. Patterson, S. Manley, J. M. Gillette, J. Lippincott-Schwartz, and V. V. Verkhusha, Photoactivatable mCherry for high-resolution two-color fluorescence microscopy. *Nat. Meth.*, **6**, 153–159, (2009).

[92] M. Andresen *et al.*, Photoswitchable fluorescent proteins enable monochromatic multilabel imaging and dual color fluorescence nanoscopy. *Nat. Biotech.*, **26**, 1035–1040, (2008).

[93] R. Ando, H. Mizuno, and A. Miyawaki, Regulated fast nucleocytoplasmic shuttling observed by reversible protein highlighting. *Science*, **306**, 1370–1373, (2004).

[94] J. Fuchs *et al.*, A photoactivatable marker protein for pulse-chase imaging with superresolution. *Nat. Meth.*, **7**, 627–630, (2010).

[95] J. Wiedenmann *et al.*, From EosFP to mIrisFP: structure-based development of advanced photoactivatable marker proteins of the GFP-family. *J. Biophotonics*, **4**, 377–90, (2011).

[96] K. Nienhaus and G. Ulrich Nienhaus, Fluorescent proteins for live-cell imaging with super-resolution. *Chem. Soc. Rev.*, **43**, 1088–1106, (2014).

[97] G. T. Dempsey, J. C. Vaughan, K. H. Chen, M. Bates, and X. Zhuang, Evaluation of fluorophores for optimal performance in localization-based super-resolution imaging. *Nat. Meth.*, **8**, 1027–1036, (2011).

[98] R. Henriques, C. Griffiths, E. H. Rego, and M. M. Mhlanga, PALM and STORM: Unlocking live-cell super-resolution. *Biopolymers*, **95**, 5, p. 322–331, (2011).

[99] A. Sharonov and R. M. Hochstrasser, Wide-field subdiffraction imaging by accumulated binding of diffusing probes. *Proc. Natl. Acad. Sci. USA*, **103**, 18911–18916, (2006).

[100] R. Jungmann, M. S. Avendaño, J. B. Woehrstein, M. Dai, W. M. Shih, and P. Yin, Multiplexed 3D cellular super-resolution imaging with DNA-PAINT and Exchange-PAINT. *Nat. Meth.*, **11**, 313–318, (2014).

[101] S. A. Jones, S.-H. Shim, J. He, and X. Zhuang, Fast three-dimensional super-resolution imaging of live cells. *Nat. Meth.*, **8**, 499–508, (2011).

[102] H. D. Lee *et al.*, Superresolution Imaging of Targeted Proteins in Fixed and Living Cells Using Photoactivatable Organic Fluorophores. *J. Am. Chem. Soc.*, **132**, 15099–15101, (2010).

[103] K. W. Teng *et al.*, Labeling Proteins Inside Living Cells Using External Fluorophores for Fluorescence Microscopy. *Elife*, **6**, e25460, (2017).

[104] S. B. Andersson, Localization of a fluorescent source without numerical fitting. *Opt. Express*, **16**, 18714–18724, (2008).

[105] H. Ma, F. Long, S. Zeng, and Z. L. Huang, Fast and precise algorithm based on maximum radial symmetry for single molecule localization, *Opt. Lett.*, **37**, 2481–2483, (2012).

[106] R. Parthasarathy, Rapid, accurate particle tracking by calculation of radial symmetry centers. *Nat. Meth.*, **9**, 724–726, (2012).

[107] T. Quan *et al.*, Ultra-fast, high-precision image analysis for localization-based super resolution microscopy. *Opt. Express*, **18**, 11867–11876, (2010).

[108] C. S. Smith, N. Joseph, B. Rieger, and K. A. Lidke, Fast, single-molecule localization that achieves theoretically minimum uncertainty. *Nat. Meth.*, **7**, 373–375, (2010).

[109] R. J. Ober, S. Ram, and E. S. Ward, Localization Accuracy in Single-Molecule Microscopy. *Biophys. J.*, **86**, 1185–1200, (2004).

[110] Y. Li, Y. Ishitsuka, P. N. Hedde, and G. U. Nienhaus, Fast and Efficient Molecule Detection in Localization-Based Super-Resolution Microscopy by Parallel Adaptive Histogram Equalization. *ACS Nano*, **7**, 5207–5214, (2013).

[111] D. Sage *et al.*, Quantitative evaluation of software packages for single-molecule localization microscopy. *Nat. Meth.*, **12**, 717–724, (2015).

[112] a Kusumi, Y. Sako, and M. Yamamoto, Confined lateral diffusion of membrane receptors as studied by single particle tracking (nanovid microscopy). Effects of calcium-induced differentiation in cultured epithelial cells. *Biophys. J.*, **65**, 2021–2040, (1993).

[113] A. D. Douglass and R. D. Vale, Single-molecule microscopy reveals plasma membrane microdomains created by protein-protein networks that exclude or trap signaling molecules in T cells. *Cell*, **121**, 937–950, (2005).

[114] S. Manley *et al.*, High-density mapping of single-molecule trajectories with photoactivated localization microscopy. *Nat. Meth.*, **5**, 155–157, (2008).

[115] T. J. Feder, I. Brust-Mascher, J. P. Slattery, B. Baird, and W. W. Webb, Constrained diffusion or immobile fraction on cell surfaces: a new interpretation. *Biophys. J.*, **70**, 2767–2773, (1996).

[116] M. J. Saxton and K. Jacobson, SINGLE-PARTICLE TRACKING: Applications to Membrane Dynamics. *Annu. Rev. Biophys. Biomol. Struct.*, **26**, 373–399, (1997).

[117] D. H. Kim *et al.*, Analysis of Interactions between the Epidermal Growth Factor Receptor and Soluble Ligands on the Basis of Single-Molecule Diffusivity in the Membrane of Living Cells. *Angew. Chem. Int. Ed.*, **54**, 7028–7032, (2015).

[118] X. Chen, J. Zaro, and W. C. Shen, Fusion Protein Linkers: Property, Design and Functionality. *Adv. Drug Deliv. Rev.*, **65**, 1357–1369, (2013).

[119] C. Etard, O. Armant, U. Roostalu, V. Gourain, M. Ferg, and U. Strähle, Loss of function of myosin chaperones triggers Hsf1-mediated transcriptional response in skeletal muscle cells. *Genome Biol.*, **16**, 267-287, (2015).

[120] T. Yeung, G. E. Gilbert, J. Shi, J. Silvius, A. Kapus, and S. Grinstein, Membrane Phosphatidylserine Regulates Surface Charge and Protein Localization. *Science*, **319**, 210–213, (2008).

[121] A. Lam *et al.*, Improving FRET dynamic range with bright green and red fluorescent proteins. *Nat. Meth.*, **9**, 1005–1012, (2012).

[122] J. F. Hancock, A. I. Magee, J. E. Childs, and C. J. Marshall, All ras proteins are polyisoprenylated but only some are palmitoylated. *Cell*, **57**, 1167–1177, (1989).

[123] V. Middel *et al.*, Dysferlin-mediated phosphatidylserine sorting engages macrophages in sarcolemma repair. *Nat. Commun.*, **7**, 12875, (2016).

[124] T. Nayak *et al.*, A Versatile and Efficient Gene-Targeting System for *Aspergillus nidulans*. *Genetics*, **172**, 1557–1566, (2006).

[125] R. Manck, Y. Ishitsuka, S. Herrero, N. Takeshita, G. U. Nienhaus, and R. Fischer, Genetic evidence for a microtubule-capture mechanism during polarised growth of *Aspergillus nidulans*. *J. Cell Sci.*, **128**, 3569–3582, (2015).

[126] L. Zhou *et al.*, Superresolution and pulse-chase imaging reveal the role of vesicle transport in polar growth of fungal cells. *Sci. Adv.*, **4**, e1701798, (2018).

[127] A. Brachmann, G. Weinzierl, J. Kämper, and R. Kahmann, Identification of genes in the bW/bE regulatory cascade in *Ustilago maydis*. *Mol. Microbiol.*, **42**, 1047–1063, (2001).

[128] R. Holliday, *Ustilago maydis*. In: King RC ed. Handbook of Genetics. *USA Plenum Press*, New York, 579–595, (1974).

[129] J. Sambrook and D. Russell, Molecular Cloning: A Laboratory Manual. *Cold Spring Harbor Laboratory Press*, Australia, (2001).

[130] K. Zarnack *et al.*, Tetracycline-regulated gene expression in the pathogen *Ustilago maydis*. *Fungal Genet. Biol.*, **43**, 727–738, (2006).

[131] G. U. Nienhaus *et al.*, Photoconvertible Fluorescent Protein EosFP: Biophysical Properties and Cell Biology Applications. *Photochem. Photobiol.*, **82**, 351–358, (2006).

[132] K. König, Cell damage during multi-photon microscopy. *Handb. Biol. Confocal Microsc., Spinger Science+Business Media*, New York, 680–689, (2006).

[133] A. Hopt and E. Neher, Highly nonlinear photodamage in two-photon fluorescence microscopy. *Biophys. J.*, **80**, 2029–2036, (2001).

[134] M. R. Banyard and R. L. Tellam, The free cytoplasmic calcium concentration of tumorigenic and non-tumorigenic human somatic cell hybrids. *Br. J. Cancer*, **51**, 761–766, (1985).

[135] M. Guizar-Sicairos, S. T. Thurman, and J. R. Fienup, Efficient subpixel image registration algorithms. *Opt. Lett.*, **33**, 156–158, (2008).

[136] R. P. J. Nieuwenhuizen *et al.*, Measuring image resolution in optical nanoscopy. *Nat. Meth.*, **10**, 557–562, (2013).

[137] Y. Ishitsuka *et al.*, Superresolution microscopy reveals a dynamic picture of cell polarity maintenance during directional growth. *Sci. Adv.*, **1**, e1500947, (2015).

[138] S. H. Lee, J. Y. Shin, A. Lee, and C. Bustamante, Counting single photoactivatable fluorescent molecules by photoactivated localization microscopy (PALM). *Proc. Natl. Acad. Sci. USA*, **109**, 17436–17441, (2012).

[139] S. T. Cooper and P. L. McNeil, Membrane Repair: Mechanisms and Pathophysiology. *Physiol. Rev.*, **95**, 1205–1240, (2015).

[140] D. Bansal *et al.*, Defective membrane repair in dysferlin-deficient muscular dystrophy. *Nature*, **423**, 6936, 168–172, (2003).

[141] D. A. Griffin *et al.*, Defective membrane fusion and repair in Anoctamin5-deficient muscular dystrophy. *Hum. Mol. Genet.*, **25**, 1900–1911, (2016).

[142] Y. Nakai, Y. Nomura, T. Sato, A. Shiratsuchi, and Y. Nakanishi, Isolation of a Drosophila Gene Coding for a Protein Containing a Novel Phosphatidylserine-Binding Motif. *J. Biochem.*, **137**, 593–599, (2005).

[143] K. R. Rosenbloom *et al.*, ENCODE Data in the UCSC Genome Browser: year 5 update. *Nucleic Acids Res.*, **41**, 56–63, (2013).

[144] A. Vonderheit and A. Helenius, Rab7 Associates with Early Endosomes to Mediate Sorting and Transport of Semliki Forest Virus to Late Endosomes. *PLoS Biol.*, **3**, e233, (2005).

[145] S. Bergink *et al.*, DNA damage triggers nucleotide excision repair-dependent monoubiquitylation of histone H2A. *Genes Dev.*, **20**, 1343–1352, (2006).

[146] R. R. Kopito, Aggresomes, inclusion bodies and protein aggregation. *Trends Cell Biol.*, **10**, 524–530, (2000).

[147] Z. Wen, Z. Zhong, and J. E. Darnell, Maximal Activation of Transcription by Statl and Stat3 Requires Both Tyrosine and Serine Phosphorylation. *Cell*, **82**, 241–250, (1995).

[148] D. Wüstner, L. M. Solanko, F. W. Lund, D. Sage, H. J. Schroll, and M. A. Lomholt, Quantitative fluorescence loss in photobleaching for analysis of protein transport and aggregation. *BMC Bioinformatics*, **13**, 296–317, (2012).

[149] D. B. Davis, K. R. Doherty, A. J. Delmonte, and E. M. Mcnally, Calcium-sensitive Phospholipid Binding Properties of Normal and Mutant Ferlin C2 Domains. *J. Biol. Chem.*, **277**, 22883–22888, (2002).

[150] L. Araujo-Bazán, M. A. Peñalva, and E. A. Espeso, Preferential localization of the endocytic internalization machinery to hyphal tips underlies polarization of the actin cytoskeleton in *Aspergillus nidulans*. *Mol. Microbiol.*, **67**, 891–905, (2008).

[151] N. Takeshita, Y. Higashituji, S. Konzack, and R. Fischer, Apical Sterol-rich Membranes Are Essential for Localizing Cell End Markers That Determine Growth Directionality in the Filamentous Fungus *Aspergillus nidulans*. *Mol. Biol. Cell*, **19**, 339–351, (2008).

[152] T. Horio, The Role of Microtubules in Rapid Hyphal Tip Growth of *Aspergillus nidulans*. *Mol. Biol. Cell*, **16**, 918–926, (2004).

[153] A. Pantazopoulou, M. Pinar, X. Xiang, and M. A. Peñalva, Maturation of late Golgi cisternae into RabE(RAB11) exocytic post-Golgi carriers visualized in vivo. *Mol. Biol. Cell*, **25**, 2428–2443, (2014).

[154] N. Takeshita *et al.*, Pulses of Ca2+ coordinate actin assembly and exocytosis for stepwise cell extension. *Proc. Natl. Acad. Sci. USA*, **114**, 5701–5706, (2017).

[155] A. Berepiki, A. Lichius, and N. D. Read, Actin organization and dynamics in filamentous fungi. *Nat. Rev. Micro.*, **9**, 876–887, (2011).

[156] R. Gibeaux, D. Hoepfner, I. Schlatter, C. Antony, and P. Philippsen, Organization of Organelles within Hyphae of Ashbya gossypii Revealed by Electron Tomography. *Eukaryot. Cell*, **12**, 1423–1432, (2013).

[157] G. Steinberg, R. Wedlich-Soldner, M. Brill, and I. Schulz, Microtubules in the fungal pathogen *Ustilago maydis* are highly dynamic and determine cell polarity. *J. Cell Sci.*, **114**, 609–622, (2001).

[158] A. Straube, I. Weber, and G. Steinberg, A novel mechanism of nuclear envelope break-down in a fungus: nuclear migration strips off the envelope. *EMBO J.*, **24**, 1674–1685, (2005).

[159] G. Fink and G. Steinberg, Dynein-dependent Motility of Microtubules and Nucleation Sites Supports Polarization of the Tubulin Array in the Fungus *Ustilago maydis*. *Mol. Biol. Cell*, **17**, 3242–3253, (2006).

[160] R. Wedlich-Söldner, A. Straube, M. W. Friedrich, and G. Steinberg, A balance of KIF1A-like kinesin and dynein organizes early endosomes in the fungus *Ustilago maydis*. *EMBO J.*, **21**, 2946–2957, (2002).

List of Abbreviations

AA	Amino acid
A.nidulans	*Aspergilus nidulans*
CM	Condition medium
CPU	Central processing unit
DMEM	Dulbecco's Modified Eagle's medium
Dysf	Dysferlin
EE	Early endosome
EMCCD	Electron multiplying charge-coupled device
FBS	Fetal bovine serum
FLIP	Fluorescence loss in photobleaching
FRAP	Fluorescence recovery after photobleaching
FRC	Fourier Ring Correlation
FWHM	Full width at half maximum
GFP	Green fluorescent protein
GPU	Graphics processing unit
KD	Knockdown
MESAB	Ethyl-m-aminobenzoate metanesulphonate
MLE	Maximum likelihood estimator
MO	Morpholino
MSD	Mean squared displacement
NA	Numerical aperture
PA-FP	Photoactivatable fluorescent protein
PALM	Photoactivated localization microscopy
PS	Phosphatidylserine
PSF	Point spread function
qRT-PCR	Quantitative real-time polymerase chain reaction

ROS	Reactive oxygen species
SD	Standard deviation
sptPALM	Single-particle tracking PALM
SSIM	Saturated structured illumination microscopy
STED	Stimulated emission depletion microscopy
STORM	Stochastic optical reconstruction microscopy
SV	Secretory vesicle
tdEosFP	Tandem dimeric EosFP
TIRF	Total internal reflection fluorescence
U. maydis	*Ustilago maydis*

List of Publications

- Middel, V., **Zhou, L.**, Takamiya, M., Beil, T., Shahid, M. Roostalu, U., Grabher, C., Rastegar, S., Reischl, M., Nienhaus, G. U., & Strähle, U. **Dysferlin-Mediated Phosphatidylserine Sorting Engages Macrophages in Sacrolemma Repair**. *Nature Commun.* **7** (2016) 12875.

- Gao, P., Prunsche, B., **Zhou, L.**, Nienhaus, K., & Nienhaus, G. U. **Background Suppression in Fluorescence Nanoscopy with Stimulated Emission Double Depletion**. *Nature Photon*. **11** (2017) 163-169.

- Takeshita, N., Evangelinos, M., **Zhou, L.**, Somera-Fajardo, R. A., Lu, L., Takaya, N., Nienhaus, G. U., & Fischer, R. **Pulses of Ca^{2+} Influx Coordinate Actin Depolymerization, Vesicle Fusion and Stepwise Cell Extension in Filamentous Fungi.** *Proc. Natl. Acad. Sci. USA* **114** (2017) 5701-5706.

- Müller, P., Zieger, M. M., Richter, B., Quick, A. S., Fischer, J., Mueller, J. B., **Zhou, L.**, Nienhaus, G. U., Bastmeyer, M., Barner-Kowollik, C., & Wegener, M. **A Novel Molecular Switch for Sub-Diffraction Laser Lithography by Photoenol Intermediate-State Cis-Trans Isomerization.** *ACS Nano* **11** (2017) 6396-6403.

- **Zhou, L.**, Evangelinos, M., Wernet, V., Eckert, A. F., Ishitsuka, Y., Fischer, R., Nienhaus, G. U., & Takeshita, N. **Superresolution and Pulse-chase Imaging Reveal the Role of Vesicle Transport in Polar Growth of Fungal Cells.** *Sci. Adv.* **4** (2018) e1701798.

- **Zhou, L.**, Obhof, T., Schneider, K., Feldbrügge, M., Nienhaus, G. U., & Kämper, J. **Cytoplasmic Transport Machinery of SPF27 Homologue Num1 in *Ustilago maydis*.** Submitted.

- **Zhou, L.**, Middel, V., Strähle, U., & Nienhaus, G. U. **Distinct Motives Rich in Positive Charges Regulate Membrane Targeting of Dysferlin and MG53.** In preparation.

Acknowledgment

First of all, I would like to express my sincere gratitude to **Prof. Dr. Gerd Ulrich Nienhaus** for giving me the opportunity to work in his group and guiding in all the time my research. He drew my interest in localization microscopy and encouraged me to explore many different research fields with super-resolution techniques. I appreciate his trust, motivation, and help on the writing of this thesis. I also want to thank **Prof. Dr. Uli Lemmer** for his support on my preparation for the defense and review this work as the first referee.

I would like to thank all the members of my group for their kind help and support during these four years. I'm very thankful to **Dr. Karin Nienhaus** for her constructive suggestions, stimulating discussions and careful revision of my thesis. A special thanks go to our technician **Julia Kuhlmann** for her input and support on the biological field of this work. I am also deeply indebted to other group members: **Dr. Yiming Li**, **Dr. Yuji Ishitsuka**, **Dr. Peng Gao**, **Linxiao Yang** and all the others. I enjoyed so much to the pleasant and intellectual atmosphere of our group. It is my great experience to work with experts with different backgrounds.

I would also like to thank my collaboration partners, **Dr. Norio Takeshita**, **Dr. Volker Middel** and **Dr. Theresa Obhof**. I had very nice time to work with them, and I appreciate their contributions to providing biological samples and constructive scientific discussions.

A special thanks go to the Wunderlich family for their continuous support. I am very grateful for their kindness and endless help to me.

Finally, particular thanks go to my parents for their support and inspiration, in spite of being so far away from me. None of this would have been possible without them. Thank you so much.